AFRL-AFOSR-VA-TR-2019-0033

Phase II: Design and Assessment of Multifunctional Coatings for Ablation and Emissivity Performance

RODNEY TRICE
PURDUE UNIVERSITY

02/01/2019
Final Report

Air Force Research Laboratory
AF Office Of Scientific Research (AFOSR)/ RTB1
Arlington, Virginia 22203
Air Force Materiel Command

REPORT DOCUMENTATION PAGE

Form Approved
OMB No. 0704-0188

1. REPORT DATE *(DD-MM-YYYY)*	2. REPORT TYPE	3. DATES COVERED *(From - To)*
1/26/2019	Final	10/1/15-9/30/2018

4. TITLE AND SUBTITLE
PHASE II: DESIGN AND ASSESSMENT OF MULTIFUNCTIONAL COATINGS FOR ABLATION AND EMISSIVITY PERFORMANCE

5a. CONTRACT NUMBER
FA9550-16-1-0039

5b. GRANT NUMBER

5c. PROGRAM ELEMENT NUMBER

6. AUTHOR(S)
R.W. Trice

5d. PROJECT NUMBER

5e. TASK NUMBER

5f. WORK UNIT NUMBER

7. PERFORMING ORGANIZATION NAME(S) AND ADDRESS(ES)
Purdue University
701 W. Stadium
West Lafayette, IN 47907

8. PERFORMING ORGANIZATION REPORT NUMBER

9. SPONSORING/MONITORING AGENCY NAME(S) AND ADDRESS(ES)
AFOSR
801 N. Randolph Street Suite 732
Arlington, VA 22203

10. SPONSOR/MONITOR'S ACRONYM(S)
Dr. Ali Sayir

11. SPONSOR/MONITOR'S REPORT NUMBER(S)

12. DISTRIBUTION/AVAILABILITY STATEMENT
No Limitations on Distribution

13. SUPPLEMENTARY NOTES
none

14. ABSTRACT
In Phase II, reported on here, we investigated multifunctional coatings for re-entry applications that combine high emissivity with ablation resistance. The microstructural evolution of ablated samarium-doped zirconium diboride/silicon carbide was investigated to understand the formation of the c1-Sm0.2Zr0.8O1.9 (SZO) oxide layer and its constituent components. In collaboration with AFRL we also measured the emittance of different emissivity modifiers.

15. SUBJECT TERMS
Hypersonic, emittance, ablation, ceramics

16. SECURITY CLASSIFICATION OF:			17. LIMITATION OF ABSTRACT	18. NUMBER OF PAGES	19a. NAME OF RESPONSIBLE PERSON
a. REPORT	b. ABSTRACT	c. THIS PAGE			Rodney W. Trice
Unc	Unc	Unc	UU	73	19b. TELEPHONE NUMBER *(Include area code)* 765 494 6405

INSTRUCTIONS FOR COMPLETING SF 298

1. REPORT DATE. Full publication date, including day, month, if available. Must cite at least the year and be Year 2000 compliant, e.g. 30-06-1998; xx-06-1998; xx-xx-1998.

2. REPORT TYPE. State the type of report, such as final, technical, interim, memorandum, master's thesis, progress, quarterly, research, special, group study, etc.

3. DATE COVERED. Indicate the time during which the work was performed and the report was written, e.g., Jun 1997 - Jun 1998; 1-10 Jun 1996; May - Nov 1998; Nov 1998.

4. TITLE. Enter title and subtitle with volume number and part number, if applicable. On classified documents, enter the title classification in parentheses.

5a. CONTRACT NUMBER. Enter all contract numbers as they appear in the report, e.g. F33315-86-C-5169.

5b. GRANT NUMBER. Enter all grant numbers as they appear in the report. e.g. AFOSR-82-1234.

5c. PROGRAM ELEMENT NUMBER. Enter all program element numbers as they appear in the report, e.g. 61101A.

5e. TASK NUMBER. Enter all task numbers as they appear in the report, e.g. 05; RF0330201; T4112.

5f. WORK UNIT NUMBER. Enter all work unit numbers as they appear in the report, e.g. 001; AFAPL30480105.

6. AUTHOR(S). Enter name(s) of person(s) responsible for writing the report, performing the research, or credited with the content of the report. The form of entry is the last name, first name, middle initial, and additional qualifiers separated by commas, e.g. Smith, Richard, J, Jr.

7. PERFORMING ORGANIZATION NAME(S) AND ADDRESS(ES). Self-explanatory.

8. PERFORMING ORGANIZATION REPORT NUMBER. Enter all unique alphanumeric report numbers assigned by the performing organization, e.g. BRL-1234; AFWL-TR-85-4017-Vol-21-PT-2.

9. SPONSORING/MONITORING AGENCY NAME(S) AND ADDRESS(ES). Enter the name and address of the organization(s) financially responsible for and monitoring the work.

10. SPONSOR/MONITOR'S ACRONYM(S). Enter, if available, e.g. BRL, ARDEC, NADC.

11. SPONSOR/MONITOR'S REPORT NUMBER(S). Enter report number as assigned by the sponsoring/ monitoring agency, if available, e.g. BRL-TR-829; -215.

12. DISTRIBUTION/AVAILABILITY STATEMENT. Use agency-mandated availability statements to indicate the public availability or distribution limitations of the report. If additional limitations/ restrictions or special markings are indicated, follow agency authorization procedures, e.g. RD/FRD, PROPIN, ITAR, etc. Include copyright information.

13. SUPPLEMENTARY NOTES. Enter information not included elsewhere such as: prepared in cooperation with; translation of; report supersedes; old edition number, etc.

14. ABSTRACT. A brief (approximately 200 words) factual summary of the most significant information.

15. SUBJECT TERMS. Key words or phrases identifying major concepts in the report.

16. SECURITY CLASSIFICATION. Enter security classification in accordance with security classification regulations, e.g. U, C, S, etc. If this form contains classified information, stamp classification level on the top and bottom of this page.

17. LIMITATION OF ABSTRACT. This block must be completed to assign a distribution limitation to the abstract. Enter UU (Unclassified Unlimited) or SAR (Same as Report). An entry in this block is necessary if the abstract is to be limited.

Subject: Final Report

Grant Title: PHASE II: DESIGN AND ASSESSMENT OF MULTIFUNCTIONAL COATINGS FOR ABLATION AND EMISSIVITY PERFORMANCE

Grant #: FA9550-16-1-0039
Reporting Period: October 1, 2015 – September 30, 2018

Prepared By: Prof. Rodney Trice, Purdue University

Abstract

Hypersonic vehicles require sharp featured leading edges to reduce drag on the vehicle. One approach to reducing the temperature in these components, often as high as 2000°C, is to increase the emissivity of the surface, affording more re-radiation of the incoming heat. Phase I of this work developed a Sm^{3+}-doped SiC/ZrB_2 coating system that not only demonstrated an emissivity of 0.9 at 1600°C, but also increased ablation resistance compared to an undoped SiC/ZrB_2 coating. In Phase II, reported on here, we investigated multifunctional coatings for re-entry applications that combine high emissivity with ablation resistance. The microstructural evolution of ablated samarium-doped zirconium diboride/silicon carbide was investigated to understand the formation of the c_1-$Sm_{0.2}Zr_{0.8}O_{1.9}$ (SZO) oxide layer and its constituent components. It was found that SZO phase is formed in two steps, beginning with oxidation of the Sm-dopant and ZrB_2 into Sm_2O_3 and ZrO_2, respectively. The formation of a borosilicate glass on the surface of the ablated sample quickly removed the effect of any surface features or density on emittance. In collaboration with AFRL/Dr. Jonathan Vernon, we are also pursued the development of samples with selective emittance by blending together two different emissivity modifiers (Sm and Er) in a ZrB_2/SiC matrix. ZBS billets co-doped with Sm and Er forms a potential tailorable emittance c_1-$(Sm/Er)_{0.2}Zr_{0.8}O_{1.9}$ oxide scale as the major phase during oxidation. Emittance values were mixed due to differences in oxidation of the surface.

Accomplishment 1: Cyclic Ablation of High-Emissivity Sm-Doped ZrB_2/SiC Coatings on Alumina Substrates

I. Introduction

Future hypersonic vehicle design involves the use of sharp leading edges instead of blunt ones to improve performance and reduce aerodynamic drag [1]. Increased convective heating of these edges can result in thermal shock and ablation by atmospheric friction during the reentry process [1]. Among the ultra-high temperature ceramics (UHTCs) being considered for leading edges, studies have shown that ZrB_2-SiC (ZBS) is one of the best materials for this application due to its high melting point and strength at 1500°C and above, as well as its ablation and thermal shock resistance [2,3,4].

Studies performed by Tan et al. [3,6] have shown that adding Sm dopant to ZBS ceramics increases the emissivity compared to ceramics comprised of only ZBS. Specifically, a total hemispherical emittance of 0.9 at 1600°C was measured for a coating comprised of 5 mol.% Sm with a balance of ZrB_2/SiC. Furthermore, the Sm dopant improved ablation performance by forming a stable oxide scale of c1-Sm0.2Zr0.9O1.9, which has a melting point between 2500°C and 2700°C, and thus can withstand temperature extremes expected during hypersonic flight [5].

In the previous report by Tan et al. [5], a single ablation cycle of 60 s was performed on the ZBS coatings (with variable Sm concentration) applied to dense ZrB2/SiC substrates. The temperature achieved was up to 2039°C and the Sm oxide scale remain adhered to the unreacted coating. The original design of the current study was to investigate the effect of thermal cycling (e.g. repeated ablation cycles) on ZrB_2/SiC coatings with different levels of Sm dopant. Cyclic ablation is not well understood, and it was deemed important to consider the cyclic life of these coatings when used as leading edge materials to predict of ablation resistance in dynamic environments [7]. However, the Sm-doped ZrB_2/SiC coatings were applied to alumina substrates rather than ZrB_2/SiC substrates with distinct differences in coating performance observed. Thus, in this study, ZBS coatings doped with 0, 3, 5 and 8 mol.% Sm (ZBS, 3SmZBS, 5SmZBS and 8SmZBS, respectively) were evaluated via cyclic ablation testing on alumina substrates. The specimens were heated rapidly up to temperatures exceeding 1600°C for 60 s using an oxyacetylene torch for two cycles. The microstructure and phase assemblage after each cycle were analyzed and discussed.

II. Experimental Procedure

(1) Materials and powder preparation

Spray-dried powders were prepared from a suspension that consisted of 80 vol.% ZrB_2 (3–5 μm, Grade A, HC Starck, Munich, Germany), 20 vol.% α-SiC (1.4 m, Grade UF-05, HC Starck, Munich, Germany), 0.4 wt.% dispersant (Darvan 821A, R.T. Vanderbilt Company, Inc., Norwalk, USA), 2 wt.% PVA binder (Celvol 203, Celanese Corporation, Dallas, USA) and DI water. The average spray-dried particle size was approximately 38 μm. Samarium dopant was added to the spray dried ZrB_2/SiC powders via a chemical infiltration method. In this process, 5, 10, and 15

mol.% samarium nitrate hexahydrate (99.9% pure $Sm(NO_3)_3 \cdot 6H_2O$, Sigma-Aldrich, St. Louis, USA) were dissolved into 200-proof ethanol and the resulting solution was then infiltrated into the porous spray-dried ZrB_2/SiC powder. Next, the solvent was removed via a rotary evaporator (BM 200, Yamato Scientific America Inc., Santa Clara, USA) at 100°C. This powder was heated at 400°C in air for an hour to remove residual moisture and nitrates. Tan et al.[3] showed that below 400 °C both the ZBS and the Sm-doped coatings did not have any weight gain. As the normalize weight gain resulted to be approximate zero below 400°C, it suggests that the oxygen content does not have any effect during the heat treatment at 400°C. The first weight gain inflections start near 600°C due to the oxidation of ZrB2 to form m-ZrO_2 and B_2O_3 glass [3].

Subsequently, the dried mixture was sieved using a 60-mesh (250 μm aperture) to eliminate large agglomerates. Fumed silica (0.02 wt.%, Cab-O-Sil®, Cabot Corporation, Boston, USA) was added to all the powders as a flowing agent for feeding the powders during the plasma spray process.

Table 1. Plasma spray deposition parameters [3].

Current (A)	200
Deposition Efficiency (%)	~50-60
Standoff (cm)	2.54
Powder Flow (g/min)	10
Tranverse Speed (cm/s)	117
Process Gas	Argon, Hydrogen

The coatings were prepared at Praxair Surface Technologies (Indianapolis, USA) using a shrouded plasma spray process on alumina substrates. Table 1 shows the plasma spray deposition parameters. Powders were plasma sprayed onto 7 mm thick alumina substrates with an average coating thickness of roughly 200-350 μm. Samples were cut to 25.4 mm x 25.4 mm. The amount of $Sm(NO_3)_3$ (mol%) incorporated into the coatings was measured by mass spectroscopy on pulverized coatings (NSL Analytical Services Inc., Cleveland, USA). The actual concentrations of $Sm(NO_3)_3$ (mol%) in each coating are listed in Table 2, along with the bulk density and total porosity, measured from earlier reports [5,6]. XRD results on as-sprayed coatings showed that ZrB2 is the major phase and the biggest peak of α-SiC at 35.5° (2θ). As showed on Tan results [5], a similar broad hump SmO and Sm_2O_3 peaks was identified on the broad hump between 26-35° (2θ). To help simplify discussion, the naming convention is based on the actual Sm molar concentration. For instance, the 3SmZBS coating contains ~3 mol.% Sm in the ZrB2/SiC matrix.

Table 2. As sprayed coating composition and properties, reproduced from [6].

	$Sm(NO_3)_3$ (mol.%)	Actual Sm (mol.%)	Bulk Density (g/cm^3)	Total Porosity (%)
ZBS	0	0	4.5	18.2
3SmZBS	5	2.8	4.1	26.1
5SmZBS	10	5.3	3.7	32.0
8SmZBS	15	8.2	3.5	35.7

(2) Oxyacetylene Ablation Testing

Heat flux conditions and ablation resistance were assessed using an oxyacetylene ablative torch rig. The test rig was constructed using ASTM 285-082 as a standard [6]. The ablation torch (Victor Technologies, St. Louis, USA) used a 5 mm orifice and the separation distance of 20 mm between the sample and the torch tip was held as a constant. Front and back face temperatures were measured using a two-color pyrometer (OS3750, Omega Engineering Inc., Stamford, CT, USA) which was connected to a data logger. This was used to measure temperature as a function of time. The emissivity setting for the pyrometer was estimated to be 0.9. An oxygen rich environment was simulated using an oxygen:acetylene ratio of 12:10 slpm. Test specimens were exposed to 60 s intervals of flame. Samples were cooled to room temperature and characterized before another cycle was performed. Mass change that occurred was not reported due to some of the coatings delaminating. The heat flux was measured to be 452 W/cm^2 using a thermogage circular foil heat flux gauge (TG1000-4, Vatell Corp., Christiansburg, VA).

(3) Microstructural and Phase Analysis

Before performing the microstructural analysis, the samples were coated with a thin layer of Au/Pd. A scanning electron microscope (SEM) (Phillips XL-40, FEI Co., Hillsboro, USA) was used to characterize coating topography in the as sprayed conditions after each cycle. X-ray diffraction (XRD) (D8 Focus, Bruker Corporation, Billerica, USA) was used to analyze the phases present. Cu Kα radiation was used over 2θ values of 20°-80° on the coatings after ablation using a step size of 0.02° and a scan rate of 5°/minute. Samples were aligned in the XRD to analyze the regions where the ablation flame was most intense.

III. Results

(1) Ablation Results after Cycle 1

Figure 1a shows a plot of front face temperature as a function of time during the 1st ablation cycle for each of the four coatings tested. The ZBS coating displayed a continuous temperature increase through the 60 s of heating, with a maximum of 1502°C measured. Each of the Sm-doped coatings displayed a temperature discontinuity upon heating. This discontinuity occurred at 1570°C, 1545°C, and 1577°C for the 3SmZBS, 5SmZBS, and 8SmZBS coatings respectively. Each of the Sm-doped coatings displayed a higher front face temperature than the ZBS coating after the discontinuity.

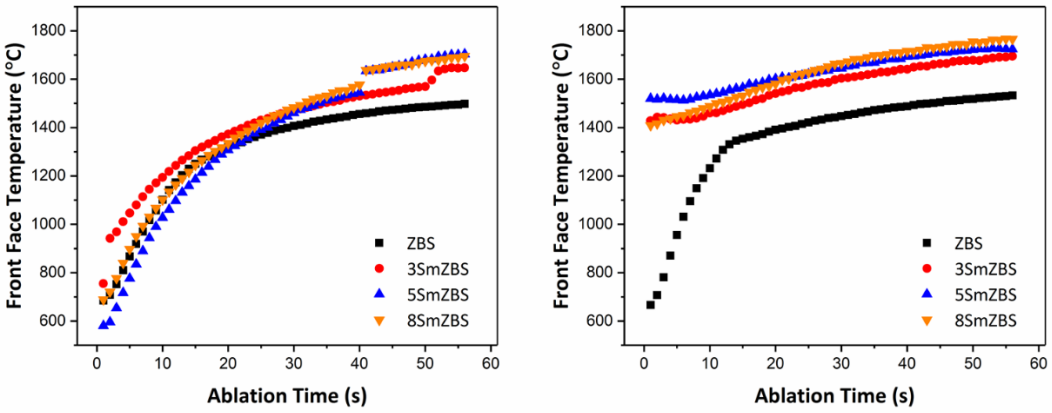

Fig. 1. Front face temperature during the 60-second ablation for the (a) 1st cycle and (b) 2nd cycle.

Figure 2 shows the surface of the coatings after the 1st ablation cycle. The ZBS coating (Figure 2a) displayed little macroscopic evidence of the thermal cycle. Each of the Sm-doped ZBS coatings in Figures 2b, 2c and 2d developed a delamination blister after the 1st cycle. Due to the limited conduction through the thickness of the coating and substrate, the blister is responsible for the increase in front face temperature and the temperature curve discontinuities observed in Figure 1a.

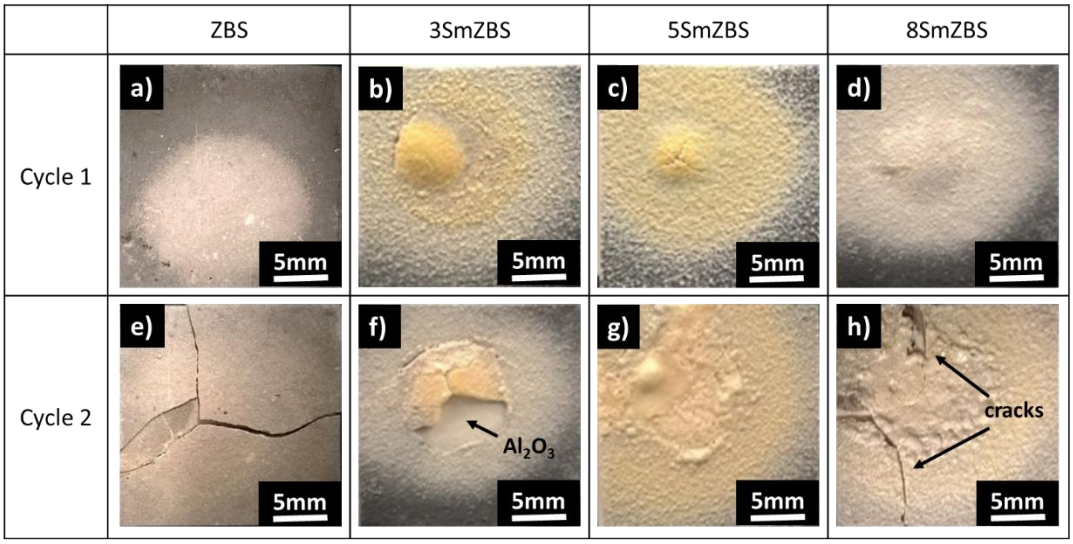

Fig. 2. Optical images of the ablated coatings: a) ZBS, b) 3SmZBS, c) 5SmZBS and d) 8SmZBS after cycle 1, and e) ZBS, f) 3SmZBS, g) 5SmZBS, and h) 8SmZBS after cycle 2. The Al_2O_3 substrate became visible in 3SmZBS after the 2nd ablation cycle due to coating delamination.

The SEM micrograph of the ZBS coating after the 1st ablation cycle (Figure 3a) shows the formation of an oxide scale with a few pores. For the Sm-doped coatings, the surface appears to have clusters of "islands" which are crystalline regions. Figure 3b shows very fine islands in the 3SmZBS surface, while the islands in 5SmZBS in Figure 3c appear to be larger and are surrounded by "lagoons". Based on the micrographs in Figure 3b to 3d, the islands appear to increase in size

as more Sm dopant in present in the ZBS coating. Additionally, the 8SmZBS coating (Figure 3d) has large bubbles that have popped during the ablation cycle and a crack forming.

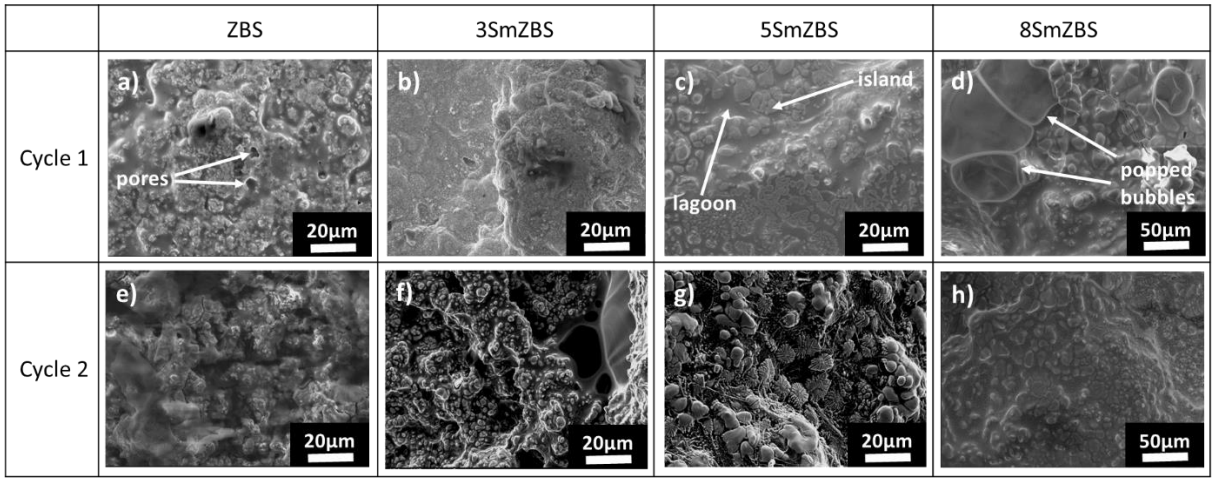

Fig. 3. Scanning electron micrographs of the following coatings: a) ZBS, b) 3SmZBS, c) 5SmZBS and d) 8SmZBS after cycle 1, and e) ZBS, f) 3SmZBS, g) 5SmZBS, and h) 8SmZBS after cycle 2. Burst bubbles are observed in the top right of the 8SmZBS microstructure after the 1st cycle and flower-like microstructures are observed in the 5SmZBS coating after the 2nd cycle.

The XRD plot for the ZBS coating in Figure 4a match with the previous studies [3,5], where the primary phase formed was monoclinic zirconia (m-ZrO_2, JCPDS-37-1484) with very small amounts of tetragonal zirconia (t-ZrO_2, JCPDS-80-0965) observed. For the 3SmZBS, the primary phase formed is m-ZrO_2, with a Sm-stabilized t-ZrO_2 phase formed. Based on the relative intensities, the ratio of Sm-stabilized t-ZrO_2 phase to m-ZrO_2 increases as the Sm concentration increases. Only the t-ZrO_2 phase was detected for the 8SmZBS coating.

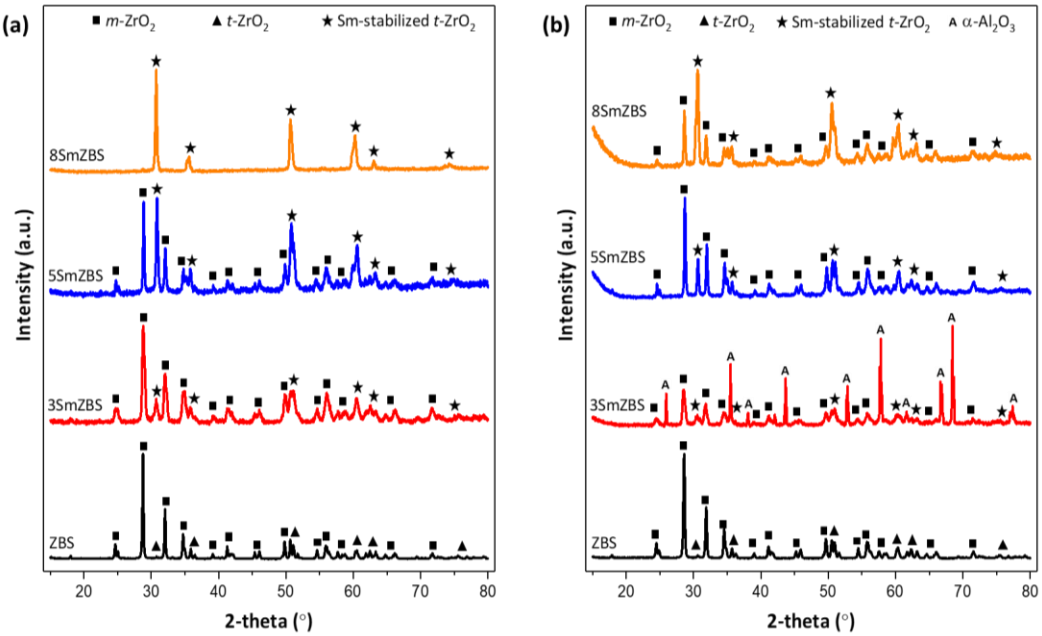

Fig. 4. X-ray diffraction patterns of the surface after the (a) 1st cycle and (b) 2nd cycle.

(2) Ablation Results after Cycle 2

Figure 1b shows the front face temperature during the 2nd 60-second ablation cycle. The maximum temperature reached by the ZBS during this cycle reached 1540°C, compared to 1502°C during the 1st cycle. For the three Sm-doped coatings, the temperature curves were continuous, but significantly hotter (~200°C) than the ZBS specimen. The increased front face temperature of the doped coatings is due to the limited conduction of heat away from front face, a consequence of the blister formed during cycle 1.

Since no temperature discontinuities were observed in Figure 1b, there is no further blistering occurring during the 2nd ablation cycle for all the coatings. Note that the ZBS coating failed due to cracking of the underlying alumina substrate and showed little evidence of damage prior to this from ablation testing. The 3SmZBS coating (Figure 2f) spalled off during cooling and revealed the alumina substrate below the coating. Both the 5SmZBS and 8SmZBS samples displayed a glassy layer on the surface after the 2nd ablation cycle in Figures 2g and 2h. There were cracks formed on the 8SmZBS (Figure 2h) sample upon cooling due to thermal shock.

Figure 3e presents the surface topography of the ZBS coating after the 2nd ablation cycle; gaps have formed in the oxide scale. The islands observed in the first cycle have overall increased in sizes for the Sm-doped coatings. A similar trend as the 1st cycle is observed here, where the crystalline regions increase in size with more Sm dopant. The 5SmZBS sample surface, shown in Figure 3g, now contains flower-like structures amongst the islands. Furthermore, the bubbles observed after cycle 1 in the 8SmZBS coating have disappeared and the microstructure now only contains the crystalline islands among the amorphous lagoon area.

Figure 5a presents the SEM cross-sectional microstructure of the ZBS coating after the 2nd ablation cycle. The Sm doped coatings separated from the substrate, except on a larger scale in the ablation zone. The evidence of the crystalline islands and the amorphous lagoon structures are also evident as seen in figure 5d.

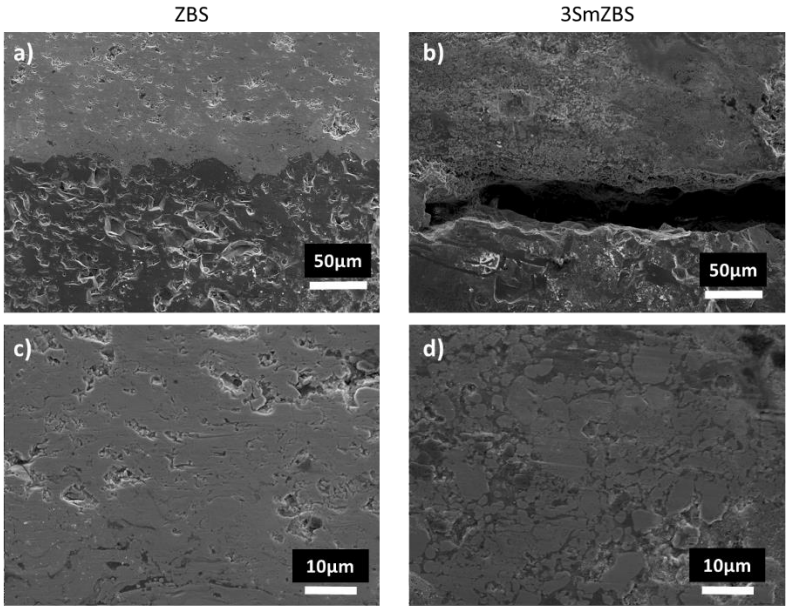

Fig 5. SEM- EDS cross section of a) ZBS at 350x, b) 3SmZBS at 350x, c) ZBS at 2000x above the blister, and d) 3SmZBS at 2000x above the blister. Islands ZrO_2 and amorphous boria/silica lagoons can be seen in the 3SmZBS.

Figure 4b shows the XRD results obtained from the surface of the coatings after the 2nd ablation cycle. The XRD of ZBS remains unchanged, being mainly comprised of m-ZrO_2 with small amounts of t-ZrO_2 observed. The 3SmZBS sample had peaks associated with □-Al_2O_2, consistent with the spallation of the coating from the substrate as evidenced in Figure 2f. The 5SmZBS coating was comprised of m-ZrO_2 and Sm-stabilized t-ZrO_2 phase. The 8SmZBS coating was still primarily the Sm-stabilized t-ZrO_2 phase, but peaks associated with m-ZrO_2 were observed. Both the 5SmZBS and 8SmZBS show evidence of an amorphous phase at lower 2θ.

IV. Discussion

(1) First observation: *Samarium-doped coatings blister during ablation testing*

The first observation was the blister formed in the Sm-doped ZBS coatings during ablation testing. Blister formation was not observed in the ZBS coating after either cycle 1 or 2. The Al_2O_3/ZrO_2 phase diagram [9], presented in Figure 6, shows that pure ZrO_2 melts at 2710°C. As Al_2O_3 mixes with the ZrO_2, there is an important eutectic reaction which occurs at 1860oC and acts as a melting point reduction. The complete invariant reaction occurring at 1860°C is given as:

$$L\ (58wt.\%\ Al_2O_3) \qquad Al_2O_3 + t\text{-}ZrO_2\ (4wt.\%\ Al_2O_3)$$

Thus, even small amounts of alumina (> 4 wt.%) can result in a small volume percent of liquid phase. However, Figure 1 indicates that the temperature of the coatings never reached 1860°C during testing, and therefore, cannot be responsible for the blisters formed. The cross section depicted figure 5c shows that no glassy phase was seen on the SEM cross section for the ZBS coating. This suggests that no liquid phase at the interface was formed during ablation.

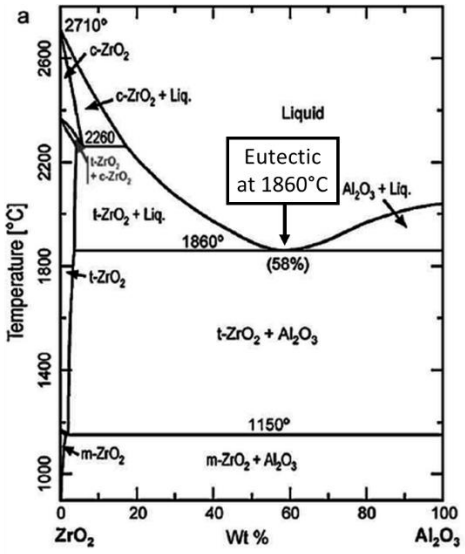

Fig. 6. ZrO_2-Al_2O_3 phase diagram, adapted from reference [9].

A simplified ternary phase diagram showing the effect of Sm2O3 on phase assemblage when the proportions of Al_2O_3 and ZrO_2 are kept constant is presented in Figure 7. The phase diagram shows a melting point depression at 1680°C for an alloy with 15 mol.% of Sm_2O_3/42.5 mol.% Al_2O_3/42.5 mol.% ZrO2 that correspond to the ternary eutectic composed by Al_2O_3 (AL), F-ZrO_2 (F), and the perovskite structure $SmAlO_3$ (SA) [10]. The SEM-EDS cross section results for the 3SmZBS coatings shows the presence of a glassy phase (figure 5d. The presence of this amorphous phase confirms that the alumina compositions for all the samarium-doped coatings at the interface between the substrate and the coating were higher than the 42.5 mol.% of alumina needed to start forming a liquid phase at the ternary eutectic point (as shown in figure 7).

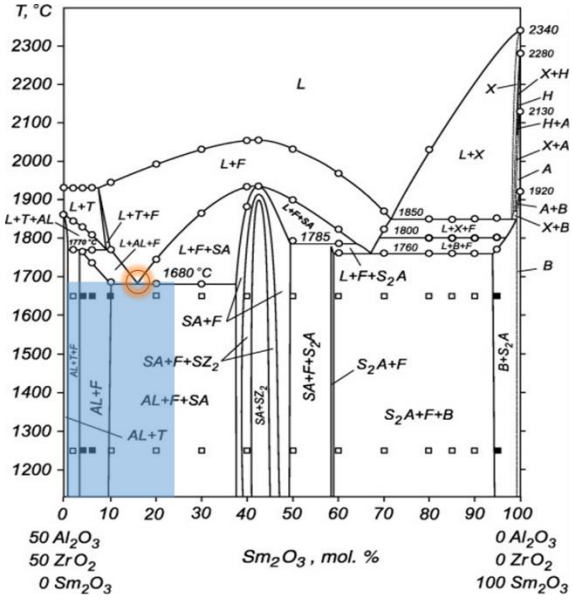

Fig. 7. Al_2O_3-ZrO_2-Sm_2O_3 phase diagram, adapted from reference [10].

The SEM-EDS for all the samarium-doped ZBS coatings suggest that at the ablated region, which experienced temperatures above 1680°C, formed a liquid phase composed of Si, Sm, and Al along with F-ZrO_2 above this temperature. Eventually, after the sample is cooled to room temperature, a glassy phase (composed of Si, Sm and Al) along with zirconia is formed as shown in the SEM cross section in figure 5d. This glassy phase provides evidence that with the addition of Sm to the ZBS coating, along with the abundant supply of oxygen from the atmosphere during ablation, leads to the formation of a liquid phase as it reacts with the alumina substrate and oxidized ZrB2 coating. This local melting would cause thermal stresses to induce a separation of the coating from the substrate, and thus result in a blister.

Based on the phase diagram, it is expected to see the discontinuity on the ablation temperature at 1680°C for 3SmZBS instead of the 1570°C showed in figure 1a as well as for 5SmZBS and 8SmZBS. The oxides formed are also different from the findings by Tan et. al. [5]. The temperature difference may be explained by the assumption that the coating emissivity was 0.9 (as set on the pyrometer). As the emissivity of an oxidized surface are generally lower, it would underestimate the temperature measured, in this case by ~110°C.

However, all the samarium-doped ZBS samples had parts where the coating was not detached from the substrate. Figure 8 presents cross-section of the 2nd cycle of 3SmZBS coating in a cooler ablation zone. There are clearly three distinct regions. Region 1 had 18wt% Al which is not enough to form the liquid and remained adhered to the substrate. Figures 10 and 11 shows that the same behavior occurred for the 5SmZBS, and 8SmZBS coatings at the cooler ablation zones. It provides further evidence that in order to develop a blister, the samples need to satisfy two conditions: a critical amount of alumina becoming part of the coating and being heated above the ternary eutectic temperature. Satisfying these two conditions will make the coating to form the glassy phase and detach from the alumina substrate.

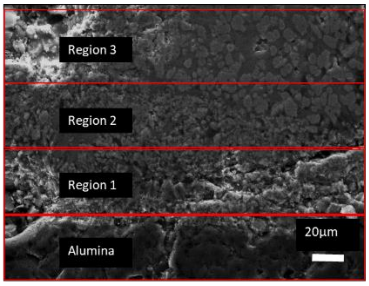

	Al(wt%)	Zr(wt%)	O(wt%)	Si(wt%)	Sm(wt%)	C(wt%)
Region 1	18	28	16	16	12	11
Region 2	11	40	15	12	12	10
Region 3	12	47	4	12	21	3

Fig 8. SEM- EDS cross section of cycle 2 of 3SmZBS with EDS analysis at region 1, 2, and 3 for several elements.

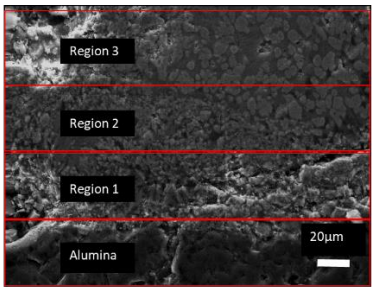

	Al(wt%)	Zr(wt%)	O(wt%)	Si(wt%)	Sm(wt%)	C(wt%)
Region 1	18	28	16	16	12	11
Region 2	11	40	15	12	12	10
Region 3	12	47	4	12	21	3

Fig 9. SEM- EDS cross section of cycle 2 of 5SmZBS with EDS analysis at region 1, 2, and 3 for several elements.

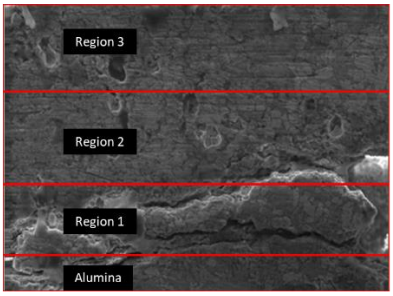

	Al(wt%)	Zr(wt%)	O(wt%)	Si(wt%)	Sm(wt%)	C(wt%)
Region 1	13.55	37.29	15.18	6.03	7.06	20.90
Region 2	9.19	48.98	11.94	6.76	5.47	17.67
Region 3	8.77	45.31	16.24	6.80	5.03	17.86

Fig 10. SEM- EDS cross section of cycle 2 of 8SmZBS with EDS analysis at region 1, 2, and 3 for several elements.

(2) Second observation: *Difference in microstructure as Sm dopant is increased*

The ZBS coating demonstrated some porosity after the 1st cycle due to the evaporation of gaseous by-products, such as B_2O_3, CO and CO_2. SiC is commonly added to ZrB2 in order to reduce the high evaporation rate of B_2O_3 by forming a silica-rich scale [11]. However, the distribution of SiC throughout the composite is discontinuous [12] and further depletion of volatile products create an uneven surface topography after the 2nd cycle as observed in Figure 3e.

Sm is commonly used as a silica glass modifier in optical applications [13]. The addition of Sm dopant to ZBS coatings have demonstrated a reduction in viscosity of the primarily silica-based glassy phase in previous reports [3,6] and this is particularly evident for the 8SmZBS coating after cycle 1 in this study. Since the glass formed in the 8SmZBS coating had the lowest viscosity amongst the Sm-doped coatings, the evolution of volatile products can lead relatively easy bubble formation shown in Figure 3d [14]. Bubbles are typically observed in ZBS systems between 1450°C and 1650°C, and they collapse and disappear within a minute during the cooling process [15]. As the glassy products are evaporated during the 1st cycle of ablation test, the overall viscosity will increase. Consequently, there were no popped bubbles observed after the 2nd ablation cycle of the 8SmZBS coating.

A flower-like microstructure was observed in Figure 3g for the 5SmZBS coating after the 2nd cycle. Figure 11 shows a higher magnification micrograph of the flower-like structures found at a different location. These structures were noted by Karlsdottir et al. [16] for ZBS coatings during oxidation at 1550°C for up to 4 hours. The study described the "islands" (center regions of the flower-like structure) to be m-ZrO_2, the "petals" to be B_2O_3 glass, and the "lagoon" regions to be SiO_2 glass. The formation of the flower-like structure is driven by the viscous fingering phenomena, which is the displacement of a less viscous liquid [17]. It is known that during the oxidation of ZBS coatings, ZrB_2 reacts to form an inner layer composed of crystalline ZrO_2 and liquid B_2O_3, and the SiC reacts to form a SiO_2 outer film [11,18,19]. Due to the instability of the moving interface, the less viscous B_2O_3 liquid displaces a more viscous SiO_2 liquid [19]. The rising B_2O_3 rich liquid contains dissolved ZrO_2, which deposits in the center of the flower-like structure when the B_2O_3 evaporates. The liquid boria-rich oxidation product is transported through the overlying layer of SiO_2 liquid by convection, forming convection cells aligned like the petals of a flower [16].

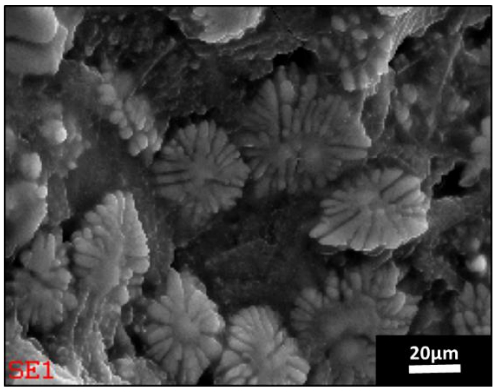

Fig. 11. SEM micrograph of the flower-like microstructure on the 5SmZBS coating after the 2nd cycle.

The flower-like structure formed on the 5SmZBS sample was not seen in the 3SmZBS and 8SmZBS coatings. Since the addition of Sm affects the viscosity of the glassy phase, this has resulted in several differences in the microstructures as a function of the amount of Sm dopant added. This is evident by the sizes of islands and lagoons in the micrographs. The low evaporation rate for 3SmZBS led to formation of very fine ZrO_2 islands shown after the 1st cycle (Figure 3b). After the 2nd cycle, the islands have increased in size, similar to the island size in 5SmZBS after one cycle. For the 8SmZBS coating, the evaporation rate is much higher than the other Sm-doped coatings. The increased rate of convection cell formation will cause the ZrO_2 islands to impinge with each other after covering the entire surface, leaving no room for the formation of petals [20].

(3) Third observation: *Formation of Sm-stabilized t-ZrO2 phase*

The XRD results presented in Figure 4 showed differences in the phase assemblage on the surface of the coatings after each ablation cycle. The crystalline phases present in the ZBS sample after ablation cycles 1 and 2 remain unchanged. The primary phase found in ZBS is m-ZrO_2, with very small amounts of t-ZrO_2 detected. Some t-ZrO_2 phase remained since it was not able to

transform to m-ZrO_2 during the rapid cooling process [21]. For the Sm-doped coatings, the t-ZrO_2 phase is present but at a much higher intensity. The aliovalent Sm^{3+} ions stabilizes the ZrO_2 in a similar way Y^{3+} does and can reduce the formation of m-ZrO_2 on cooling, which typically leads to cracking of the coating [8]. This can be seen with by a peak shift in the larger angle direction of 0.2 2θ in the XRD results. It would be expected to see a shift in a smaller 2θ direction, however the blistering of the sample raised the ablation zone by ~1mm, causing the shift in the opposite direction. The presence of Sm is also verified in the crystalline islands as seen in figure 11. With more Sm dopant present, it is possible to stabilize all the t-ZrO_2 phase, as demonstrated by the 8SmZBS after cycle 1. However, the limited Sm concentration was not able to further stabilize the t-ZrO_2 for the 2nd cycle, which led to the formation of m-ZrO_2. As a result, the coating evidently had formed cracks as illustrated in Figure 2h.

The XRD results have shown that the protective oxide scales formed after ablation for the Sm-doped ZBS coatings on alumina substrates are different than those studies previously performed by Tan et al. [5] on ZBS substrates. Studies for Sm-doped ZBS coatings on ZBS substrates have shown that after ablation there are three main oxide scales formed depending on the samarium percent: m-ZrO_2, c_1-$Sm_{0.2}Zr_{0.8}O_{1.9}$, and $Sm_2Zr_2O_7$. Some beneficial effects of the c_1-$Sm_{0.2}Zr_{0.9}O_{1.8}$ oxides include their high melting point and emissivity, adherence to the unreacted coating during cooling, and formation of a dense oxide scale. Therefore, this cubic fluorite structure oxide scale provides a better ablation resistance than the m-ZrO_2 oxide scale formed on ZBS coatings. The XRD results for Sm-doped ZBS coatings on alumina substrates did not show the c_1-$Sm_{0.2}Zr_{0.8}O_{1.9}$ or $Sm_2Zr_2O_7$ protective oxides scales. Based on the phase diagram presented in Figure 7, small portions of c_1-$Sm_{0.2}Zr_{0.8}O_{1.9}$ compound should be formed with m-ZrO_2 being the main phase. However, the temperature achieved by ablation in this report is ~400°C lower than Tan et al.'s report [5], which may explain the different phases obtained and explain the emissivity difference. The temperature difference also explains why the presently studied coatings did not adhere to the alumina substrate.

Conclusions

Sm-doped ZBS coatings were applied by a shrouded air plasma spray onto alumina substrates and two cycles of 60-second ablation testing was performed. The phase assemblage and microstructure were evaluated after each ablation cycle. The ZBS coating did not exhibit delamination from the alumina substrate or any phase change after each cycle. The ablation of the Sm-doped coatings resulted in a blister forming after the 1st cycle due to a local eutectic reaction occurring between Sm_2O_3, ZrO_2, and Al_2O_3. Higher Sm concentration in the ZBS coatings lowers the viscosity of the glassy phase and increases its evaporation rate. The micrographs show that the size of ZrO_2 islands formed increase with more Sm added after each cycle, as the speed of forming convection cells increases. 5SmZBS coating exhibited flower-like microstructures after the 2nd ablation cycle as a result of the viscous fingering process. The addition of Sm dopant to the ZBS forms a Sm-stabilized t-ZrO_2 phase after ablation, rather than m-ZrO_2. The addition of 8 mol.% of Sm to ZBS can fully stabilize the t-ZrO_2 after a 60-second ablation cycle.

References

[1] T. H. Squire and J. Marschall, “Material property requirements for analysis and design of UHTC components in hypersonic applications,” *J. Eur. Ceram. Soc*., 30[11], 2239–2251 (2010).

[2] F. Monteverde, “The thermal stability in air of hot-pressed diboride matrix composites for uses at ultra-high temperatures,” *Corros. Sci*., 47[8], 2020–2033 (2005).

[3] W. Tan, C. A. Petorak, and R. W. Trice, “Rare-earth modified zirconium diboride high emissivity coatings for hypersonic applications,” *J. Eur. Ceram. Soc*., 34[1], 1–11 (2014).

[4] M. Tului, G. Marino, and T. Valente, “Plasma spray deposition of ultra high temperature ceramics,” *Surf. Coat. Technol*., 201[5], 2103–2108 (2006).

[5] W. Tan, M. Adducci, and R. Trice, “Evaluation of rare-earth modified ZrB2- SiC ablation resistance using an oxyacetylene torch,” *J. Am. Ceram. Soc*., 97[8], 2639–2645 (2014).

[6] W. Tan, M. Adducci, C. Petorak, A. E. Brenner, and R. W. Trice, “Effect of rare-earth dopant (Sm) concentration on total hemispherical emissivity and ablation resistance of ZrB2/SiC coatings,” *J. Eur. Ceram. Soc*.,1–9, (2016).

[7] L. Liu, W. Feng, X. Shi, H Wu and J. Zhu, "Effect of surface ablation products on the ablation resistance of C/C-SiC composites under oxyacetylene torch", *Corros. Sci*., 67, 60–66 (2013).

[8] ASTM E 285-08, "Standard Test Method for Oxyacetylene Ablation Testing of Thermal Insulation Materials." ASTM International, (2008).

[9] F. Tarasi, M. Medraj, A. Dolatabadi, J. Oberste-Berghaus and C. Moreau, “Amorphous and crystalline phase formation during suspension plasma spraying of the alumina-zirconia composite,” *J. Eur. Ceram. Soc*., 31[15], 2903–2913 (2011).

[10] Lakiza, Sergij, and Lydia Lopato. "Phase diagram of the alumina–zirconia–samaria system." *J. Am. Ceram. Soc*., 89[11], 3516–3521 (2006).

[11] W. Fahrenholtz, "Thermodynamic analysis of ZrB2-SiC oxidation: formation of a SiC-depleted region", *J. Am. Ceram. Soc*., 90[1], 143–148 (2007).

[12] X. Zhang, H. Hu and C. J. Han, “Structure evolution of ZrB2-SiC during the oxidation in air”, *J. Mater. Res*., 23[7], 1961–1972 (2008).

[13] M. Farries, P. R. Morkel and J. E. Townsend, “Spectroscopic and lasing characteristics of samarium doped glass fibre”, *IEE Proc. J. (Optoelectronics)*, 137[5], 318–322 (1990).

[14] J. Han, P. Hu, X. Zhang, S. Meng and W. Han. “Oxidation-resistant ZrB2-SiC composites at 2200°C.” *Compos. Sci. and Technol*., 68[3], 799–806 (2008).

[15] S. Gangireddy, S. Karlsdottir, S. Norton, J. Tucker and J. Halloran, "In situ microscopy observation of liquid flow, zirconia growth, and CO bubble formation during high temperature oxidation of zirconium diboride-silicon carbide", *J. Eur. Ceram. Soc*., 30, 2365–2374 (2010).

[16] S. Karlsdottir, J. Halloran and C. Henderson, "Convection patterns in liquid oxide films on ZrB2-SiC composites oxidized at a high temperature", *J. Am. Ceram. Soc.*, 90[9], 2836–2867 (2007).

[17] S. J. Langer, "Dendrites, viscous fingers and the theory of pattern formation", *Science*, 243[4895], 1150–1157 (1989).

[18] F. Monteverde and A. Bellosi, "Oxidation of ZrB2-based ceramics in dry air", *J. Electrochem. Soc*, 150[11], 552–559 (2003).

[19] E. Opila, S. Levine and J. Lorincz, "Oxidation of ZrB2 and HfB2-based ultra-high temperature ceramics: effect of Ta additions", *J. Mater. Sci*., 39, 5969–5977 (2004).

[20] S. Karlsdottir and J. Halloran, "Formation of oxide films on ZrB2-15 vol% SiC composites during oxidation: evolution with time and temperature", *J. Am. Ceram. Soc*., 6, 1328–1322 (2009).

[21] Y. Jia, H. Li, L. Feng,. J. Sun, K. Li and Q. Fu, "Ablation behavior of rare-earth La-modified ZrC coating for SiC-coated carbon/carbon composites under an oxyacetylene torch", *Corros. Sci*., 104, 61–70 (2016).

[22] Z. Chen, R. Trice, H. Wang, W. Porter, J. Howe, M. Besser and D. Sordelet, "Co-doping of air plasma-sprayed yttria- and ceria-stabilized zirconia for thermal barrier applications", *J. Am. Ceram. Soc*, 88[6], 1584–1590 (2005).

Accomplishment 2: In Situ Oxide Scale Investigation of Sm-Doped ZrB_2/SiC Billets

1.0 Introduction

Sharp leading-edge designs for hypersonic vehicles improve performance by reducing aerodynamic drag. However, sharp edges lead to convective heating resulting in temperatures exceeding 2000°C. [1] Ultra-high temperature ceramics (UHTC) are among the materials being considered for leading edges, specifically ZrB2-SiC (ZBS) which has a high melting point and thermal shock resistance at 1500°C and above. [2,3,4]

Studies performed by Tan et. al. [3,6] have shown that adding samarium (Sm) dopant to the ZBS system increases the emittance compared to ceramics comprised only of ZBS. Specifically, in a study where the total hemispherical emittance was tested on a 5 mol% Sm-doped ZBS plasma sprayed coating, it was found to have an emittance of 0.9 at 1600°C. [3] In addition, the Sm dopant improved ablation performance by forming a stable oxide scale of c_1-$Sm_{0.2}Zr_{0.8}O_{1.9}$ (SZO) which has a melting point above 2500°C, making it capable of withstanding extreme temperature conditions during hypersonic flight. Sm was also found to incorporate into the SiO_2 phase lowering the viscosity of the glass. [6] The formation sequence of the oxide scale of Sm-doped ZBS is not understood, thus it was deemed important to investigate. The motivation of this work is to understand the microstructural evolution of the oxide layer and its components during rapid heating in air. In this study, the oxide scale of 3mol% Sm-doped ZBS billets ablated using an oxyacetylene torch were evaluated at 10, 60, and 300s. The phase assemblage and microstructure were analyzed using XRD, SEM, and EDS.

2.0 Experimental Procedure

2.1 Materials and powder preparation

Spray-dried powders were prepared from a suspension that consisted of 80 vol.% ZrB2 (3–5 μm, Grade A, HC Starck, Munich, Germany), 20 vol.% α-SiC (1.4 m, Grade UF-05, HC Starck, Munich, Germany), 0.4 wt.% dispersant (Darvan 821A, R.T. Vanderbilt Company, Inc., Norwalk, USA), 2 wt.% PVA binder (Celvol 203, Celanese Corporation, Dallas, USA) and DI water. Spray drying was performed by Arch Instant Spray Drying Services, Brunswick, GA. The average spray-dried particle size was ~50 μm. Samarium dopant was added to the spray dried ZrB_2/SiC powders via a chemical infiltration method. In this process, 10 mol.% samarium nitrate hexahydrate (99.9% pure Sm(NO3)3·6H2O, Sigma-Aldrich, St. Louis, USA) was dissolved into isopropyl alcohol and the resulting solution was then infiltrated into the porous spray-dried ZrB_2/SiC powder. Next, the solvent was removed via a rotary evaporator (BM 200, Yamato Scientific America Inc., Santa Clara, USA) at 100°C. This powder was heated at 400°C in air for an hour to remove residual moisture and nitrates. Tan et al.[3] showed that below 400°C both the ZBS and the Sm-doped powders did not have any weight gain. As the normalize weight gain was approximate zero below 400°C, it suggests that the oxidation of the powders has little effect during the heat treatment at

400°C. The first weight gain inflections start near 600°C due to the oxidation of ZrB2 to form m-ZrO_2 and B_2O_3 glass [3].

Subsequently, the dried mixture was crushed and sieved using a -325 mesh (40 μm aperture) to eliminate large agglomerates. The powder was then pressed into 38mm x 38mm x 5mm billets at 6 metric tons at room temperature and sandwiched between two SiC plates layered with graphite and sprayed with boron nitride. The purpose of the SiC plates was to avoid bloating of the samples due to outgassing during sintering. The pressed billets were then sintered in argon at 2000°C for 15 minutes (Series System VI, Centorr Vacuum Industries, Nashua, USA). A 1-hr hold at 1650°C, prior to reaching 2000°C, was programed into the heating cycle to evaporate off the boria glass formed from the boron nitride. The densities of the sintered billets was 87±2% and measured by Archimedes' method and compared to a theoretical density of 6.36 g/cm3. The billets had a linear shrinkage of ~20% in x and y and ~40% shrinkage in the thickness. They were then cut to 25.4mm x 25.4 mm and polished using an automatic polisher (GPX Series Advanced Autopolisher, LECO Corp., St. Joseph, USA) to an Ra of 0.4±0.1μm which was measured via atomic force microscopy (AFM). (Dimension 5000 AFM, Bruker, Santa Barbara, USA) The composition of the billets were measured by mass spectroscopy and comprised of 29.8 mol% Zr, 56.7% B, 7% C, 0.5% Si, 3% Sm, 2.8% O, and 0.2% impurities. (NSL Analytical Services Inc., Cleveland, USA)

2.2 Oxyacetylene ablation testing

Heat flux conditions and ablation resistance were assessed using an oxyacetylene ablative torch rig as performed in previous studies. [6] The test rig was constructed using ASTM 285-082 as a standard [7]. The ablation torch (Victor Technologies, St. Louis, USA) used a 5 mm orifice and a separation distance of 20 mm between the sample and the torch tip was kept as a constant. Front and back face temperatures as a function of time were measured using a two-color pyrometer (OS3750, Omega Engineering Inc., Stamford, CT, USA) which was connected to a data logger and thermocouple respectively. The emittance setting for the pyrometer was set to 0.9. An oxygen rich environment was simulated using an oxygen:acetylene ratio of 12:10 slpm. Test specimens were exposed to the flame for 10, 60, and 300 s. The heat flux was measured to be 452 W/cm2 using a thermogage circular foil heat flux gauge (TG1000-4, Vatell Corp., Christiansburg, VA).

2.3 Microstructural and phase analysis

Before performing the microstructural analysis the samples were coated with a thin layer of Au/Pd. A scanning electron microscope (SEM) (Quant 650 FEG, Thermo Fischer Scientific, Hillsboro, USA) was used to characterize coating topography in the as-sprayed conditions after each cycle. X-ray diffraction (XRD) (D8 Focus, Bruker Corporation, Billerica, USA) was used to investigate the phases present. Cu Kα radiation was used over 2θ values of 20°-80° on the coatings after ablation using a step size of 0.02° and a scan rate of 5°/minute. Samples were aligned in the XRD to analyze the regions where the ablation flame was most intense. AFM (Dimension 500

AFM, Bruker, Santa Barbara, USA) was used to measure the pre-ablated average surface roughness (Ra) of the specimens over a 300+ μm2 area in contact mode using a speed of 350 points/second.

3.0 Results

3.1 Pre-Ablated Microstructure and Phase Assemblage

Figure 12a-b show the pre-ablated microstructure of the 87% dense ceramic billet. Figure 13 shows the XRD peaks generated from this surface. The predominant phase is ZrB2,with small peaks coorelating to a SmB2C2 matrix . Small ZrC and SmBO3 peaks are also visible in the pre-ablated XRD scan. The oxidation of the SiC to SiO and CO during sintering coupled with the degradation of Sm2O3 from the pre-sintered powders in the reducing atmosphere is believed to result in the formation of the ZrC, SmB2C2, SmBO3, and loss of SiC in the billets. Similar reactions also occurred with pressurless sintered Y2O3/ SiC. [8] Previous studies on pressureless sintering on ZrB2-SiC ceramics has been with hold times of 1hr+ at similar temperatures that reached densities of 99%. [9] However for our studies it was found that increased hold time had little effect on resultant density.

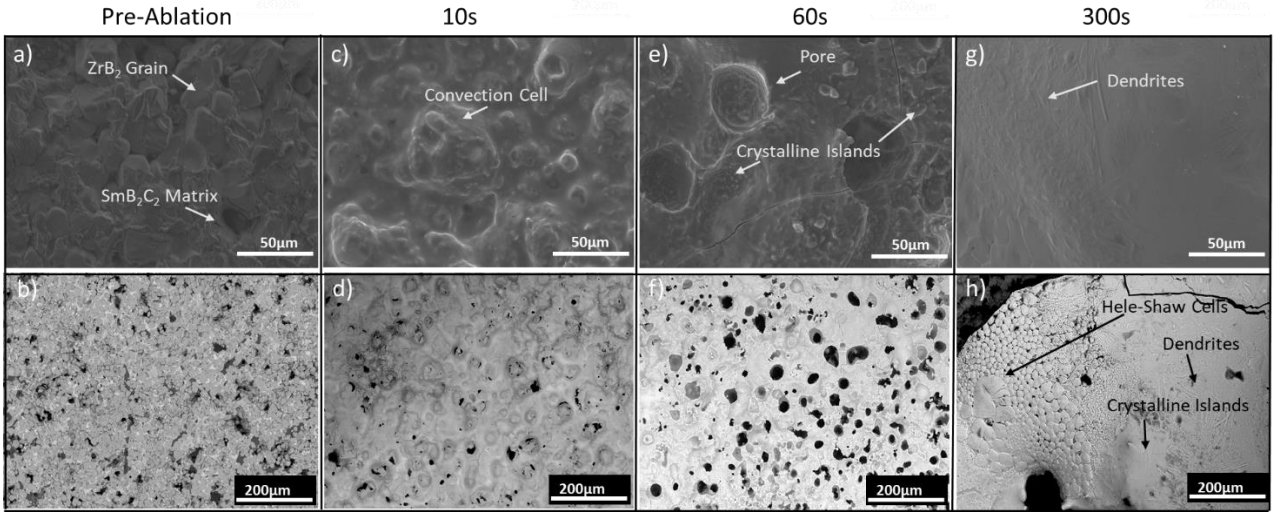

Figure 12: SEM micrographs at different magnifications for pre-ablated billets, 10s post ablated, 60s post ablated, and 300s post ablated. Images A, C, G, and E depict SE imageswhile images B, D, F, and H show BSE images.

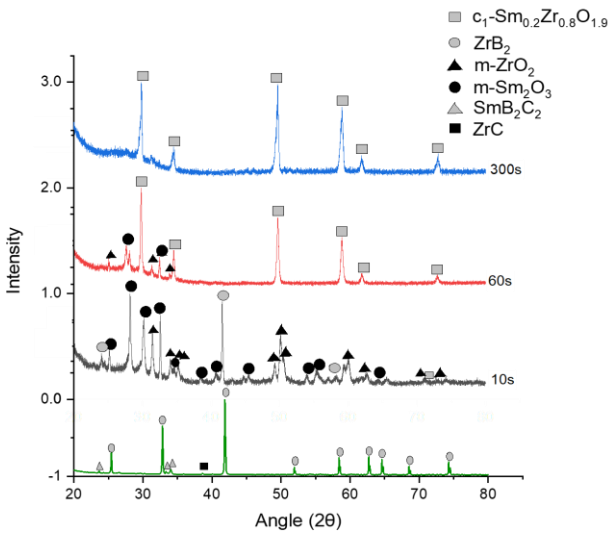

Figure 13: XRD of pre- and post-ablated.

3.2 Weight Gain and Heating Profile as a Function of Ablation Time

Figure 14 shows the front-face sample temperature as a function of ablation time for 10, 60, and 300s holds. The temperature reached after 10s, 60s, and 300s was 1494°C, 1656°C, and 1870°C, respectively. As the emittance of the oxide scale formed is unknown, the pyrometer emittance setting was set to 0.9 which is believed to be higher than the actual emittance of the oxide. Because of the this it is believed the actual temperatures reached are higher than reported. The weight gained after 10s, 60s, and 300s was 0%, 0.8%, and 2.6%, respectively. One possible explanation for 0% weight gain after 10s of ablation is due to the counter loss in weight from B2O3 glass. The inset optical image in Figure 14b shows a white oxide scale indicating little oxidation from of the ceramic billet imaged in Figure 14a. As shown in Figures 14c through d the oxide scale becomes increasingly more yellow as the ablation time increases. It is important to note that the crack in Figure 14c is a result of excessive force used when billet was removed from the sample holder and is not a result of thermal shock. The circles on the optical images indicate where XRD and SEM/EDS analysis were performed.

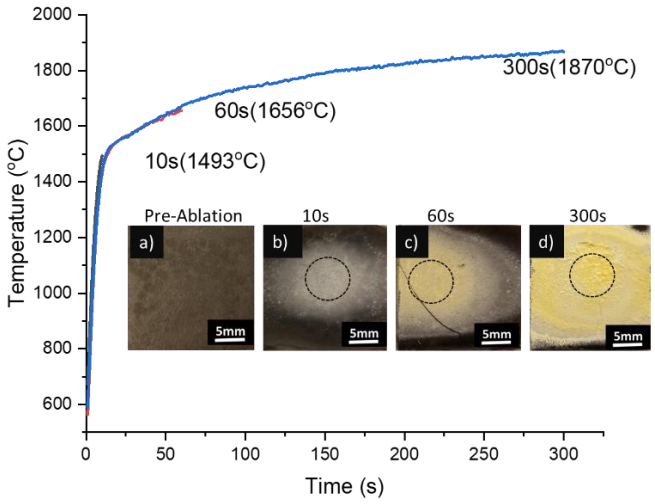

Figure 14: Time vs. temperature graph of ablated samples10s, 60s, and 300s. Optical images are a) before ablation, b) 10s post ablation, c) 60s post ablation, and d) 300s post ablation.

3.3 Post Ablated Samples Contained Sm2O3, ZrO2, and c1-Sm0.2Zr0.8O1.9

XRD analysis, presented in Figure 3, shows the phases present after 10s change from ZrB2 and Sm metal to ZrB2, Sm2O3, and m-ZrO2. Thus, a 10s exposure is sufficient to begin the oxidation process. Furthermore, the presence of an amorphous hump at low 2θ suggests a glassy phase is present on the surface. After 60s, the phases present on the surface are a c1-Sm0.2Zr0.8O1.9 (SZO), Sm2O3, and m-ZrO2. XRD results in Figure 2 shows a single-phase, SZO, after 300s.

3.4 Microstructure Changed with Increased Ablation Time

Figure 12c-d show the formation of convectional cells surrounded by what appears to be a glassy phase after 10s of ablation. Subsequently convectional cells appear to have burst after 60s of ablation as seen in Figures 12e-f. Figure 12g-h show large pores along with a large crystalline region present in the topography after 300s. Dendrites, large grains, and Hele-Shaw cells are visible after 300s as seen in Figure 1h. Hele-Shaw cells appear as round dendritic structures and result from viscous fingering from two fluids of different viscosity. [10] Figure 15 shows cross-sections of the samples after ablation. The oxide scale morphs from a denser oxide scale of ~50μm that is scattered with glassy regions of ~50μm to highly porous ~150μm and ~400μm oxide scales.

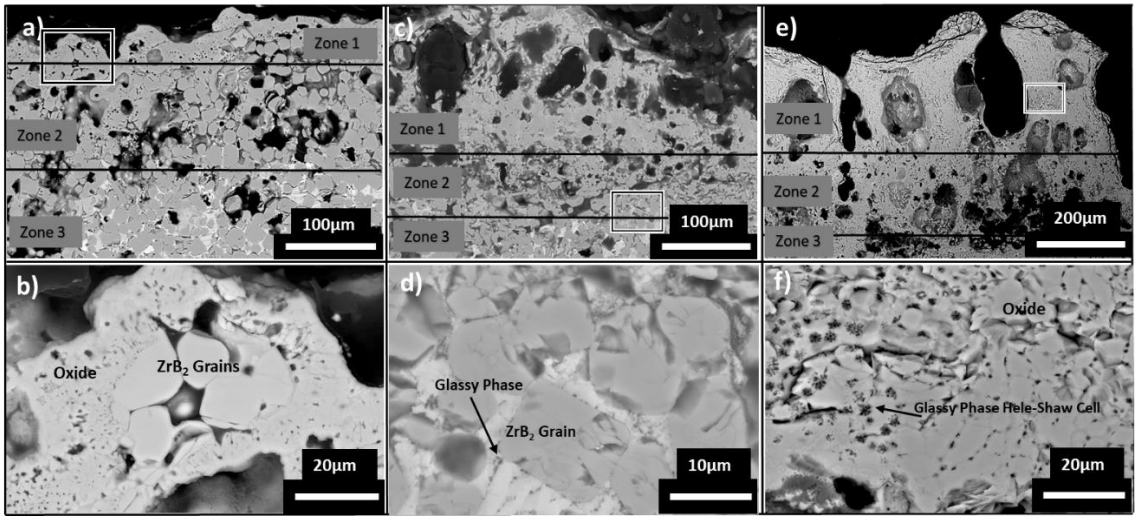

Figure 15: BSE cross-sectional images of a) 10s ablated, c) 60s ablated, and c) 300s ablated. Boxed areas correspond with higher magnified images beneath showing crystalline regions and an intergranular glassy phase in the form of blots after 10s and Saffman-Taylor instabilities post 60s and 300s ablation.

EDS analysis in Figure 16 of these cross-sections reveal high concentrations of Sm and Zr further in the cross-section that gradually diffuse into mixed regions of the two elements. This appears to correlate to SZO. This can be seen in the porous oxide zone, indicated as zone 1 in Figures 15 and 16. Zones are indicated the depth in to the cross section. Zone 2 reveals an intermediate region between the substrate and oxide scale that is higher in density. Figure 16 shows this region is where the Sm and Zr is still in the process of diffusion. After 300s of ablation, zone 2 also shows the depletion of Sm in this region. Zone 3 depicts the substrate of the ablated billets. It should be noted that outside the diffuse Sm/Zr regions, Sm highly associates with O after ablation as well as Si after 60s and 300s of ablation.

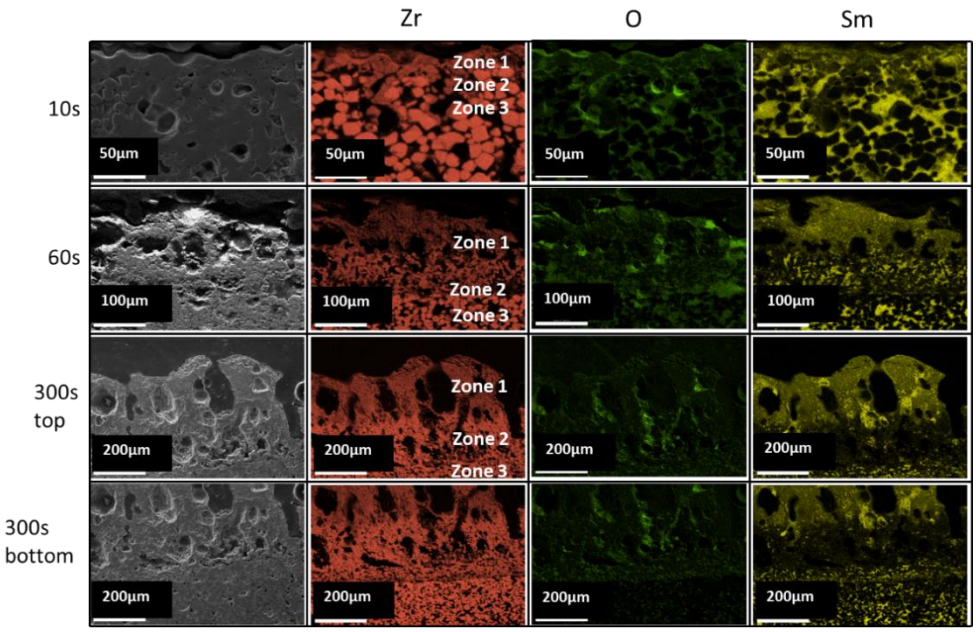

Figure 16: Cross-sectional EDS analysis of billets after 10s, 60s, and 300s of ablation.

4.0 Discussion

4.1 First observation: *Sm-doped samples form SZO from Sm_2O_3 and ZrO_2 and Sm/Zr borosilicates*

In Figure 13 Sm_2O_3 and m-ZrO_2 are present post 10s and 60s of ablation. An amorphous hump is also present after ablation indicating the formation of a glassy phase. The oxidation of the SmB_2C_2 matrix and ZrB_2 grains results in the formation of these two oxides on the surface as well as Sm/Zr-doped B_2O_3/SiO_2 (borosilicate) glass. In ZBS billets oxidized in a furnace for 30 minutes at 1550°C, it was seen that m-ZrO2 islands form dispersed in borosilicate glass. [13] Borosilicate glass also doped with Zr was also seen for oxidized ZBS systems. [14] After 60s of ablation, our sample also reached a similar temperature. Although m-ZrO_2 and Sm_2O_3 could not be seen in EDS analysis on the surface, it is believed they are in the form of nano-oxides in the glassy phase. This was the case for ablated HfB_2/SiC ceramics where nano-oxides of HfO2 were found emulsified in SiO2 glass. [12]

With the addition of Sm_2O_3 to the oxidized system, SZO develops on the surface as seen after 60s as the main oxide present and 300s as the single crystalline phase present in Figure 13. This is due to the combination of Sm_2O_3 and ZrO2. The Sm_2O_3/ZrO_2 phase diagram shows that at ~1700°C and 11 mol% Sm_2O_3, SZO forms. [11] Although we only start out with 3 mol% Sm in the system, there is a concentration of 23 mol% Sm on the surface post 300s of ablation. The increase in Sm is due to the doped amorphous glassy phase being forced to the surface through the formation and bursting of convectional cells which will be described later. This provides enough Sm to form the SZO phase. As the billet is oxidized and B2O3 evaporates off the surface, the Sm concentration increases. Tan et. al. [6] also found a higher concentration of Sm on the surface of

plasma sprayed coatings of Sm-doped ZBS post 60s of ablation. As the boria and silica evaporate, the Sm_2O_3 and m-ZrO_2 become closer in proximity and combine to form SZO.

Below the surface the SmB_2C_2 matrix oxidizes and allows for oxygen to be present to oxidize the ZrB_2 grains. After 10s of ablation as seen in Figure 16, the Sm containing matrix can clearly be seen as being oxidized. Th Zr rich regions remain untouched by the oxygen. It is believed the Sm diffuses with the oxygen and dopes the Zr rich region. In Figure 6 it is clearly seen that the Sm and O concentrations align in the oxidized portion of the ZrB_2 grain. It can also be seen in the oxidized regions of the grain that the regions rich in Zr are doped with Sm. This is clearly evidence of the grain transforming into Sm-doped m-ZrO_2, Sm_2O_3, as well as the start of c1-$Sm_{0.2}Zr_{0.8}O_{1.9}$. In Figure 17 samarium can also be seen starting to dope the Si rich region. As mentioned previously the Sm dopes the Si rich liquid which his forced to the surface between grain boundaries and pores. This is due to the expansion of the oxidizing ZrB_2 grain. The Si region in Figure 6 can clearly be seen liquid sintering the Zr grains together confirming the liquids path of travel. This is the same process for oxide films formed on ZBS. [14]

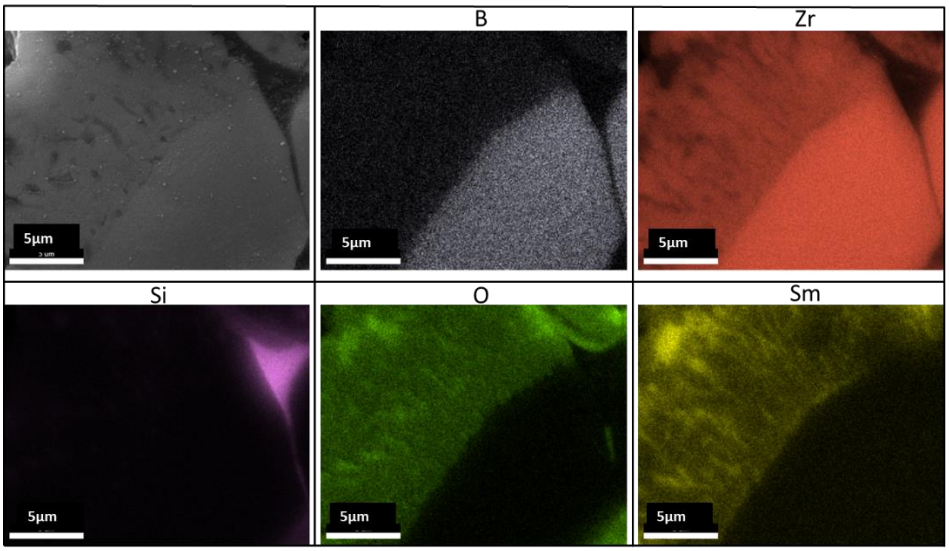

Figure 17: EDS analysis post 10s of ablation of a ZrB_2 grain starting to form Sm_2O_3, ZrO_2, and SZO. Also indicative of the formation of the intergranular Sm-doped silicate glassy phase.

4.2 Second observation: *Amorphous Hele-Shaw cells present in cross-section result from pores and two glasses*

In Figure 4, the glassy phases inhabit areas around the crystalline grains. Figure 15b and 15d show rounded glassy regions after 10s in the oxide scale and under the oxide scale after 60s of ablation. Post 300s of ablation in Figure 15f, evidence of glassy-phase Hele-Shaw cells are present in the oxide scale. This is due to the formation of glasses with different viscosities. Hele-Shaw cells, also known as Staffman-Taylor instabilities, are flower like dendrites formed from the injection of a less viscous liquid into a higher viscous liquid. Porosity is also known to affect the formation of Hele-Shaw cells. [21] These amorphous Hele-Shaw cells were also observed in

Monteverde et. al. [15] and Tan et. al. [5], in ablated LaB_6-ZBS and Sm-ZBS respectively however, they were classified as glass separations.

While oxidation of the ZrB_2 grain is occurring, the SiC is also becoming oxidized forming CO_2 gas and a Sm/Zr-doped B_2O_3- SiO_2 glass. Tan et. al. [5] also had a doped SiO_2 phase, however it was only doped with Sm causing the glass to become less viscous. The evaporation of borosilicate glass changes the viscosity of regions of the glass. This also leaves the doped borosilicate glass with higher concentrations of Sm and Zr in the remaining glass that is not crystalized, but more viscous than the original glass formed. Therefore, evidence of the glass is still seen after 300s. Composition gradients in BSZ liquid is also formed which can be seen in the form of dendrites in previous studies done by Karlsdottir and Halloran. [13] In oxide films formed on ZBS via a 1550°C furnace treatment, it was shown that zirconia islands emerge out of boria-silica-zirconia (BSZ) liquid as the boria evaporates off and a higher viscous liquid remains. [13] The formation of the BSZ glass occurs at a reaction interface and is driven up to the surface due to the volume increase upon oxidation of the bulk material. [14] The glass seen in Figure 15d and 4f is present around grain boundaries and at triple points as seen in the 60s and 300s cross sections relating to reaction interfaces. With the addition of Sm in our system, EDS analysis shows the remnant glassy phase contains both Sm and Zr. This indicates the initial liquid formed during ablation is boria-silica-zirconia-samaira. EDS analysis show this glass is mainly Si, B, and O with Sm and Zr. Different concentrations of Sm and Zr in the glass due to evaporation of the borosilicate is one plausible explanation for different glasses of different viscosities.

4.3 Third observation: *Topography formation derived from convectional cells*

In Figure 12c-d, the topographical microstructure after 10s consists of partially erupted convectional cells. Convectional cells like these were observed by Karlsdottir et. al. [16] in 15vol% SiC-85vol% ZrB_2 that were heated to 1550oC for in air 1 hr. They observed islands of ZrB_2 in lagoons of SiO_2 that were a result of viscous fingering created by borosilicate liquid moving through a more viscous silica rich fluid and across the surface from ZrO_2 columns. It was suggested that the driving force for the flow liquid is from the volume increase due to oxidation as mentioned previously in a similar article. [16] In early oxidative stages, the BSZ liquid flows through the pores of the primary oxidized ZrO_2 porous layer. Later the volume increase induces pressure and stress leading to the rupture of the oxide scale where the liquid is then squeezed up to the surface and flows to form the convectional cells and their features. The rapid evaporation of boria resulted in rapid formation of zirconia precipitated and rapid formation of convection cells. [13] What is seen in 10s post ablated billet is the rapid formation of just what is described, except with the addition of Sm in the system. Evidence of the rupture and formation of convectional cells can be seen in Figure 15a where angular ZrB_2 grains are transforming into what appears to be a porous oxide as described previously. Figure 16 shows cross-sectional EDS analysis after 10s of ablation of a ZrB_2 grain nested in a convectional cell. An Sm-doped Si can be seen liquid sintering the two grains together and the Zr starting to dissolve into the liquid confirming the travel path of the liquid. It can also be seen that the oxygen rich region of the columns contain Zr and Sm. This is

indicative of the viscous fingering described in Karlsdottir etl. al.[16] This is also evidence of the reaction interface for Sm-Zr borosilicate liquid.

After 60s of ablation, it can be seen in Figure 12e that the convectional cells have erupted and large pores where the convectional cells once inhabited propagate the surface. When convectional cells erupt, this reveals a new path for rapid inward oxygen diffusion. [13] This helps explain the increase in oxide scale thickness after 60s and 300s of ablation. It can also be seen in Figure 1f that the oxide islands are larger. It is hypothesized that the oxide islands grow via two methods. The first is the islands start to coalesce with time. Second is grain growth out of the liquid from the formation of SZO out of Sm_2O_3 and ZrO_2 as mentioned previously. As the grains are added to by the liquid and time is increased, rapid grain growth occurs. In Figure 13, after 60s the main phase present is c1-$Sm_{0.2}Zr_{0.8}O_{1.9}$ along with small phases of Sm_2O_3 and ZrO_2. The large crystalline grains Figures 1g and 5b consist of mainly Zr, O, and Sm which correspond to the SZO phase. A glassy phase consisting of a higher concentration of Sm and Si is also present. Cracks can also be seen in Figure 12c possibly due to thermal shock during cooling.

After 300s several different microstructural features are present. From low magnification in Figure 1h, it is obvious that there are large crystalline regions with massive pores which appears to be indicative of coalescence of grains as well as cracks. When magnification is increased dendrites, islands, and large grains of SZO are present as seen in the BSE image in Figure1h. Around each of the mentioned crystalline phases, there is Sm/Zr/Si/O glass as depicted in Figure 18 of EDS of reach of the mentioned regions.

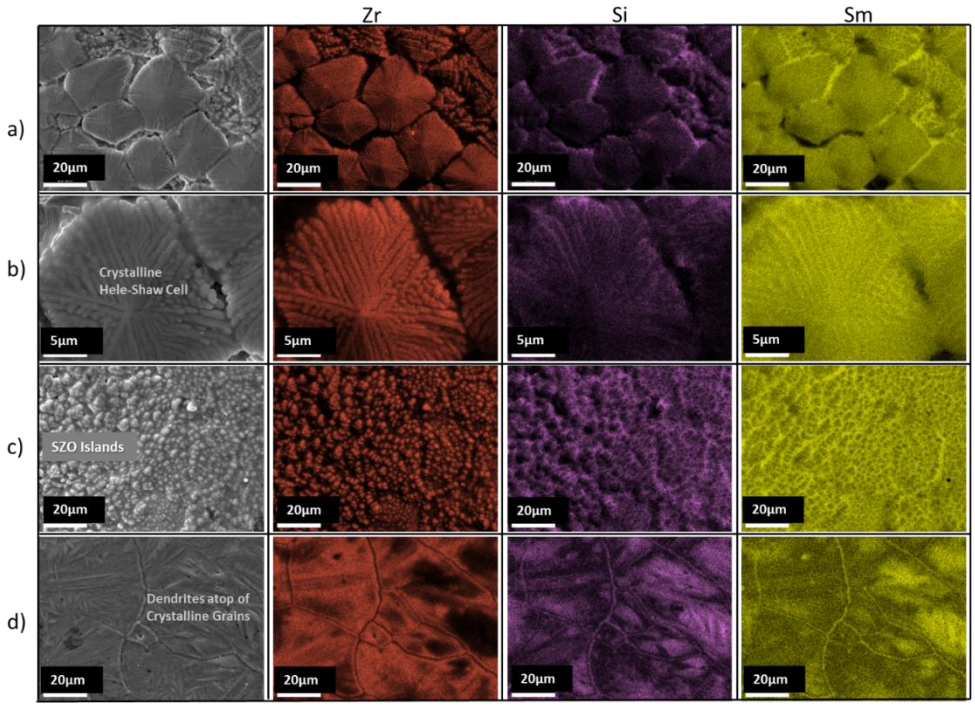

Figure 18: EDS analysis of post 300s of ablation of a) dendritic Saffman-Taylor crystalline instability region, b) higher mage of region, c) oxide island region, and d) large uniform dendritic crystalline phase.

In the large continuously "smooth" crystalline region depicted in Figure 18d, glass dendrites are laced amongst each other. This suggests there was a low quantity of glass atop the surface of this zone that, when undercooled, formed the dendritic structure. This dendritic glass structure due to undercooling can also be seen in studies performed on the immiscible liquid zirconia-silica system. [17] In this large region there are also residual pockets of the Sm/Zr/Si/O glass only visible in BSE and EDS images. This suggests the residual glass has a relatively high evaporation temperature. This similar behavior of the glass is also seen in ZBS doped with yttrium when $Y_2Si_2O_7$ is formed. [19] SZO "islands" are also present in the sample and are surrounded by more of the glassy phase as well as seen in Figure 18c.

In Figure 12h these islands appear to gradually form into the large crystalline region suggesting the coalescing of these islands is the reason for the formation of the large crystalline region. The large grains are also laced with crystalline dendrites. ZrO_2 dendrites were also observed in 8hr furnace formed ZBS oxide scales. [13] It was suggested that the dendrites precipitated from super-saturation of zirconia in BSZ liquid and then coalesced to form the main grains of ZrO_2 is lands. ZrO_2 crystals deposited via a chemical vapor deposition in atmospheric pressure on a silicon substrate were found to destabilize and form a dendritic structure. [18] It is suggested that the destabilization of the oxide is also the case for our c1-$Sm_{0.2}Zr_{0.8}O_{1.9}$ grain edges where the Si dominant amorphous glass is present.

There are also regions of crystalline Hele-Shaw cells surrounded by doped borosilicate glass as seen in Figure 18a-b. However, this network is different than those in the larger crystalline region. Similar dendrites were also observed in 2 cycle ablated ZBS doped with 5mol% Sm on an alumina substrate. [20] In this study the flower-like dendrites of Sm-stablized ZrO_2 were formed via the deposition process of Sm/Al-stablized ZrO_2 precipitating from the lobes boria rich liquid surrounded by silica rich liquid. [20] In this system, a flower with petals pattern was not seen. Dendritic structures like these were also seen in liquid zirconia-silica systems. [17] The dendrites were said to arise as aggregated ZrO_2 surrounded by 2 liquids of different Zr and Si compositions in turbulent conditions. However, the flower-like dendrites observed in this study are characteristic of a Hele-Shaw cell. One possible explanation for this is that the oxide is becoming destabilized from the Si containing glassy phase. It is suggested the destabilized oxide is less viscous than the surrounding evaporating borosilicate glass. However, this material is not well understood, and further investigation is required.

5.0 Conclusion

The microstructural evolution of ablated samarium-doped zirconium diboride/silicon carbide was investigated to understand the formation of the c_1-$Sm_{0.2}Zr_{0.8}O_{1.9}$ oxide layer and its constituent components. It was found that SZO phase is formed by pre-oxide cursors of Sm_2O_3 and ZrO_2 due to the oxidation of ZrB_2 and the samarium containing matrix. Oxygen also seems to be transported with the Sm during ablation first as an oxide then as a glass. The formation of convectional cells and the coalescing of the oxides proceeds to have grain growth and dendritic

structures formed from the amorphous phase as well as destabilization of the amorphous phase. Crystalline and amorphous Hele-Shaw cells were also formed, however the later due to destabilization of the oxide with the silica glass. Future work is being done on forming SZO from Sm_2O_3 and ZrO_2 and the effect of sintering density and surface topography on ablation performance.

References

[1] T. H. Squire and J. Marschall, "Material property requirements for analysis and design of UHTC components in hypersonic applications," *J. Eur. Ceram. Soc*., 30[11], 2239–2251 (2010).

[2] F. Monteverde, "The thermal stability in air of hot-pressed diboride matrix composites for uses at ultra-high temperatures," *Corros. Sci*., 47[8], 2020–2033 (2005).

[3] W. Tan, C. A. Petorak, and R. W. Trice, "Rare-earth modified zirconium diboride high emissivity coatings for hypersonic applications," *J. Eur. Ceram. Soc*., 34[1], 1–11 (2014).

[4] M. Tului, G. Marino, and T. Valente, "Plasma spray deposition of ultra high temperature ceramics," *Surf. Coat. Technol*., 201[5], 2103–2108 (2006).

[5] W. Tan, M. Adducci, and R. Trice, "Evaluation of rare-earth modified ZrB2- SiC ablation resistance using an oxyacetylene torch," *J. Am. Ceram. Soc*., 97[8], 2639–2645 (2014).

[6] W. Tan, M. Adducci, C. Petorak, A. E. Brenner, and R. W. Trice, "Effect of rare-earth dopant (Sm) concentration on total hemispherical emissivity and ablation resistance of ZrB2/SiC coatings," *J. Eur. Ceram. Soc*., 1–9 (2016).

[7] ASTM E 285-08, "Standard Test Method for Oxyacetylene Ablation Testing of Thermal Insulation Materials." ASTM International, (2008).

[8] T. Negano, and K. Kaneko, "Effect of atmosphere on weight loss in sintered silicon carbide during heat treatment," *J. Am. Ceram. Soc*., 83 [11], 2781-2787 (2000).

[9] S. Zhang, G. Hilmas, and W. Farhenholtz, "Pressureless Sintering of ZrB2-SiC Ceramics," *J. Am.Ceram. Soc*., 91[1], 26-32 (2008).

[10] M. B. Amar, and E. G. Poire, "Pushing a non-newtonian fluid in a Hele-Shaw cell:

from fingers to needles," *Phys. Fluids*, 11[7], 1757-1767 (1999).

[11] D. Michel, Y. Rouaux, M. Perez, Y. Jorba, "Ceramic eutectics in the systems ZrO2-Ln2O3: (Ln=Lanthanide): unidirectional solidification, microstructural and crystallographic characterization*," J. Mater. Sci*., 61-66 (1980).

[12] D. D. Jayaseelanm E. Zapata-Solvas, C. M. Carney, A. Katz, P. Brown, and W. E. Lee, "Microstructural evolution of HfB2 based ceramics during oxidation at 1600-2000oC," *J. Advances in Applied Ceramics*, 114, 277-295 (2015).

[13] S. N. Karlsdottir, and J. W. Halloran, "Formation of Oxide Films on ZrB2-15vol% SiC Composites During Oxidation: Evolution with Time and Temperature," *J. Am. Ceram. Soc*., 92 [6], 1328-1332 (2009).

[14] S.N. Karlsdottir, J.W. Halloran, and A.N. Grundy, "Zirconia Transport by Liquid Convection During Oxidation of Zirconium Diboride-Silicon Carbide Composite," *J. Am. Ceram. Soc.*, 91 [1], 272-277 (2008).

[15] F. Monteverde, D. Alfano, and R. Savino, "Effects of LaB6 addition on arc-jet convectively heated SiC-containing ZrB2-based ultra-high temperature ceramics in high enthalpy supersonic airflows," *Corros. Sci*., 75, 443-453 (2013).

[16] S. N. Karlsdottir, J. W. Halloran, and C. E. Henderson, "Convection Patterns in Liquid Oxide Films on ZrB2-SiC Composites Oxidized at High Temperature," *J. Am. Ceram. Soc*., 90 [9], 2863-2867 (2007).

[17] R. Telle, F. Greffrath, and R. Prieler, "Direct Observation of the Liquid Miscibility Gap in the Zirconia-Silica System," *J. Eur. Ceram. Soc*., 35, 3995-4004 (2015).

[18] D. B. Epassaka, S. Ohshio, and H. Saitoh, "Morphological Instability of ZrO2 Crystallites formed by CVD Technique Operated Under Atmospheric Pressure," *J. Mater. Sci*., 38, 3239-3244 (2003).

[19] J. He, Y. Wang, L. Lou, and L. An, "Oxidation Behavior of ZrB2-SiC (Al/Y) Ceramics at 1700oC," *J. Eur. Ceram. Soc*., 36, 3769-3774 (2016).

[20] A. E. Brenner, A. A. Peña, X. L. Phuah, C. Petorak, B. Thompson, and R. W. Trice, "Cyclic Ablation of High-Emissivity Sm-doped ZrB2-SiC Coatings on Alumina Substrates," *J. Euro. Ceram. Soc.,* 38, 1136-1142 (2018).

[21] H. S. Rabbani, D. Or, Y. Liu, C. Lai, N. B. Lu, S. S. Datta, H. A. Stone, and N. Shokri, "Suppressing Viscous Fingering in Structured Porous Media," *PNAS*, 19, 4833-4838 (2018)

Accomplishment 3: Evaluation of Rare-Earth Element Dopants (Sm and Er) on Ablation Resistance of ZrB_2/SiC Sintered Billets

1. Introduction

Hypersonic vehicle design involves the use of sharp leading edges to improve performance and reduce aerodynamic drag.[1,2] During hypersonic flights, a substantial amount of energy is transferred to the vehicle leading edge by convection and chemical heating.3 Convective heating, caused by the high enthalpy bow shock layer, can result in strong thermal shock in the vehicle's sharp leading edges.[1] The atmospheric friction during the reentry process causes the diatoms in the air to separate into ions, which in turn, recombine on the hot surface to release energy resulting in chemical heating.[4] Both processes can heat the leading edge to greater than or equal to 2000°C.

Among the ultra-high temperature ceramics (UHTC) being considered for leading edges, studies have shown that ZrB_2/SiC (ZBS) is a promising material for hypersonic applications due to its high melting point and strength at 1500°C and above, as well as its ablation and thermal shock resistance.[3-6] Despite all of these benefits, ZBS becomes less effective at temperatures above 1600 °C due to the evaporation of the protective glassy oxide layers formed by oxidation of the SiC.[4,7,8] Because of this, finding a means to reduce the surface temperature during hypersonic flight is an urgent issue. Leading edge surface temperatures can be reduced by two ways. A UHTC with a high thermal conductivity is beneficial because it reduces the thermal gradient and the undesirable effects of local hot spots.[4] A UHTC can also reduce surface temperature via radiation.[4] The relevant material property is emittance, with a value approaching that of a black body desired. Studies performed by Tan et al. [3,4,9] have shown that adding Sm dopant to ZBS increases its emittance compared to ceramics comprised of only ZBS. Specifically, a total emittance of 0.9 at 1600 °C was measured for a coating with 5 mol.% Sm dopant and a balance of ZrB_2/SiC.[9] Furthermore, the Sm dopant improved ablation performance by forming a stable oxide scale of c_1-$Sm_{0.2}Zr_{0.9}O_{1.9}$, which has a melting point of 2700 °C, and thus can withstand temperature extremes expected during hypersonic flight.[9]

From a scientific standpoint, it would be helpful if emittance could be tailored at different wavelengths. For example, materials with tailorable emittance could be used to improve the efficiency of engines, thermo-photo voltaic cells, and other applications.[9-11] One approach to creating a ceramic with tailorable emittance would be to use two different rare-earth elements, adding them to a UHTC in small quantities. In this approach, one rare-earth element is added to increase the emittance of the UHTC over a large wavelength range (visible to near infrared wavelengths, consistent with the temperature range expected for hypersonic flight) and another is added to decrease the emittance at specific wavelength range. The end result is a UHTC, in structural or coating form, with selective emittance. Samarium oxide has been shown to have a high emittance from visible to near IR wavelengths.[12,13] Erbium oxide has a demonstrated low emittance in several wavelength ranges, specifically in the 0.7-0.8 μm, 1–1.1 μm, and 1.7-1.8 μm ranges.[13]

With this in mind, the goal of this study was to dope a UHTC with two rare-earth elements, employing both samarium and erbium, to evaluate the effects of Sm and Er atoms on the ablation resistance of ZBS systems in dynamic environments. Thus, for this study, ZBS billets co-doped with Sm and Er atoms in five different ratios were prepared, with the nominal total dopant concentration constant at 3 mol.% as showed on the Tan et al.[9] study. These samples were evaluated via ablation testing for 60s and 300s using an oxyacetylene torch to evaluate how the Sm and Er dopants affect the oxidation process, and the final oxide phase(s) stability and development, to produce an UHTC that possess a tailorable emittance, strong thermal shock and ablation properties, and a high melting point.

2. Experimental Procedure

2.1 Materials and powder preparation

Spray-dried powders were prepared using the same method employed by Tan et al.[4,9] and the Brenner et al.[20] studies. Briefly, a lab spray dryer (APV Anhydro Model S1, Anhydro Inc, Soeborg, Denmark) was used to produce powder agglomerate from a liquid suspension feed (Aero-Instant Spraying Service, Brunswick, USA) that consisted of 80 vol.% ZrB2 (3–5 μm, Grade A, HC Starck, Munich, Germany), 20 vol.% α-SiC (1.4 m, Grade UF-05, HC Starck, Munich, Germany), 0.4 wt.% dispersant (Darvan 821A, R.T. Vanderbilt Company, Inc., Norwalk, USA), 2 wt.% PVA binder (Celvol 203, Celanese Corporation, Dallas, USA) and deionized water. The suspension was fed into the drying chamber by using a spraying nozzle, where the air was heated to 200 °C. Next, a rotary atomizer spun at ~30,000 rpm was used to atomize the suspension into controlled-size droplets. The temperature at the outlet was ~105 °C. The average particle size of the spray-dried particles, which was obtained by using a Malvern Mastersizer 2000 (Malvern Instrument Ltd., Worcestershire, UK), was approximately 38 μm. Figure 1 shows a SEM micrograph of the undoped spray dried ZrB2-20 vol% SiC particles.

Samarium and/or erbium dopants were added to the spray dried ZrB2/SiC powders via a chemical infiltration method. In this process, samarium nitrate hexahydrate (99.9% pure $Sm(NO_3)_3 \cdot 6H_2O$, MSE Supplies, Arizona, USA) and/or erbium nitrate hexahydrate (99.9% pure $Er(NO_3)_3 \cdot 6H_2O$, MSE Supplies, Arizona, USA) were dissolved into 99.9% pure isopropyl alcohol, and the resulting solution was then infiltrated into the porous spray-dried ZrB_2/SiC powder. Solutions mixed in five different molar ratios (1Sm:0Er, 2Sm:1Er, 1Sm:1Er, 1Sm:2Er and 0Sm:1Er) were prepared; the total rare-earth nitrate hexahydrate compound was added at an initial concentration of 10 mol.%. Next, the alcohol and likely some of the water was removed via a rotary evaporator (BM 200, Yamato Scientific America Inc., Santa Clara, USA) at 100°C. This powder was heated at 500°C in air for an hour to remove residual moisture, water, and nitrates. Tan et al.[4] performed a study of the normalized weight gain as a function of temperature from 200-1300°C demonstrating that below 600 °C both the ZBS and the Sm-doped coatings exhibit no weight gain that would be associated with oxidation. As the normalized weight gain was ~0 below 600 °C, it suggests that the oxygen content does not increase during the heat treatment at 500 °C. These results are consistent with temperature transitions reported by Bartuli et al.[14] for ZrB_2/SiC

coatings, providing further evidence that the ZBS and the Sm-doped coatings did not have any weight gain below 600 °C. The first weight gain inflections start near 600°C due to the oxidation of ZrB_2 to form m-ZrO_2 and B_2O_3 glass.[4] After nitrate, water and moisture removal at 500°C, the dried mixture was sieved using a 60-mesh (250 μm aperture) to eliminate large agglomerates. For ZBS powders/dopant ratios, ~20% by weight was lost during the 500oC heat treatment. These losses are due to the evaporation of the nitrates and water. ZBS powders with different ratios of Sm and/or Er dopants were die pressed at 82 MPa. The pressed billets were heated to 1650 ^oC, held for 1 hr, heated to 2000 °C, held for 15 min, then cooled to room temperature. Sintering occurred in an argon atmosphere with graphite heating elements at a partial oxygen pressure of 10-7 ppm. Samples were cut into 25.4 mm x 25.4 mm squares.

The billets were polished to ~0.1 μm using an auto polisher, where the billets were polished first to 6 μm, then to 3 μm, and finally to 0.1 μm. The bulk density of each billet for each ratio of Sm:Er was measured by the Archimedes methodology as described in the ASTM C373-88 standard. Surface roughness (Ra) was measured using an AFM (AS0200 AlphaStep, Tencor Corporation, Milpitas, USA). To help simplify discussion, the naming convention is on the intended molar ratios. For instance, the 2Sm:1Er billet was to contain 6.66 mol.% $Sm(NO_3)_3 \cdot 6H_2O$ and 3.33 mol.% $Er(NO_3)_3 \cdot 6H_2O$ in the ZrB_2/SiC matrix. The amount of Sm and Er incorporated into the samples was measured by ICPMS with fusion preparation on pulverized billets (NSL Analytical Services Inc., Cleveland, USA).

2.2 Oxyacetylene Ablation Testing

Heat flux conditions and ablation resistance were assessed using an oxyacetylene ablative torch rig. The test rig was constructed using ASTM E285-082 as a standard.[15] The ablation torch (Victor Technologies, St. Louis, USA) used a 5 mm orifice and a separation distance of 20 mm between the sample and the torch tip was held constant. An oxygen rich environment was simulated using an oxygen:acetylene ratio of 12:10 slpm. The heat flux was measured to be 452 ± 6.8 W/cm^2 using a thermogage circular foil heat flux gauge (TG1000-4, Vatell Corp., Christiansburg, VA). The circular-foil heat flux gauge have a water-cooler system which continuously provides an active heat sink that removes the absorbed heat, especially for applications with longer measurement times or high heat flux levels. Also, the thermogage sensor is coated with colloidal graphite. Front surface temperatures as a function of time were measured using a single-color pyrometer (OS3750, Omega Engineering Inc., Stamford, CT, USA) which was connected to a data logger. The single-color pyrometer has a target size for temperature measurements of 20 mm diameter which was positioned on the sample where the flame was the hottest. The maximum temperature values from the target size area were measured at a spectral band of 1.55 μm and reported with an accuracy rating of ±1.2% from the measured value. The emittance setting for the pyrometer was set to be 0.9. Five test specimens were exposed to 60s and other five test specimens to 300s intervals of flame. Samples were cooled to room temperature and characterized.

2.3 Microstructural and Phase Analysis

Before performing the microstructural analysis, the samples were coated with a thin layer of Au/Pd. A scanning electron microscope (SEM) (Phillips XL-40, FEI Co., Hillsboro, USA) was used to characterize billet topography in the pre-ablated and post-ablated conditions. X-ray diffraction (XRD) (D8 Focus, Bruker Corporation, Billerica, USA) was used to identify the phases present using Cu Kα radiation for 2θ values of 20°-80° on the billets before ablation, and for 2θ values of 15°-80 after ablation. A step size of 0.02° and a scan rate of 5°/minute was used for all samples. Samples were positioned in the XRD to analyze the regions where the ablation flame was most intense.

3. Results

3.1 Pre-ablated Sintered Samples Results

The actual concentrations of Sm (mol.%) and Er (mol.%) incorporated into each billet are listed in Table 3, along with the measured bulk density, theoretical density, total porosity (%), and surface roughness. It was observed that ~3 mol.% rare-earth element(s) were incorporated into the sintered billets, ~1/3 of the 10 mol.% rare-earth nitrate hexahydrate compounds during the chemical doping process. It should be noted that most of this reduction in the dopant concentration was caused by the heat treatment at 500°C where the water and nitrates were removed, and not because the Sm and Er were lost. Recall that the 10 mol.% added during the chemical doping process is referring to the combined $Sm(NO_3)_3{\cdot}6H_2O$ and $Er(NO_3)_3{\cdot}6H_2O$. Therefore, the combined concentrations of Sm (mol.%) and Er (mol.%) represents ~35% (~3.5 mol.%) of 10 mol.% added during the chemical doping process. As ~3 mol.% dopant(s) were incorporated into the sintered billets, it can be concluded that the reminder ~0.5 mol.% was lost during powder handling or during sintering. These results are different than the ones presented in Tan et al.[4,9] studies and Brenner et al.[16] study where 5 mol.% Sm dopant was incorporated into plasma-sprayed coatings. The decrease of the ~2 mol.% of the dopant(s) incorporated into the sintered billets of the present study were caused by the different method used to prepare the samples, as the samples used in Tan et al.[4,9] studies and Brenner et al.[16] study were prepared using a plasma spray process.

	$Sm(NO_3)_3{\cdot}6H_2O$ Added (mol%)	$Er(NO_3)_3{\cdot}6H_2O$ Added (mol%)	Actual Sm Incorporated (mol%)	Actual Er Incorporated (mol%)	Densification level (%)	Bulk Density (g/cm^3)	Volume of Open Porosity (cm^3)	Surface Roughness, Ra (nm)
1Sm:0Er	10	0	2.94	0		3.91	0.76	102 ± 12
2Sm:1Er	6.6	3.3	1.85	1.23		4.74	0.72	95 ± 15
1Sm:1Er	5	5	0.97	1.80		4.77	0.03	105 ± 14
1Sm:2Er	3.3	6.7	0.95	2.33		4.82	0.72	108 ± 8
0Sm:1Er	0	10	0	3.11		4.97	1.23	104 ± 11

Table 3: Samarium and erbium dopant concentration and properties after sintering.

Table 3 shows more Er dopant was integrated into the sample than the Sm dopant. This is apparent by comparing the 1Sm:0Er and 0Sm:1Er billets, where 2.94 mol.% of Sm and 3.11 mol.% or Er were incorporated respectively. This difference is explained by the differences in their molar mass, where Sm represents the 33.8% of the 10 mol.% $Sm(NO_3)_3 \cdot 6H_2O$ added during the chemical doping process for the 1Sm:0Er billet, whereas Er represents 36.3% of the 10 mol.% $Er(NO_3)_3 \cdot 6H_2O$ added for the 0Sm:1Er billet. Surface roughness (Ra~100 nm) were all similar, consistent with using the same polishing procedures for each billet investigated. Samples ranged in total porosity from 17 to 31%.

XRD results on the billets before ablation testing presented in Figure 19 indicated ZrB2 is the majority phase with a small peak at 35.5° identified as α-SiC. For the 1Sm:0Er and 0Sm:1Er samples, the small intensity peaks between 2θ of 23-35.5° correspond to Sm2O3 and Er2O3 respectively. For the 2Sm:1Er, 1Sm:1Er, and 1Sm:2Er pre-ablated samples, the XRD results shows a similar $(Sm/Er)_2O_3$ phase due to the Sm and Er atoms exchanging positions because of their similar ionic size (242 pm for Sm and 236 pm for Er). The peaks were shifted to larger 2θ due to the smaller interplanar spacing caused by the slightly smaller erbium atoms. As was noted in the XRD results, the Sm and Er compounds and alloys oxidized to some extent in the high purity Ar atmosphere during the sintering process.

Figures 20a-e compare the SEM micrographs of the surface of the billets before the ablation testing. The XRD results in Figure 19 indicating the primary phase to be ZrB2 were further verified by EDS results for each sample which showed ZrB2 grains of approximately a 1:2 ratio of Zr to B atoms. The grains were surrounded by a matrix composed of mainly Sm and Er with small portions of O, Si, and C. The small portion of Si and C in the EDS results also matches with the small α-SiC peak identified at 35.5° in the XRD plot in figure 19.

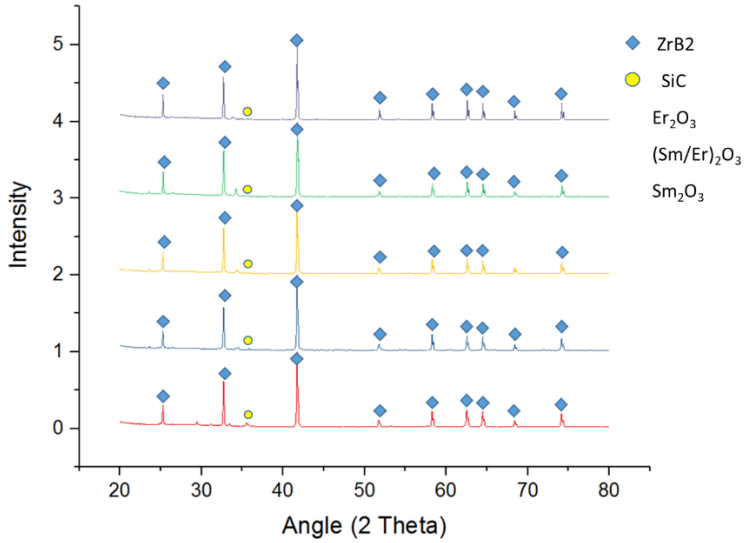

Figure 19: X-ray diffraction patterns of the surface of the pre-ablated sintered samples.

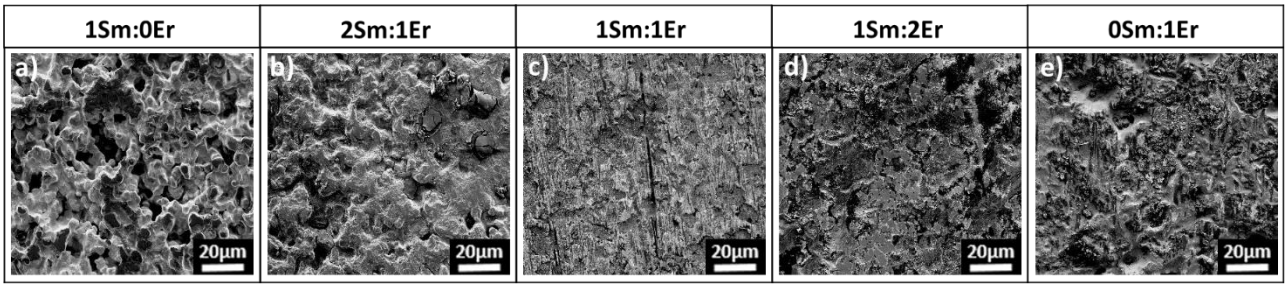

Figure 20: SEM electron micrographs of the surface of the pre-ablated sintered billets

3.2 Ablation Results After 60s

Figure 21a shows a plot of front surface temperature as a function of time during the 60s ablation cycle for each of the five billets tested. All the samples displayed a continuous temperature increase through the 60s of heating, with a rapid increase in temperature followed by a much slower increase in temperature. The maximum temperatures during the ablation cycle were the highest for the 0Sm:1Er and 1Sm:2Er samples at 1717 ± 21°C and 1715 ± 21°C respectively, and the lowest for the 2Sm:1Er sample at 1612 ± 19°C. The maximum temperatures for the 1Sm:0Er and 1Sm:1Er samples were 1690 ± 20°C and 1672 ± 20°C, respectively. The temperature at which the rate of heating slows down is different for all the samples. The inflection point temperature was the highest for the 0Sm:1Er sample at 1600 ± 19°C after ablating for 12s, and the lowest for the 2Sm:1Er sample 1300 ± 16°C after ablating for 9s.

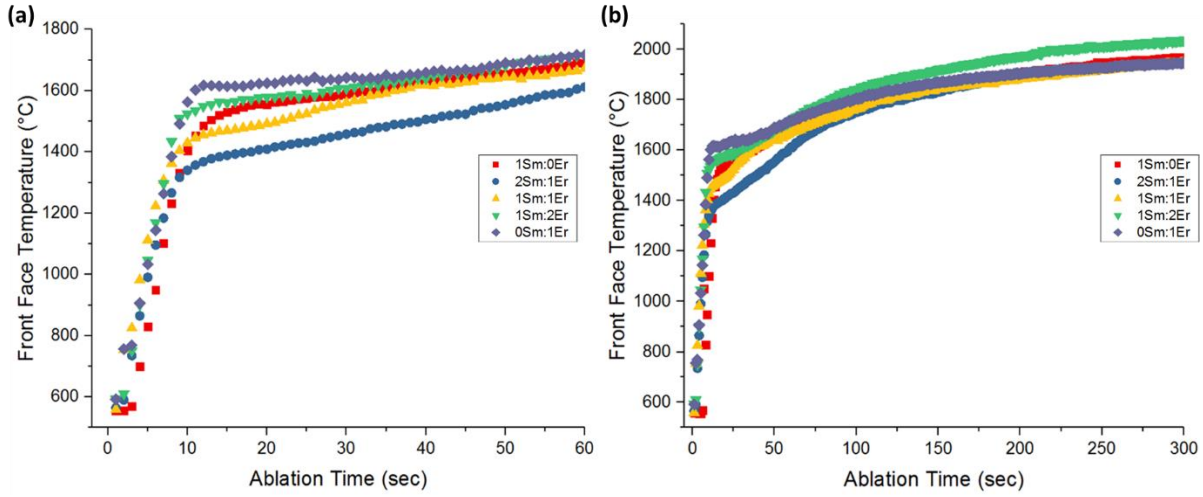

Figure 21: Front face temperature during ablation testing for (a) 60s and (b) 300s. for: a) 1Sm:0Er, b) 2Sm:1Er, c) 1Sm:1Er, d) 1Sm:2Er, and e) 0Sm:1Er.

Figures 22a-e compare the ablated surfaces after the 60s ablation cycle. Each of the Sm:Er billets developed an adherent oxide scale. The oxide scale color changes relative to the amount of Sm and Er dopant from yellow in the 1Sm:0Er sample to pink in the 0Sm:1Er sample.

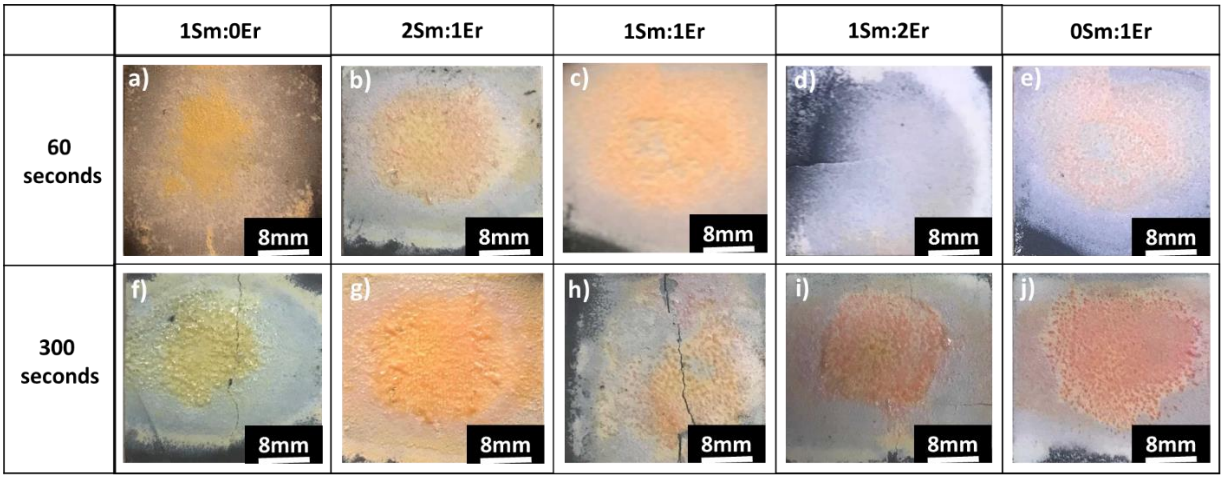

Figure 22: Optical images of the ablated billets: a) 1Sm:0Er, b) 2Sm:1Er, c) 1Sm:1Er, d) 1Sm:2Er, and e) 0Sm:1Er after 60s, and f) 1Sm:0Er, g) 2Sm:1Er, h) 1Sm:1Er, i) 1Sm:2Er, and j) 0Sm:1Er

Figures 23a-e compare SEM micrographs of the surface of the billets after ablating for 60s. For all the Sm:Er samples, the surface appears to have clusters of crystalline islands surrounded by an amorphous phase. Figures 6a-c show that the crystalline islands become larger as the Sm concentration is increased from 0.97 mol.% in the 1Sm:1Er sample to 2.94 mol.% in the 1Sm:0Er sample. Additionally, the 1Sm:1Er billet shows the presence of pores and dendrites, while the 1Sm:0Er billet shows a "flower-like" microstructure.

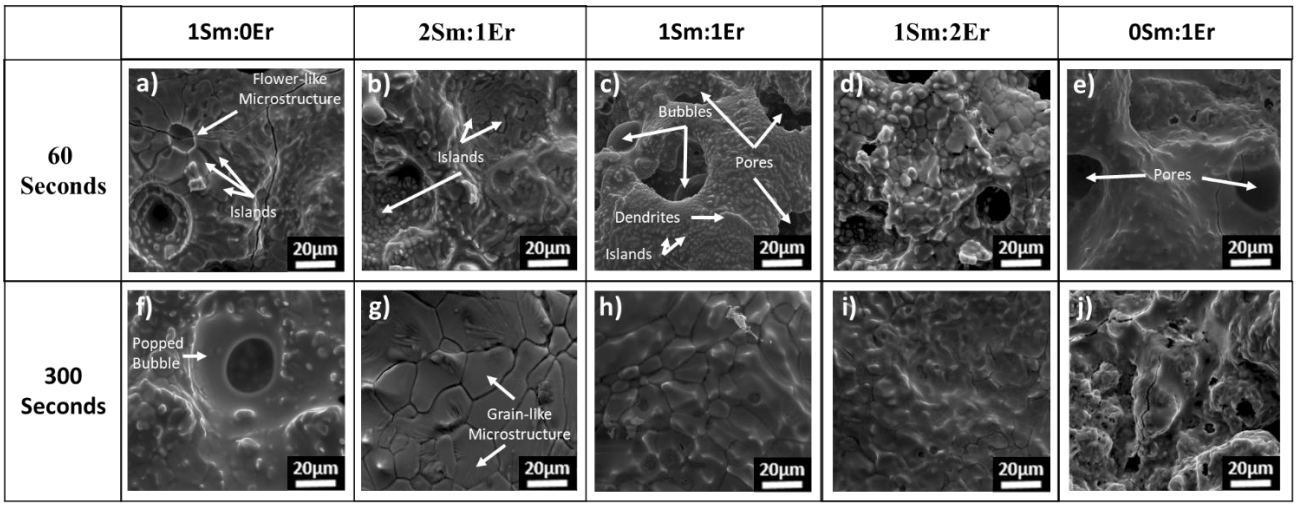

Figure 23: SEM electron micrographs of the following billets: a) 1Sm:0Er, b) 2Sm:1Er, c) 1Sm:1Er, d) 1Sm:2Er, and e) 0Sm:1Er after 60s, and f) 1Sm:0Er, g) 2Sm:1Er, h) 1Sm:1Er, i) 1Sm:2Er, and j) 0Sm:1Er after 300s.

The post-ablation XRD results for the 1Sm:0Er sample presented in Figure 24a match with previous studies[9], where the major phase formed was the cubic samarium zirconium oxide scale

(c_1-$Sm_{0.2}Zr_{0.8}O_{1.9}$, JCPDS-01-78-1302). For the ablated 2Sm:1Er, 1Sm:1Er, and 1Sm:2Er billets samples, the XRD results shows a similar cubic structure (c_1-$(Sm/Er)_{0.2}Zr_{0.8}O_{1.9}$) as the major phase due to the Sm and Er atoms exchanging positions because of their similar ionic size (242 pm for Sm and 236 pm for Er). The primary peaks were shifted to larger 2θ due to the smaller interplanar spacing caused by the slightly smaller erbium atoms. Lattice parameters of 0.517 nm, 0.513 nm, 0.511 nm, 0.510 nm, and 0.507 nm were measured for c1-(Sm/Er)0.2Zr0.8O1.9 for the 1Sm:0Er, 2Sm:1Er, 1Sm:1Er, 1Sm:2Er and 0Sm:1Er samples, respectively. These results follow the Vegard's law as the interplanar spacing decrease almost linearly as the Sm dopant concentration is increased. Small portions of monoclinic zirconia (m-ZrO_2, JCPDS-00-37-1484) were also observed. Finally, the ablated 0Sm:1Er sample was primarily cubic erbium zirconium oxide scale (c_1-$Er_{0.2}Zr_{0.8}O_{1.9}$) with small amounts of m-ZrO_2.

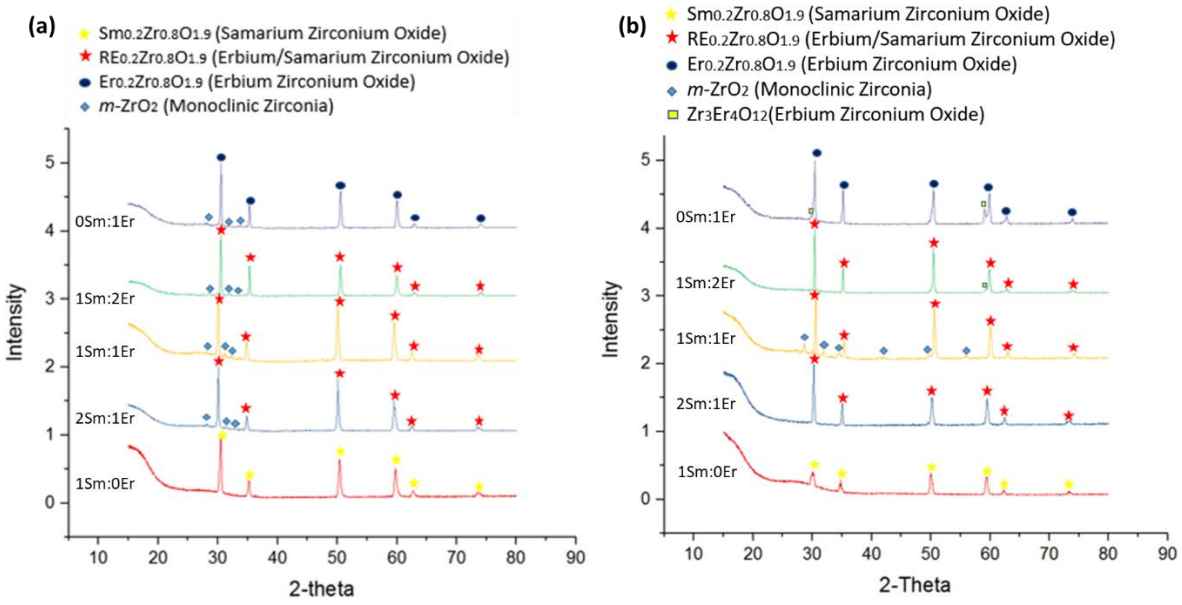

Figure 24: X-ray diffraction patterns of the surface after (a) 60s and (b) 300s ablation cycles.

3.3 Ablation Results After 300s

The ablation results of the samples evaluated for 60s were compared with the first 60s of the samples ablated for 300s to test the variation of the temperature measurements with time. The standard deviation of each time point was calculated, and then, these 60 standard deviation values were used to calculate their 95% confidence interval. The variations of the temperature measurements were small, varying from 37 ± 4.2 °C, 8.8 ± 4.3 °C, 8.3 ± 4.1 °C, 5.9 ± 3.2 °C, and 8.1 ± 4.2 °C for the compositions 1Sm:0Er, 2Sm:1Er, 1Sm:1Er, 1Sm:2Er, and 0Sm:1Er respectively.

Figure 21b shows the front surface temperature during the 300s ablation cycle. The maximum temperature during the ablation cycle was the highest for the 1Sm:2Er sample at 2037

± 24°C. Maximum temperatures of 1968 ± 24°C, 1946 ± 23°C, 1947 ± 23°C and 1947 ± 23°C were measured for the 1Sm:0Er, 2Sm:1Er, 1Sm:1Er, and 0Sm:1Er samples, respectively. During the first 100s of ablation, the 2Sm:1Er sample showed the lowest front face temperature. Excluding the 1Sm:2Er sample, the temperature difference between the other 4 compositions studied after ablation for 100s seem to be very similar. All the samples displayed a continuous temperature increase through the 300s of heating but were significantly hotter (~300°C) than the samples ablated for 60s. As the ablation time is increased from 60s to 300s, a second inflection point, in addition to the first one previously described, can be seen for all the five Sm:Er molar ratios. The inflection point occurs at approximately 1700 ± 20°C after ablation for 75s.

Figures 22f-j show the ablation surface micrograph comparison of the samples after the 300s ablation cycle. Each of the Sm:Er billets developed an adherent oxide scale. The oxide scale color changes relative to the amount of Sm and Er dopant as in the 60s ablation cycle from yellow in 1Sm:0Er to pink in 0Sm:1Er. It was observed that more amorphous phase was present when the ablation time was increased from 60s to 300s. It should be noted that the cracks shown on the 1Sm:0Er and 1Sm:1Er samples were caused by removing the samples from the ablation rig.

Figures 23f-j present the surface topography of the ablated samples after 300s. The crystalline islands observed in the first 60s of ablation for the 2Sm:1Er, 1Sm:1Er, and 1Sm:2Er samples, have increased in size and coalesced. Therefore, a grain like-structure is evident in the three samples containing both Sm and Er dopants (Figures 23g-i), whereas a glassy phase is covering the crystalline grain-like structure. The amount of glassy phase on these three samples appears to increase as the Er concentration increases. On the contrary, the 1Sm:0Er and 0Sm:1Er samples did not show the grain-like structure. Figure 23f shows that in the 1Sm:0Er sample the crystalline islands formed after 60s have increased in size but maintained the amorphous lagoon surrounding them. Figure 23j shows that the 0Sm:1Er sample have a similar microstructure as the 1Sm:0Er.

Figure 24b shows the XRD results obtained from the surface of the samples after the 300s ablation cycle. The XRD of the samples after ablation for 300s remains unchanged, being primarily composed of c_1-$(Sm/Er)_{0.2}Zr_{0.8}O_{1.9}$ as the major phase with small amounts of m-ZrO_2 observed. More amorphous phase, as evidenced by the humps in the Figure 24b XRD data, is apparent after 300s of ablation.

A typical EDS line-scan for sample ablated for 300 s is shown in Figure 25. For the 2Sm:1Er sample shown the Sm and Er dopant concentration is much higher at the ablated surface (x=0 μm) than in deeper regions of the billet. The average Sm and Er concentration between x=0-75μm (within the oxide scale), as shown in Figure 25, is ~30 wt.% for Sm and ~20 wt.% for Er. The c_1-$Sm_{0.2}Zr_{0.8}O_{1.9}$ phase requires ~23 wt.% Sm to form, whereas the c_1-$Er_{0.2}Zr_{0.8}O_{1.9}$ phase requires ~20 wt.% Er to form. As the distance from the ablated surface is further increased, the average combined Sm and Er concentration between x=75-250 μm as shown in Figure 25, is ~16 wt.%. It is worth noting that the concentration difference between Sm and Er decreases as the distance from the ablated surface is increased. On the contrary, the Zr concentration is much lower at the ablated surface than in deeper regions of the billet. The average Zr concentration between x = 0 – 75 μm (within the oxide scale), as shown in Figure 8, is ~45 wt.%. As the distance from the

ablated surface is further increased, the average Zr concentration between x=75-250 μm is ~75 wt.%. Based on the Figure 25 EDS line-scan, it can be concluded that as the distance from the ablated surface is increased, the amount of the c_1-$(Sm/Er)_{0.2}Zr_{0.8}O_{1.9}$ phase decreases, and the amount of the m-ZrO_2 phase increases.

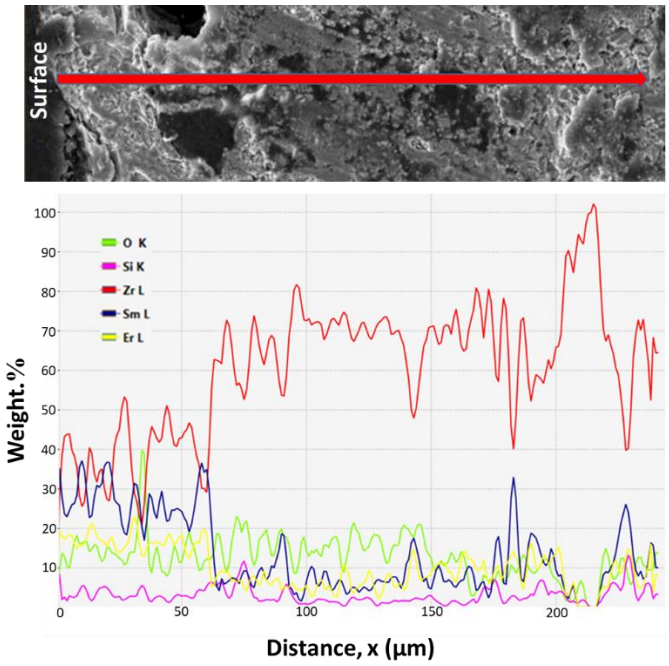

Figure 25: EDS line-scan for the 2Sm:1Er sample after 300s ablation cycle and the wt.%

4. Discussion

4.1 First observation: *The beneficial samarium/erbium zirconium oxide scale noted after ablation for 60s and 300s is formed by a convection cells mechanism*

This study investigates the ablation properties of the oxide scales formed during ablation when emittance modifiers of Sm and Er are added. The crystalline and amorphous phases observed in Figure 23 are being formed by a convection cell mechanism. These convection cells were noted by Karlsdottir et al.17 for ZrB_2/SiC coatings during oxidation at 1550°C as a flower-like microstructure. The study described the "islands" (center regions of the flower-like structure) to be m-ZrO_2, the "petals" to be B_2O_3 glass, and the "lagoon" regions to be SiO_2 glass.17 The formation of the flower-like structure is caused by the viscous fingering phenomenon, which is the displacement of a less viscous liquid.17,18 Due to the instability of the moving interface, the less viscous B_2O_3 liquid displaces a more viscous SiO_2 liquid.17-19 The rising B_2O_3 rich liquid contains dissolved ZrO_2, which deposits in the center of the flower-like structure when the B_2O_3 evaporates. The liquid boria-rich oxidation product is transported through the overlying layer of SiO_2 liquid by convection, forming convection cells aligned like the petals of a flower.[17-20]

Brenner et al.[16] also noted these convection cells during the oxidation of Sm-doped ZrB_2/SiC coatings at ~1700 °C. Even though the convection cells mechanism during the ablation

process in the present study was very similar compared to both Brenner et al.[16] and Karlsdottir et al.[17,18,21] studies, the final ablation product is different. The addition of Sm dopant to the ZrB_2/SiC coatings in Brenner et al.[16] study formed a Sm-stabilized t-ZrO_2 phase after ablation, whereas the Karlsdottir et al.[17,18,21] studies final product was m-ZrO_2. Studies have shown that the B_2O_3 glass present on the surface of a Sm-doped ZrB_2/SiC coating after heating to 900 °C contains Sm3+ atoms.9 It is expected that the B_2O_3 glass formed in the present study would not only contain Sm^{3+} atoms but also Er^{3+} atoms. This was confirmed by the SEM-EDS image shown in the Figure 26a, where 31.0, 59.1, and 47.4 wt.% of Sm were detected in zones A-C respectively; while 71.0 and 51.0 wt.% of Er were detected in zones A-B in the Figure 26b.

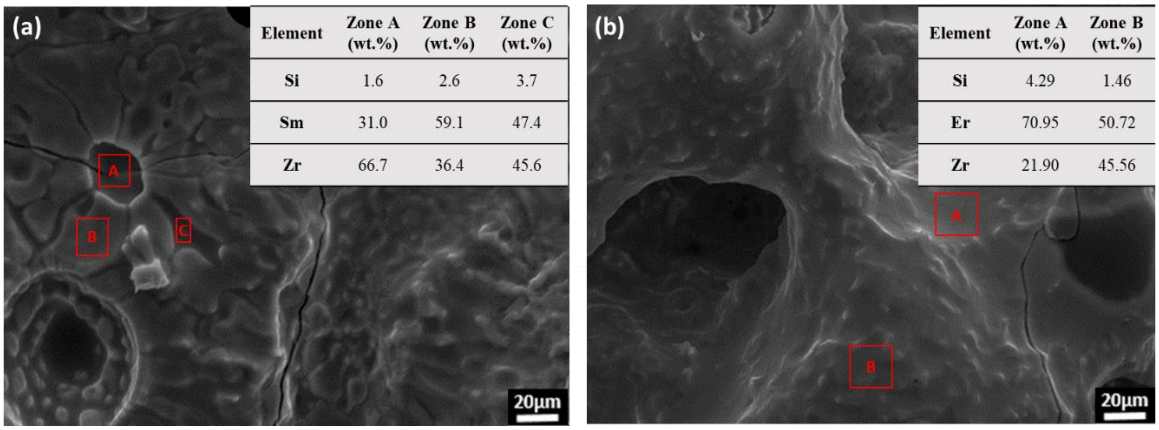

Figure 26: SEM-EDS for: a) micrograph of the flower-like microstructure on the 1Sm:0Er billet after the 60s ablation cycle, b) micrograph of the 0Sm:1Er billet after the 60s ablation cycle.

Because of the Sm^{3+} and Er^{3+} atoms being present in the rising B_2O_3-rich liquid containing dissolved ZrO_2, the final oxide scale product formed during the ablation testing will be different. This was confirmed by the XRD results on Figures 24a-b and the SEM-EDS of Figure 26a where the center region of the "flower-like" structure is composed of the crystalline c_1-$(Sm/Er)_{0.2}Zr_{0.8}O_{1.9}$ instead of the m-ZrO2 reported in the Karlsdottir et al.[17,18,21] studies or the Sm-stabilized t-ZrO_2 phase in Brenner et al.[16] study.

The evaporation of B_2O_3 glass would be expected as the maximum front surface temperatures were 1690 ± 20°C and 1717 ± 21°C during the 60s ablation tests for the 1Sm:0Er and 0Sm:1Er billets, respectively. Based on these surface temperatures it is also expected that much of the SiO_2 glass would be evaporated, consistent with the small amounts of Si detected in the EDS results presented in Figure 26a-b.

Even though the powder preparation and the ablation test parameters used in the present study were the same than the ones used in the Brenner et al.[16] study, the resulted final oxide scale was different. This difference occurred because the alumina substrates in the Brenner et al.[16] study became part of the system by forming a blister after the ablation for 60s due to a local eutectic reaction occurring between Sm_2O_3, ZrO_2, and Al_2O_3, and therefore, inhibited the formation of the c_1-$(Sm/Er)_{0.2}Zr_{0.8}O_{1.9}$ reported for the 1Sm:0Er sample in the present study. If the problem of the alumina substrate becoming part of the system in the Brenner et al.[16] study is avoided, the c_1-

$(Sm/Er)_{0.2}Zr_{0.8}O_{1.9}$ oxide phase will be formed, consistent with Tan et al.[4,9] studies and the present study.

The only difference in the XRD results between the samples ablated for 60s and 300s is the evidence of more glassy phase after longer ablation times, as observed by larger amorphous humps at lower values of 2θ for each of the Sm:Er billets investigated. The glassy phase seems to be more evident as Er concentration increased. The increase in the amount of the glassy phase makes sense with the assertions in previous studies,[9,18,22] where the addition of rare-earth dopants to ZrB2/SiC billets modifies the tetrahedron structure of B_2O_3 and SiO_2 resulting in the reduction of the viscosity of the glass and melting temperature. As the theoretical density of samarium oxide (7.62 g/cm3) is lower than erbium oxide (8.64 g/cm3), the viscosity should be reduced even more as the Sm concentration increases. This relationship between reduction of viscosity and increase of glassy phase is evident for the ablated billets after 300s of this study. The increased glassy phase formed as the ablation time is increased from 60s to 300s is preventing conduction of heat away from the surface resulting in an increase of the front surface temperature. Therefore, it is expected that this glassy phase might affect the emittance, but future studies need to be performed to confirm this assertion.

With increased time at high temperature, the glassy phase submerges the convection cells and they essentially disappear. Even though we cannot see the convection cells in the final microstructure after ablation, their effect on the final microstructure can be noted by the presence of c_1-$(Sm/Er)_{0.2}Zr_{0.8}O_{1.9}$ crystalline islands surrounded by a glassy phase. Occasionally remnants of the convection cells can be observed in the final microstructure. For example, a "flower-like" structure is noted in Figure 23a for the 1Sm:0Er sample. After ablation for 300s, the c_1-$(Sm/Er)_{0.2}Zr_{0.8}O_{1.9}$ islands grow, coalesce, and inhibit the formation of petals by forming the crystalline grains shown in Figures 23g, 23h, and 23i.21,23

Overall, the convection cell mechanism occurring in the present study is similar to both Karlsdottir et al.[17,18,21] and Brenner et al.[16] studies. However, significant differences are shown due to the rare-earth dopants used in the present study which cause the formation of different oxide scales during ablation testing. As the main purpose of doping the ZBS systems with emittance modifiers as Sm and Er is to form a c_1-$(Sm/Er)_{0.2}Zr_{0.8}O_{1.9}$ phase, the Sm-stabilized t-ZrO_2 in the Brenner et al.[16] study and the m-ZrO2 in the Karlsdottir et al.[17,18,21] studies do not offer any improvement in modifying the emittance and the Sm^{3+} ions role in the final microstructure is limited. The ability to increase the emissivity by forming the c_1-$(Sm/Er)_{0.2}Zr_{0.8}O_{1.9}$ instead of m-ZrO2 was confirmed by Tan et al.[9] study by increasing the emissivity up to 0.9 at 1600°C for a coating constituted of 5 mol.% Sm with a balance of ZrB2/SiC. Therefore, it can be concluded that a similar c_1-$(Sm/Er)_{0.2}Zr_{0.8}O_{1.9}$ with different Sm:Er ratios will produce differences in the emittance. As a result, the c_1-$(Sm/Er)_{0.2}Zr_{0.8}O_{1.9}$ is a more desirable oxide product because it produces a potential tailorable emittance oxide scale; whereas forming a more stable and ablation resistance oxide scale than both the m-ZrO2 formed on Karlsdottir et al.[17,18] studies, and the Sm-stabilized t-ZrO2 on Brenner et al.16 study. Furthermore, the c_1-$Sm_{0.2}Zr_{0.8}O_{1.9}$ has a melting point of 2700 °C for 3 mol.% of Sm dopant which is similar to the one of m-ZrO_2.[9]

Finally, the fact that the beneficial c_1-$(Sm/Er)_{0.2}Zr_{0.8}O_{1.9}$ provides a more dense oxide scale than m-ZrO_2 typically formed on ZBS systems, could help to address the one of the most damaging factors to ZBS systems caused by the porous m-ZrO_2 scale that does not provide any barrier to oxygen transport and tends to detach from the base alloy. Hence, the beneficial c_1-$(Sm/Er)_{0.2}Zr_{0.8}O_{1.9}$ oxide scale formed in the surface, will reduce the amount of oxygen transported to deeper parts of the billet where the concentration of m- ZrO_2 is higher as showed by the EDS line-scan on Figure 25. This statement was also reported by Tan et al.[9] who showed that the c_1-$(Sm/Er)_{0.2}Zr_{0.8}O_{1.9}$ oxide scale formed for ZBS coatings doped with 3 mol.% of Sm is more dense than m-ZrO_2 formed for ZBS coatings.

4.2 Second observation: *Changes in the surface Sm and Er dopant concentration affects surface temperature measured.*

Despite the similarities of the convection cell mechanism in the billets prepared with five different Sm:Er molar ratios, the heating rates vary as can be noted by the difference in the inflection points observed in Figures 20a-b. For example, Figure 4a shows that the inflection point temperature was the highest for the 0Sm:1Er sample at 1600 ± 19°C after ablation for 12s, and the lowest for the 2Sm:1Er sample 1300 ± 16°C after ablation for 9s. These differences in the inflection points can be explained by the different compositions of Sm3+ and Er3+ atoms in the billets which change the emittance and the spectral absorptance of the oxide scales formed during ablation.

Changes in the emittance caused by using Sm^{3+} dopant have been shown in previous studies which demonstrated that the emittance of ZrO_2 can be increased via doping with rare-earths oxides which intentionally introduce defects into a pure material.[9,24] By comparing the ionic conductivity of the c_1-$(Sm/Er)_{0.2}Zr_{0.8}O_{1.9}$ phase formed in the present study with the m-ZrO_2, it is important to note that the ionic conductivity will increase for the c_1-$(Sm/Er)_{0.2}Zr_{0.8}O_{1.9}$ as the incorporated Sm^{3+} and Er^{3+} ions creates oxygen vacancies.[9,23] These oxygen vacancies provide transitions within the material band gap which modify the emittance.[9,23] Figure 8 shows that the amount of m-ZrO_2 increases as the distance from the ablated surface is further increased. Based on that, the ionic conductivity should be higher in the ablated surface than in deeper regions of the billets.

Samarium oxide has demonstrated high emittance from visible to near IR wavelengths.[12] It is expected that the emittance will generally increase as the Sm3+ concentration is raised. Hence, increases in the heating rate may result from changes in emittance upon heating of such rare earth doped coatings. Previous evaluation of Sm-doped ZrB_2/SiC coatings[9] demonstrate that the Sm^{3+} atoms concentration is much higher at the ablated surface in comparison with Sm^{3+} atoms concentration in the bulk. Figure 25 shows the rare-earth dopant concentration is much higher in the ablated surface than in the bulk. Therefore, it is expected that the concentration dependent emittance in the 2Sm:1Er billet will be higher than in the 1Sm:2Er sample. Thus, ultimate temperature observed is lower for Sm rich coatings and considerable inflection points in temperature are observed for Sm rich coatings in Figure 21b.

On the other hand, it is well known that erbium oxide has demonstrated a low emittance in several wavelength ranges.[12] As the emittance for the current work was set to 0.9 on the pyrometer, the temperature would be underestimated if the emittance of the oxidized surface is lower at 1.55μm. Therefore, if the surface is reradiating less efficiently for a given temperature or becoming more absorptive at torch wavelengths, such coatings would heat more rapidly and/or achieve a higher ultimate temperature. After ablation for 60s, it is shown that as the Er^{3+} concentration is increased and the resulting c_1-$(Sm/Er)_{0.2}Zr_{0.8}O_{1.9}$ oxide scale is more either absorptive at torch wavelengths and/or reradiating less efficiently, and therefore, achieving a higher surface temperature for Er rich billets. Also, in Figure 4a, the maximum temperatures during the ablation cycle were the highest for the 0Sm:1Er and 1Sm:2Er samples; and the lowest for the 2Sm:1Er sample. However, this relation cannot be fully established as the ablation time is further increased from 60s to 300s. Figure 21b shows that maximum temperatures during the ablation cycle was the highest for the 1Sm:2Er sample, and lower for the 1Sm:0Er, 2Sm:1Er, 1Sm:1Er, and 0Sm:1Er samples. As can be noted by the results after ablation for 300s, the maximum temperatures of the 1Sm:0Er, 2Sm:1Er, 1Sm:1Er, and 0Sm:1Er samples were very similar, and therefore, the benefit of being able to control the emittance and absorption properties by varying the Sm^{3+} and Er^{3+} concentration is not clear. As the only difference in the XRD results after ablation for 60s and 300s in figures 24a-b is the evidence of more glassy phase after longer ablation times, as observed by larger amorphous humps at lower values of 2θ, it is evident that the increase in glassy phase is inhibiting the beneficial effects of increasing the emittance as the Sm^{3+} concentration is increased from 0-2.94 mol%. A possible solution to avoid this problem and maximize the beneficial effects of tailoring the emittance at these higher temperatures shown by figure 4b is to increase the total dopant(s) concentration incorporated into the sample from 3 mol.% to 5 mol.% as in Tan et al.[9] study.

5. Conclusions

Sintered ZrB_2/SiC billets co-doped with Sm and Er atoms in five different ratios were prepared. These samples were evaluated via ablation testing for 60s and 300s using an oxyacetylene torch. The phase assemblage and microstructure of the surface were evaluated after each ablation time. ZBS billets co-doped with Sm and Er forms a potential tailorable emittance c_1-$(Sm/Er)_{0.2}Zr_{0.8}O_{1.9}$ oxide scale as the major phase, which provides a more stable oxide scale than the m-ZrO_2 oxide scale formed in ZBS systems. The crystalline oxide scale and amorphous phases form by a convection cells mechanism where the c_1-$(Sm/Er)_{0.2}Zr_{0.8}O_{1.9}$ crystalline islands precipitate, grow and coalesce. Changes in the surface Sm and Er dopant concentration affects surface temperature measured due to changes in spectral emittance upon heating.

References

1. Squire T, Marschall J. Material property requirements for analysis and design of UHTC components in hypersonic applications. Journal of the European Ceramic Society. 2010;30(11):2239-2251.

2. Mack A. Aerothermodynamic behaviour of a generic nosecap model including thermomechanical structural effects. Aerospace Science and Technology. 2007;11(5):386-395.

3. Tan W, Adducci M, Trice R. Evaluation of Rare-Earth Modified ZrB2-SiC Ablation Resistance Using an Oxyacetylene Torch. Journal of the American Ceramic Society. 2014;97(8):2639-2645.

4. Tan W, Petorak C, Trice R. Rare-earth modified zirconium diboride high emissivity coatings for hypersonic applications. Journal of the European Ceramic Society. 2014;34(1):1-11.

5. Monteverde F. The thermal stability in air of hot-pressed diboride matrix composites for uses at ultra-high temperatures. Corrosion Science. 2005;47(8):2020-2033.

6. Monteverde F, Savino R. Stability of ultra-high-temperature ZrB2–SiC ceramics under simulated atmospheric re-entry conditions. Journal of the European Ceramic Society. 2007;27(16):4797-4805.343

7. Tului M, Marino G, Valente T. Plasma spray deposition of ultra high temperature ceramics. Surface and Coatings Technology. 2006;201(5):2103-2108.

8. Li H, Zhang L, Cheng L, Wang Y. Ablation Resistance of Different Coating Structures for C/ZrB2-SiC Composites Under Oxyacetylene Torch Flame. International Journal of Applied Ceramic Technology. 2009;6(2):145-150.

9. Tan W, Adducci M, Petorak C, Thompson B, Brenner A, Trice R. Effect of rare-earth dopant (Sm) concentration on total hemispherical emissivity and ablation resistance of ZrB 2 /SiC coatings. Journal of the European Ceramic Society. 2016;36(16):3833-3841.

10. Ilic O, Bermel P, Chen G, Joannopoulos J, Celanovic I, Soljačić M. Tailoring high-temperature radiation and the resurrection of the incandescent source. Nature Nanotechnology. 2016;11(4):320-324.

11. Lin S, Moreno J, Fleming J. Three-dimensional photonic-crystal emitter for thermal photovoltaic power generation. Applied Physics Letters. 2003;83(2):380-382.

12. Lenert A, Bierman D, Nam Y, Chan W, Celanović I, Soljačić M et al. A nanophotonic solar thermophotovoltaic device. Nature Nanotechnology. 2014;9(2):126-130.

13. Guazzoni G. High-Temperature Spectral Emittance of Oxides of Erbium, Samarium, Neodymium and Ytterbium. Applied Spectroscopy. 1972;26(1):60-65.

14. Bartuli C, Valente T, Tului M. Plasma spray deposition and high temperature characterization of ZrB2–SiC protective coatings. Surface and Coatings Technology. 2002;155(2-3):260-273.

15. Girin AG. Laws governing the fragmentation of a droplet in a high-speed stream. Journal of Engineering Physics and Thermophysics. 2011;84(5):1009–15.

16. Brenner AE, Peña AA, Phuah XL, Petorak C, Thompson B, Trice RW. Cyclic ablation of high-emissivity Sm-doped ZrB 2 /SiC coatings on alumina substrates. Journal of the European Ceramic Society. 2018;38(4):1136–42

17. Karlsdottir SN, Halloran JW, Henderson CE. Convection Patterns in Liquid Oxide Films on ZrB2-SiC Composites Oxidized at a High Temperature. Journal of the American Ceramic Society. 2007;90(9):2863–7.

18. Karlsdottir SN, Halloran JW. Formation of Oxide Films on ZrB2-15 vol% SiC Composites During Oxidation: Evolution with Time and Temperature. Journal of the American Ceramic Society. 2009;92(6):1328–32.

19. Hu P, Gui K, Yang Y, Dong S, Zhang X. Effect of SiC Content on the Ablation and Oxidation Behavior of ZrB2-Based Ultra High Temperature Ceramic Composites. Materials. 2013;6(5):1730–44.

20. Padovano E, Badini C, Celasco E, Biamino S, Pavese M, Fino P. Oxidation behavior of ZrB2/SiC laminates: Effect of composition on microstructure and mechanical strength. Journal of the European Ceramic Society. 2015;35(6):1699–714.

21. Karlsdottir SN, Halloran JW. Formation of Oxide Films on ZrB2-15 vol% SiC Composites During Oxidation: Evolution with Time and Temperature. Journal of the American Ceramic Society. 2009;92(6):1328–32.

22. Opila E, Levine S, Lorincz J. Oxidation of ZrB2- and HfB2-based ultra-high temperature ceramics: Effect of Ta additions. Journal of Materials Science. 2004;39(19):5969–77.

23. Ouyang, G., Ray, P., Kramer, M., & Akinc, M. (2016). Effect of AlN Substitutions on the Oxidation Behavior of ZrB2-SiC Composites at 1600°C. American Ceramic Society. Journal of the American Ceramic Society, 99(10), 3389-3397.

24. Avdoshenko, S. M. & Strachan, A. High-temperature emissivity of silica , zirconia and samaria from ab initio simulations : role of defects and disorder. 2014.

Accomplishment 4: Data Conversion: Spectral Radiance to Emittance

1. Emittance Testing and Data Conversion Process

Planck's law represents the spectral distribution of blackbody emission (L_λ) at temperature T_b as a function of wavelength (λ), first radiation constant (c_1=1.1910439 x 10^{-16} W.m^2), and second radiation constant (c_2=0.014388 m.K).

$$L_\lambda = \frac{c1}{\lambda^5\left[\exp\left(\frac{c2}{\lambda * Tb}\right)-1\right]} \qquad (1)$$

There are three main aspects from the plank distribution equation that should be noted. First, the emitted spectral radiance increases with increasing temperature. Second, at any wavelength the value of the emitted spectral radiance increases with increasing temperature. Finally, as defined by the Wien's displacement law, the spectral zone in which the spectral radiance is concentrated will be located at shorter wavelengths as the temperature increases.

Emittance testing was performed at the RHINO lab at the Airforce Research Laboratory (AFRL) in Dayton, Ohio. The samples were placed in a graphite holder where both the front face and back face of the sample were exposed. The back face of the sample was then heated with a laser powered at either 700W, 800W, and 900W and held for 60s. Total time recorded was 80s for each sample and spectral radiance data was collected with intervals of 1s across the wavelength range. The sensor collected spectral radiance measurements from 1500-5000 nm with intervals of 14.2 nm (246 wavelength points). To perform surface temperature and emittance calculations, a MATLAB algorithm was developed to average and calibrate a set of blackbody data. This algorithm relates the measured spectral radiance signal from the testing equipment with the blackbody sample temperature, perform a blackbody calibration, and subsequently, calculate the real temperature and emittance data. The calibration function was defined using the Planckian form of the Sakuma-Hatorri equation, which is a non-linear regression method [1,2]. The advantages of this equation are that approximates Planck's law integrated over a spectral band and can be easily inverted to solve for both temperature and emittance. The Planckian form of the Sakuma-Hatorri equation for a blackbody temperature is provided by the equation (2) as function of the wavelength over defined temperature ranges, the second radiation constant (c_2); and the constants A, B and C.

$$T = \frac{c2}{A * \ln\left(\frac{C}{L\lambda}\right)} - \frac{B}{A} \qquad (2)$$

Every wavelength has a unique *A*, *B*, *C*, L_λ, and ε, but the real temperature is the same across all wavelengths. As a result, for each spectral radiance vs wavelength profile, four unknowns need to be calculated (B, C, T, and ε). The coefficients in the equation (2) were obtained by using the following assumptions: (1) the coefficient A is constrained to be the wavelength (λ), and (2) the coefficients B and C are not temperature dependent. The coefficients B and C are an offset and a gain respectively, which were obtained from the calibration data, and have been determined according to what calibration is required for the blackbody data to agree with the theoretical Planckian curves. It must be noted that each calculation requires at least two temperatures to solve for the B and C coefficient values.

Four blackbody temperatures across the range of interest were calculated to solve for the unknown Sakuma-Hatorri coefficients (B and C) and calibrate the data. To solve for these four unknown blackbody temperatures, a set of four Sakuma-Hatorri equations was used with a constant wavelength λ_n at the four different unknown blackbody temperatures. In other words, for n=1, 2, 3, …, 254, a set of the Sakuma-Hatorri equations: $L_\lambda(\lambda_n, T_{b1})$, $L_\lambda(\lambda_n, T_{b2})$, $L_\lambda(\lambda_n, T_{b3})$ and $L_\lambda(\lambda_n, T_{b4})$; were used to solve the four unknown blackbody temperatures at each wavelength. As the blackbody temperature must be the same across the 1500-5000 nm wavelength range, the four average blackbody temperatures calculated were 1207 °C, 1368 °C, 1501 °C, and 1657 °C.

After calculating the four blackbody temperatures that represent the temperature range of interest, it is followed by a curve fitting process using the Sakuma-Hatorri relationship to calibrate and approximate the actual spectral radiance signal measured. It is shown by the figure 27, where the four spectral radiance versus wavelength distributions at the calculated blackbody temperatures were calibrated by the Sakuma-Hatorri function described by equation (2).

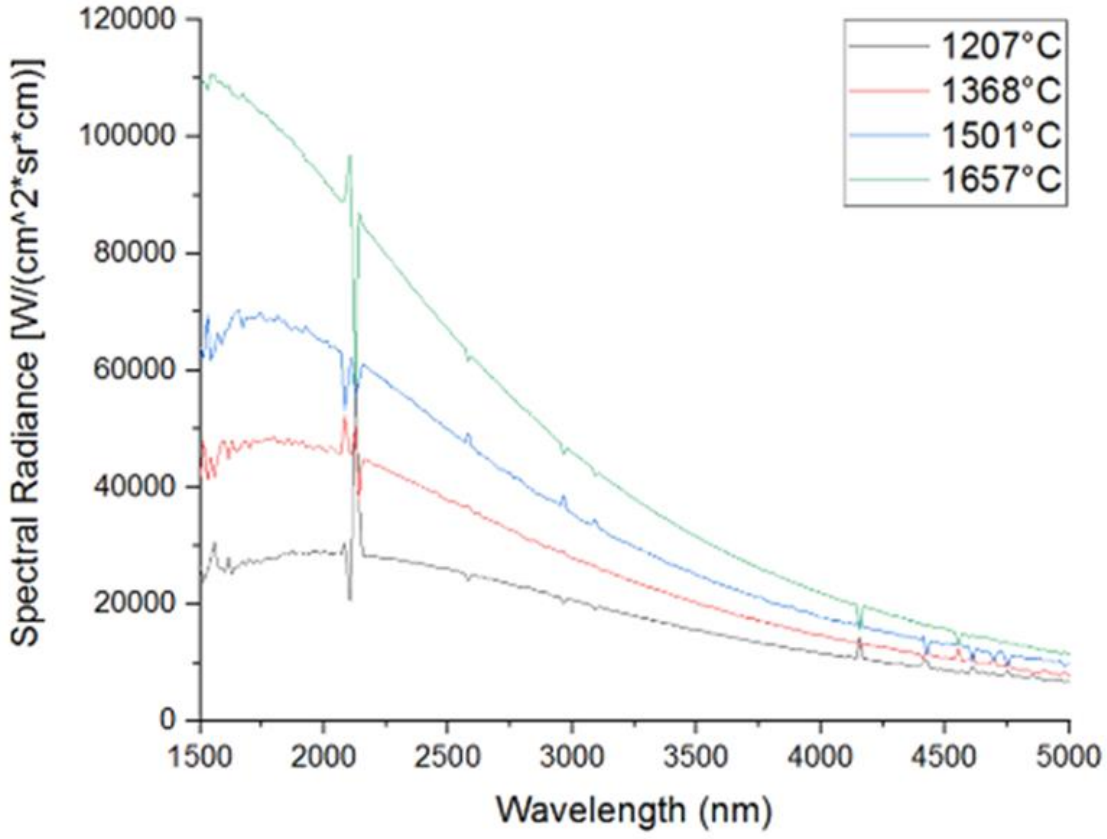

Figure 27: Blackbody calibration at the four chosen temperatures of interest.

Figure 28 shows that the value of coefficient B keeps mainly constant across the wavelength range from 1500-5000 nm. On the other hand, figure 28 shows that the coefficient C value decrease as the wavelength increase.

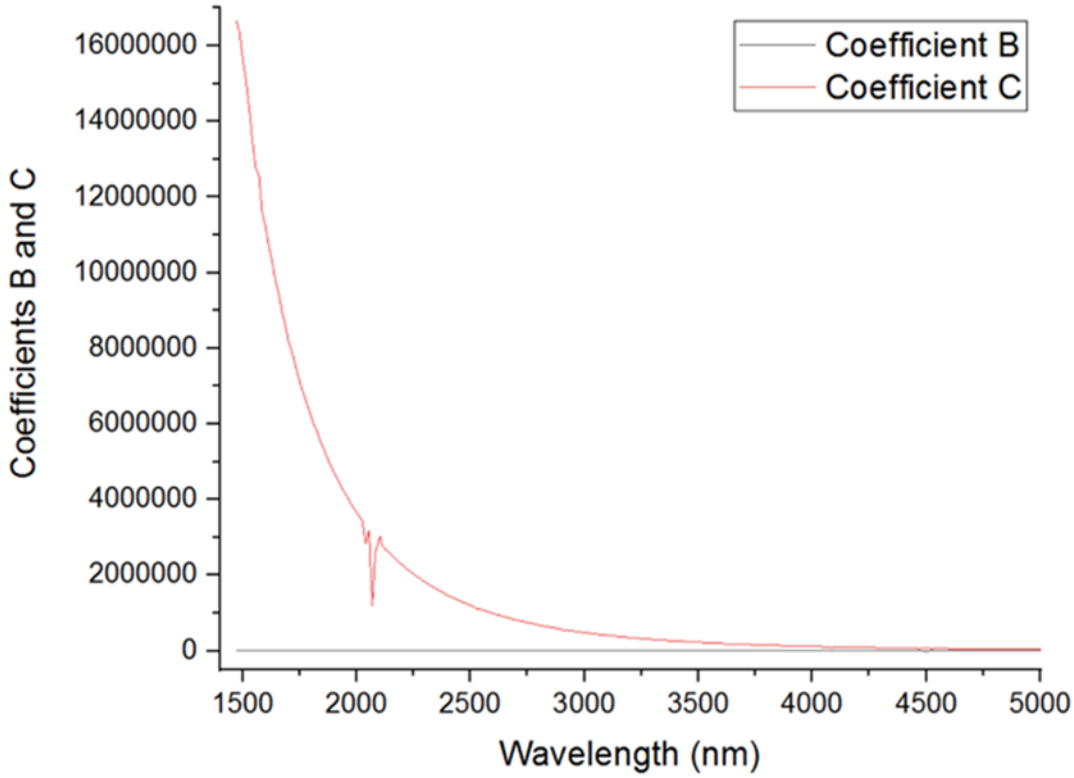

Figure 28: Coefficients B and C versus wavelength from 1500-5000 nm.

After calculating the three coefficients (A, B and C), the real temperature profiles were obtained by multiplying the equation (2) by the emittance term (ε) powered to the -0.25 as shown in equation (3).

$$T = [\boldsymbol{\varepsilon}^{-1/4}] * [\frac{c2}{A * \ln\left(\frac{C}{L\lambda}\right)} - \frac{B}{A}] \qquad (3)$$

To calculate the real temperatures, an initial emittance value was assumed across a narrow wavelength range were the data is smooth. As the data is smooth in that range, it can be assumed that it behaves as a graybody, and therefore, the emittance is constant allowing to calculate the real temperatures. After calculating the real temperatures, the equation (3) is solved for the emittance values across the wavelength range from 1500-5000 nm. Figures 29 shows an example of the temperature versus time comparison for the five different Sm:Er ratios tested at 800Watts for 80s. For the temperature versus time graph shown in Figure 29, an initial emittance assumption of 0.6 was used over the 3500-3900 nm range.

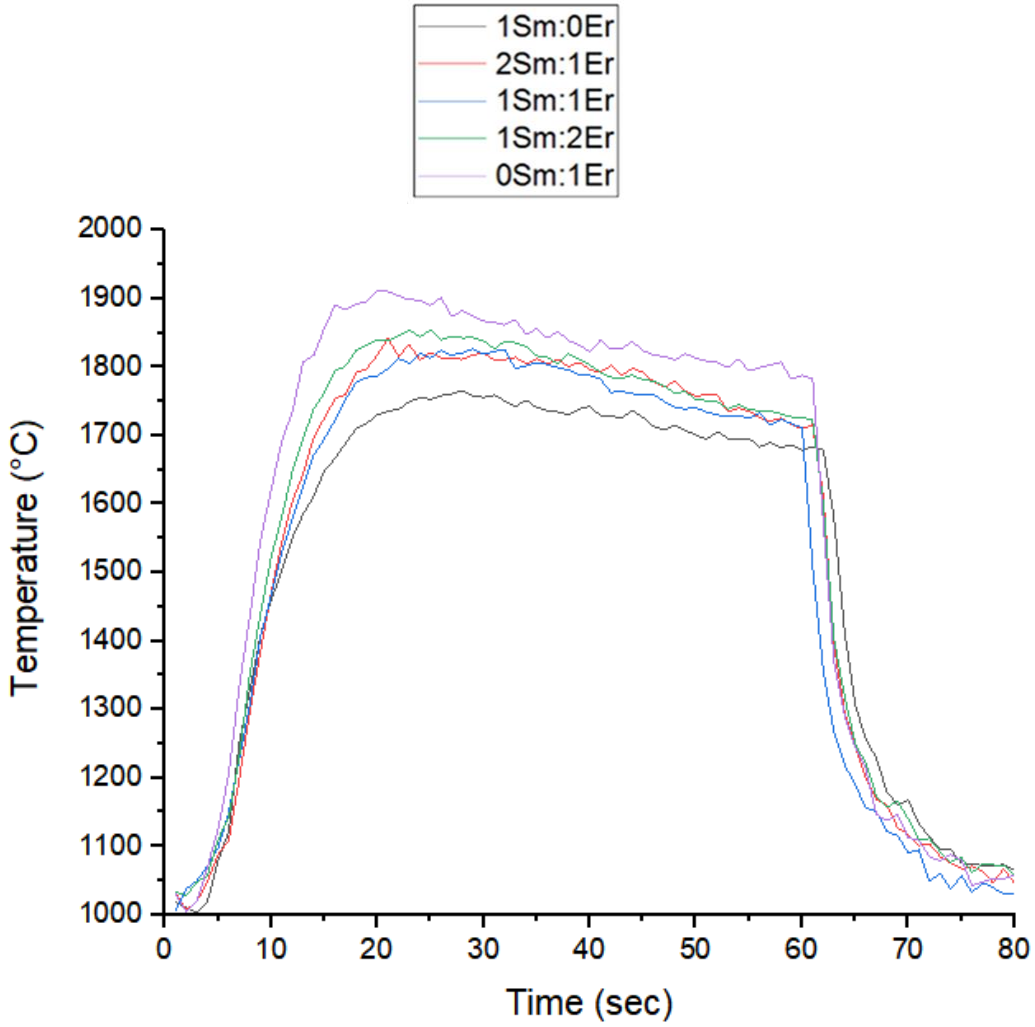

Figure 29: Temperature versus time comparison for the five different Sm:Er ratios tested at 800 Watts for 80s.

References

1. Saunders, P. Propagation of uncertainty for non-linear calibration equations with an application in radiation thermometry. (2003).
2. Saunders, P. & White, D. R. Physical basis of interpolation equations for radiation thermometry. (2003).

Accomplishment 5: Evaluation of Rare-Earth Element Dopants (Sm and Er) on Emittance of ZrB_2/SiC Sintered Billets

1. Experimental Procedure

1.1 Materials and powder preparation

Spray-dried powders were prepared using the same method employed by Tan et al.[4,9] and the Brenner et al.[20] studies. Briefly, a lab spray dryer (APV Anhydro Model S1, Anhydro Inc, Soeborg, Denmark) was used to produce powder agglomerate from a liquid suspension feed (Aero-Instant Spraying Service, Brunswick, USA) that consisted of 80 vol.% ZrB2 (3–5 μm, Grade A, HC Starck, Munich, Germany), 20 vol.% α-SiC (1.4 m, Grade UF-05, HC Starck, Munich, Germany), 0.4 wt.% dispersant (Darvan 821A, R.T. Vanderbilt Company, Inc., Norwalk, USA), 2 wt.% PVA binder (Celvol 203, Celanese Corporation, Dallas, USA) and deionized water. The suspension was fed into the drying chamber by using a spraying nozzle, where the air was heated to 200 °C. Next, a rotary atomizer spun at ~30,000 rpm was used to atomize the suspension into controlled-size droplets. The temperature at the outlet was ~105 °C. The average particle size of the spray-dried particles, which was obtained by using a Malvern Mastersizer 2000 (Malvern Instrument Ltd., Worcestershire, UK), was approximately 38 μm. Figure 1 shows a SEM micrograph of the undoped spray dried ZrB2-20 vol% SiC particles.

Samarium and/or erbium dopants were added to the spray dried ZrB2/SiC powders via a chemical infiltration method. In this process, samarium nitrate hexahydrate (99.9% pure $Sm(NO_3)_3 \cdot 6H_2O$, MSE Supplies, Arizona, USA) and/or erbium nitrate hexahydrate (99.9% pure $Er(NO_3)_3 \cdot 6H_2O$, MSE Supplies, Arizona, USA) were dissolved into 99.9% pure isopropyl alcohol, and the resulting solution was then infiltrated into the porous spray-dried ZrB_2/SiC powder. Solutions mixed in five different molar ratios (1Sm:0Er, 2Sm:1Er, 1Sm:1Er, 1Sm:2Er and 0Sm:1Er) were prepared; the total rare-earth nitrate hexahydrate compound was added at an initial concentration of 10 mol.%. Next, the alcohol and likely some of the water was removed via a rotary evaporator (BM 200, Yamato Scientific America Inc., Santa Clara, USA) at 100°C. This powder was heated at 500°C in air for an hour to remove residual moisture, water, and nitrates. Tan et al.[4] performed a study of the normalized weight gain as a function of temperature from 200-1300°C demonstrating that below 600 °C both the ZBS and the Sm-doped coatings exhibit no weight gain that would be associated with oxidation. As the normalized weight gain was ~0 below 600 °C, it suggests that the oxygen content does not increase during the heat treatment at 500 °C. These results are consistent with temperature transitions reported by Bartuli et al.[14] for ZrB_2/SiC coatings, providing further evidence that the ZBS and the Sm-doped coatings did not have any weight gain below 600 °C. The first weight gain inflections start near 600°C due to the oxidation of ZrB_2 to form m-ZrO_2 and B_2O_3 glass.[4] After nitrate, water and moisture removal at 500°C, the dried mixture was sieved using a 60-mesh (250 μm aperture) to eliminate large agglomerates. For ZBS powders/dopant ratios, ~20% by weight was lost during the 500oC heat treatment. These losses are due to the evaporation of the nitrates and water. ZBS powders with different ratios of Sm and/or Er dopants were die pressed at 82 MPa. The pressed billets were heated to 1650 ^oC, held for 1 hr, heated to 2000 °C, held for 15 min, then cooled to room temperature. Sintering

occurred in an argon atmosphere with graphite heating elements at a partial oxygen pressure of 10-7 ppm. Samples were cut into 25.4 mm x 25.4 mm squares.

The billets were polished to ~0.1 μm using an auto polisher, where the billets were polished first to 6 μm, then to 3 μm, and finally to 0.1 μm. The bulk density of each billet for each ratio of Sm:Er was measured by the Archimedes methodology as described in the ASTM C373-88 standard. Surface roughness (Ra) was measured using an AFM (AS0200 AlphaStep, Tencor Corporation, Milpitas, USA). To help simplify discussion, the naming convention is on the intended molar ratios. For instance, the 2Sm:1Er billet was to contain 6.66 mol.% $Sm(NO_3)_3 \cdot 6H_2O$ and 3.33 mol.% $Er(NO_3)_3 \cdot 6H_2O$ in the ZrB_2/SiC matrix. The amount of Sm and Er incorporated into the samples was measured by ICPMS with fusion preparation on pulverized billets (NSL Analytical Services Inc., Cleveland, USA).

2. Results

2.1 Pre-ablated Sintered Samples Results

The actual concentrations of Sm (mol.%) and Er (mol.%) incorporated into each billet are listed in Table 3, along with the measured bulk density, theoretical density, total porosity (%), and surface roughness. It was observed that ~3 mol.% rare-earth element(s) were incorporated into the sintered billets, ~1/3 of the 10 mol.% rare-earth nitrate hexahydrate compounds during the chemical doping process. It should be noted that most of this reduction in the dopant concentration was caused by the heat treatment at 500°C where the water and nitrates were removed, and not because the Sm and Er were lost. Recall that the 10 mol.% added during the chemical doping process is referring to the combined $Sm(NO_3)_3 \cdot 6H_2O$ and $Er(NO_3)_3 \cdot 6H_2O$. Therefore, the combined concentrations of Sm (mol.%) and Er (mol.%) represents ~35% (~3.5 mol.%) of 10 mol.% added during the chemical doping process. As ~3 mol.% dopant(s) were incorporated into the sintered billets, it can be concluded that the reminder ~0.5 mol.% was lost during powder handling or during sintering. These results are different than the ones presented in Tan et al.[4,9] studies and Brenner et al.[16] study where 5 mol.% Sm dopant was incorporated into plasma-sprayed coatings. The decrease of the ~2 mol.% of the dopant(s) incorporated into the sintered billets of the present study were caused by the different method used to prepare the samples, as the samples used in Tan et al.[4,9] studies and Brenner et al.[16] study were prepared using a plasma spray process.

	$Sm(NO_3)_3 \cdot 6H_2O$ Added (mol%)	$Er(NO_3)_3 \cdot 6H_2O$ Added (mol%)	Actual Sm Incorporated (mol%)	Actual Er Incorporated (mol%)	Densification level (%)	Bulk Density (g/cm^3)	Volume of Open Porosity (cm^3)	Surface Roughness, Ra (nm)
1Sm:0Er	10	0	2.94	0		3.91	0.76	102 ± 12
2Sm:1Er	6.6	3.3	1.85	1.23		4.74	0.72	95 ± 15
1Sm:1Er	5	5	0.97	1.80		4.77	0.03	105 ± 14
1Sm:2Er	3.3	6.7	0.95	2.33		4.82	0.72	108 ± 8
0Sm:1Er	0	10	0	3.11		4.97	1.23	104 ± 11

Table 3: Samarium and erbium dopant concentration and properties after sintering.

Table 3 shows more Er dopant was integrated into the sample than the Sm dopant. This is apparent by comparing the 1Sm:0Er and 0Sm:1Er billets, where 2.94 mol.% of Sm and 3.11 mol.% or Er were incorporated respectively. This difference is explained by the differences in their molar mass, where Sm represents the 33.8% of the 10 mol.% $Sm(NO_3)_3 \cdot 6H_2O$ added during the chemical doping process for the 1Sm:0Er billet, whereas Er represents 36.3% of the 10 mol.% $Er(NO_3)_3 \cdot 6H_2O$ added for the 0Sm:1Er billet. Surface roughness (Ra~100 nm) were all similar, consistent with using the same polishing procedures for each billet investigated. Samples ranged in total porosity from 17 to 31%.

2.2 Microstructural and Phase Analysis Results after Laser Heating

Figures 30a-o compare the back-face surfaces after the 80s of laser heating. The back-face surface represents the side where the samples were heated by the laser. Each of the Sm:Er billets developed an adherent oxide scale on the laser side. The oxide scale color changes relative to the amount of Sm and Er dopant from yellow in the 1Sm:0Er sample to pink in the 0Sm:1Er sample. It can be seen from figure 30a-o that the amount of glassy phase increase as the laser power is increased due to the higher temperature achieved. Also, Figure 30a-o shows that cracks were formed in all the samples due to the thermal shock caused by the rapid laser heating.

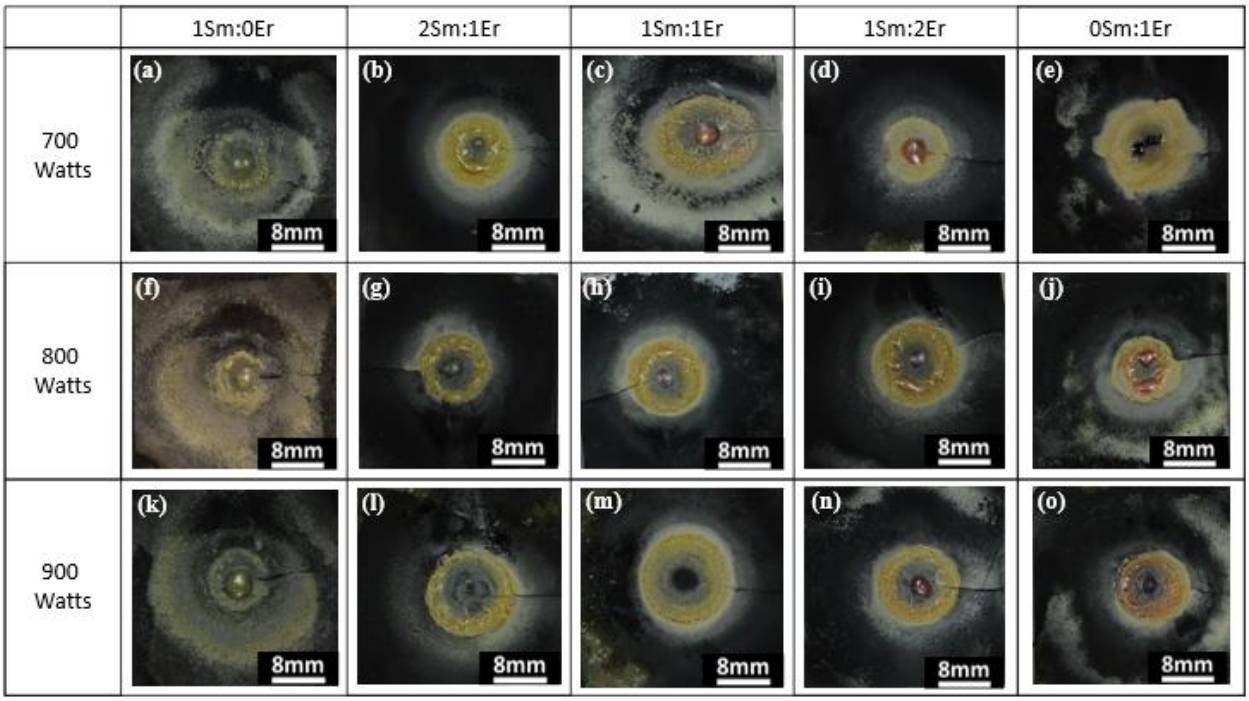

Figure 30: Optical images of the back-side of the billets (laser side).

Figures 31a-o compare the front-face surfaces after the 80s of laser heating. The front-face surface represents the side where the spectral radiance data were collected by the spectrometer. Each of the Sm:Er billets developed an adherent oxide scale on the laser side. As can be noted on Figure 31a-o, the glassy phase amount is much lower than in figure 30a-o due to the lower surface temperatures reached.

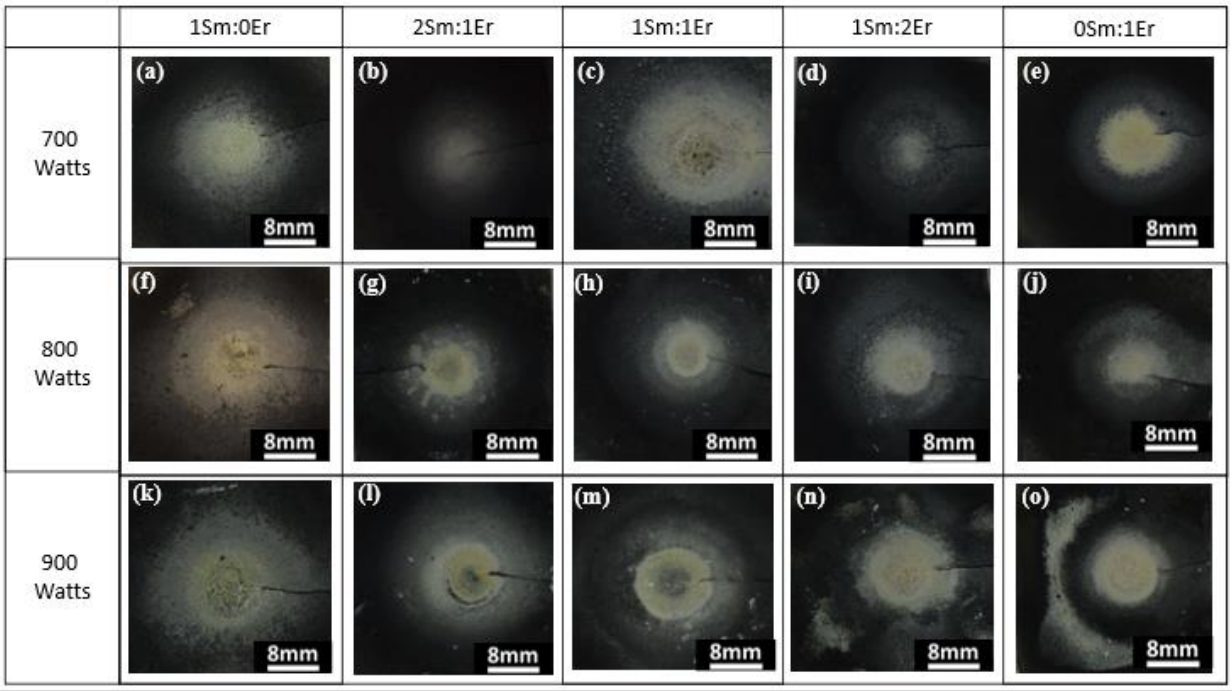

Figure 31: Optical Images of the Front Side of the Billets (Spectrometer Side where the data was collected).

The XRD results after the laser heating test for the 1Sm:0Er samples presented in Figure 32 shows that the major phase formed was monoclinic zirconia (*m*-ZrO_2, JCPDS-00-37-1484) with small portions of the cubic samarium zirconium oxide scale (c_1-$Sm_{0.2}Zr_{0.8}O_{1.9}$, JCPDS-01-78-1302), Sm_2O_3 and ZrB_2. For the 2Sm:1Er, 1Sm:1Er, and 1Sm:2Er billets samples, the XRD results also shows a similar *m*-ZrO_2 as the major phase with small amounts of a similar cubic structure (c_1-$(Sm/Er)_{0.2}Zr_{0.8}O_{1.9}$), SiO_2, $(Sm/Er)_2O_3$ and ZrB_2. The c_1-$(Sm/Er)_{0.2}Zr_{0.8}O_{1.9}$ is formed due to the Sm and Er atoms exchanging positions because of their similar ionic size (242 *p*m for Sm and 236 *p*m for Er). The primary peaks were shifted to larger 2θ due to the smaller interplanar spacing caused by the slightly smaller erbium atoms. Small portions of monoclinic zirconia (*m*-ZrO_2, JCPDS-00-37-1484) were also observed. On the contrary, the 0Sm:1Er sample was primarily cubic erbium zirconium oxide scale (c_1-$Er_{0.2}Zr_{0.8}O_{1.9}$) with small amounts of *m*-ZrO_2, SiO_2, Er_2O_3 and ZrB_2.

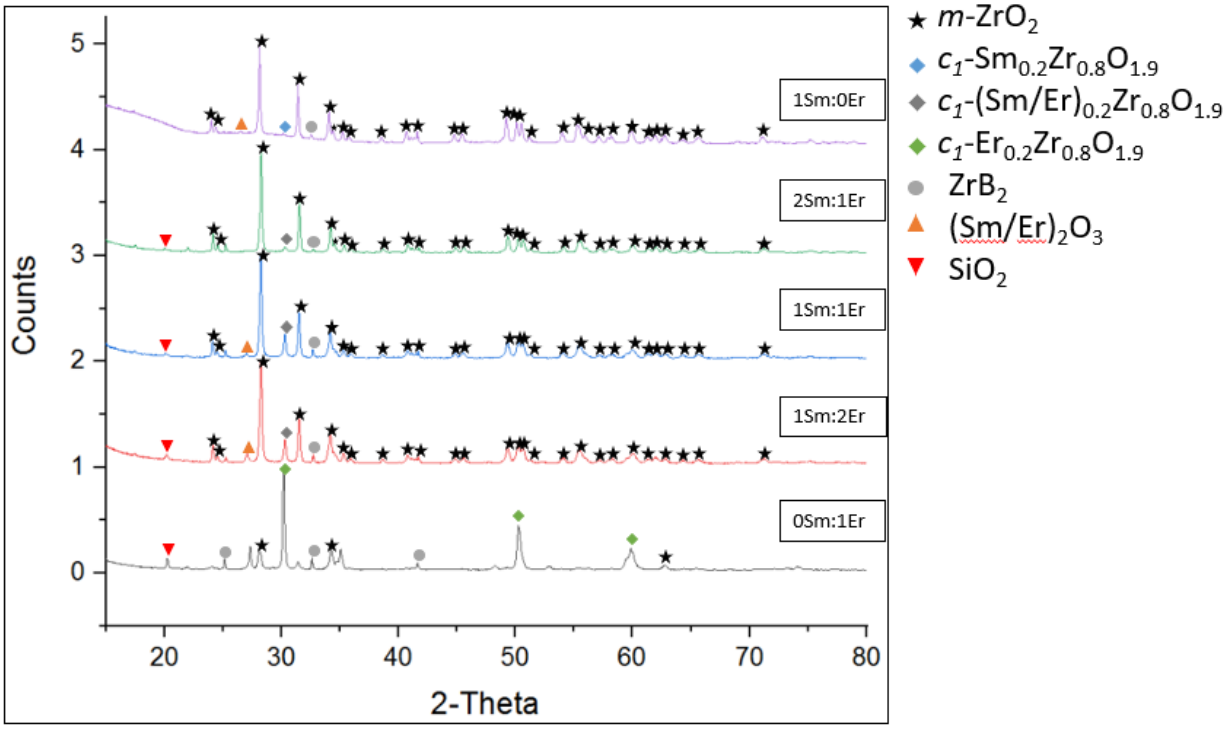

Figure 32: XRD patterns of the surface on the spectrometer side.

Figures 33a-o compare SEM micrographs of the surface of the billets after laser heating for 80s. For all the Sm:Er samples exposed to a laser heating power of 700 Watts in Figure 33a-e, the surface appears to have clusters of crystalline islands surrounded by an amorphous phase. Figures 33k-o shows that as the power is further increased to 900 Watts, the amount of glassy phase decrease whereas the porosity increase.

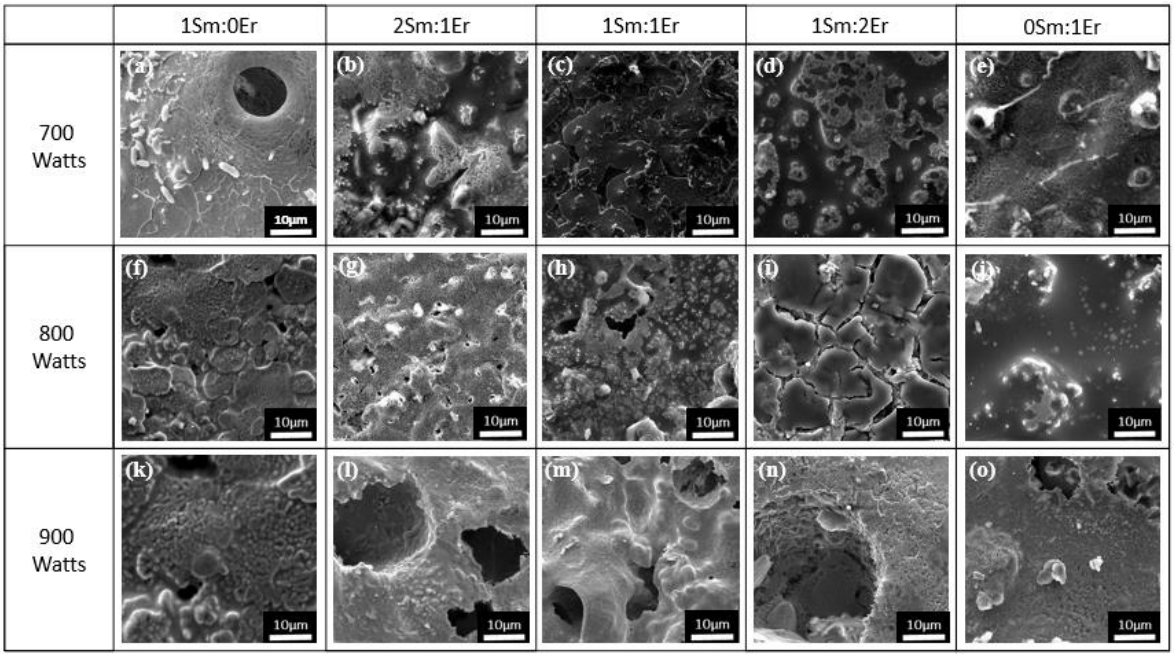

Figure 33: SEM micrographs of the billets after the laser heating test.

2.3 Emittance Results after Laser Heating

The plots of front surface temperature as a function of time (not shown) during the 80s emittance testing were calculated for each of the five billets tested at three different laser powers (700 Watts, 800 Watts and 900 Watts). All of them displayed a continuous temperature increase through the 80s of laser heating, with a rapid increase in temperature for the first ~15s until a maximum value is reached, followed by a very slow decrease in temperature for the next ~45s, and finally a rapid decrease in temperature for the final ~20s after the applied power is turned off. To accurately evaluate the effect of the rare-earth element dopants (Sm and Er) on the emittance of ZBS sintered billets, two different methods were used to analyze the emittance data. The first method analyses each Sm:Er ratio separately at three different temperatures: 1850 ^{o}C, 2000 ^{o}C and 1800 ^{o}C. The first temperature (1850 ^{o}C) was measured from the first 15s of heating when the temperature is rapidly increasing. The second temperature (2000 ^{o}C) was measured after the maximum temperature was achieved during the next ~45s of heating. The third temperature (1800 ^{o}C) was measured when the temperature is rapidly decreasing after the applied power is turned off. The second method analyses all the different five Sm:Er molar ratios at a constant temperature. The constant temperature used were 1850 ^{o}C and 2000 ^{o}C.

Figures 34a-b show the emittance versus wavelength profiles from 1500-3000 nm at 1850°C, 2000°C and 1800 °C for the 1Sm:0Er, and 0Sm:1Er samples. For the 1Sm:0Er sample, the emittance profile at 2000 °C is not presented because the 1Sm:0Er sample was the only one that did not reach that temperature. The emittance profiles for the 1Sm:0Er at 1850 °C and 1800 °C is basically the same. For the 0Sm:1Er sample, it is shown that the emittance slightly decreases with temperature from 1500-2550 nm but as the wavelength is further increased, the emittance remains mainly constant.

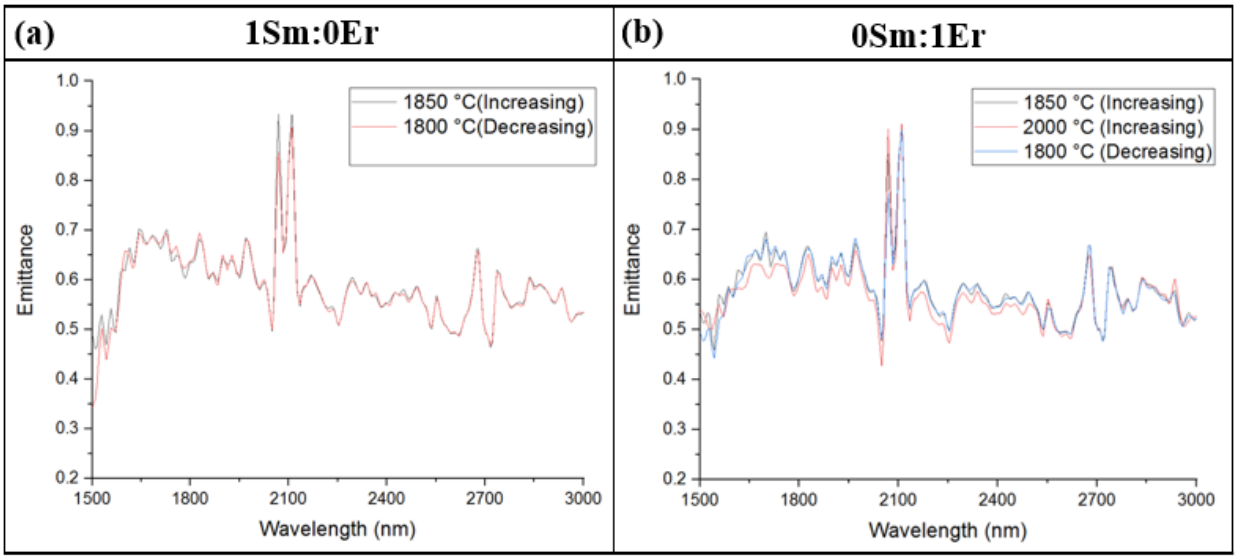

Figure 34: Emittance versus wavelength profiles at 1850°C, 2000°C and 1800 °C from 1500-3000 nm for: (a) 1Sm:0Er, and (b) 0Sm:1Er.

Figures 35a-b show the emittance versus wavelength profiles from 3000-4500 nm at 1850°C, 2000°C and 1800 °C for the 1Sm:0Er, and 0Sm:1Er samples. For the 1Sm:0Er sample,

the emittance profile at 2000 °C is not presented because the 1Sm:0Er sample was the only one that did not reach that temperature. The emittance profiles for the 1Sm:0Er and 0Sm:1Er samples at 1850 °C and 1800 °C is basically the same. The only significant change on both the 1Sm:0Er and the 0Sm:1Er samples is that the emittance increase by increasing the temperature at the maximum emittance peak located at ~4355 nm.

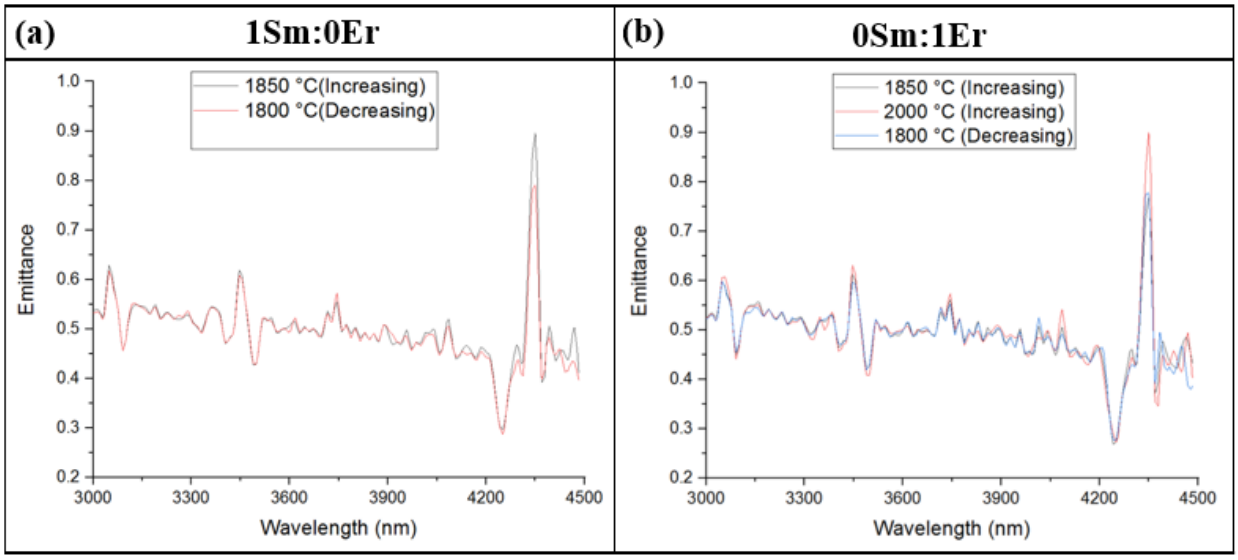

Figure 35: Emittance versus wavelength profiles at 1850°C, 2000°C and 1800 °C from 1500-3000 nm for: (a) 1Sm:0Er, and (b) 0Sm:1Er.

Figures 36a-c show the emittance versus wavelength profiles from 1500-3000 nm at 1850°C, 2000°C and 1800 °C for the 2Sm:1Er, 1Sm:1Er, and 1Sm:2Er samples. For the 2Sm:1Er sample, it is shown that the emittance slightly increases with temperature at shorter wavelengths but as the wavelength is further increased, the emittance remains mainly constant as the main oxide scale was m-ZrO_2. Also, for the 2Sm:1Er sample, at the highest emittance peaks the emittance increases by increasing the temperature. For the 1Sm:1Er sample, it is shown that the emittance decreases by increasing the temperature from 1500-2050 nm. Also, the 1Sm:1Er sample shows that at the lowest emittance peaks the emittance decrease by increasing the temperature (point A), whereas at the two highest emittance peaks (points B, C), the emittance increases by increasing the temperature. Finally, for the 1Sm:2Er sample, the emittance decreases by increasing the temperature from 1500-2050 nm. Furthermore, Figure 36a-c clearly shows that as the incorporated Er concentration is increased from 1.23 mol.% in the 2Sm:1Er sample to 2.33 mol.% in the 1Sm:2Er sample, the emittance increases at shorter wavelengths (1500-2050 nm). Also, the emittance variation with temperature from 1500-2050 nm increases as the Er mol.% increases.

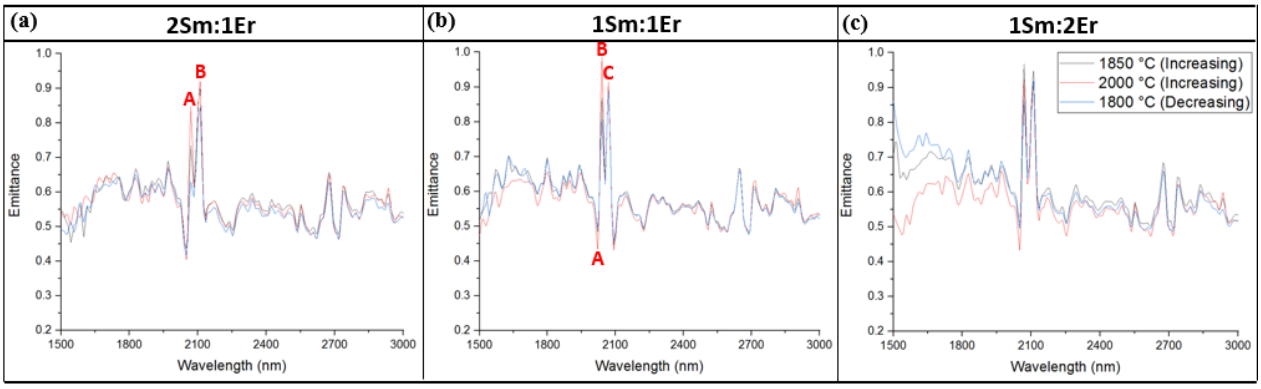

Figure 36: Emittance versus wavelength at 1850°C, 2000°C and 1800 °C from 1500-3000 nm for: (a) 2Sm:1Er, (b) 1Sm:1Er, and (c) 1Sm:2Er.

Figures 37a-c show the emittance versus wavelength profiles from 1500-3000 nm at 1850°C, 2000°C and 1800 °C for the 2Sm:1Er, 1Sm:1Er, and 1Sm:2Er samples. The emittance profiles for the 2Sm:1Er, 1Sm:1Er and 1Sm:2Er samples at 1850 °C, 2000°C and 1800 °C is basically the same. The only significant change on all of them occurred at the maximum emittance peak located at ~4355 nm where the emittance of the 1Sm:1Er and 1Sm:2Er samples increase by increasing the temperature, whereas the emittance of the 2Sm:1Er sample decrease by increasing the temperature.

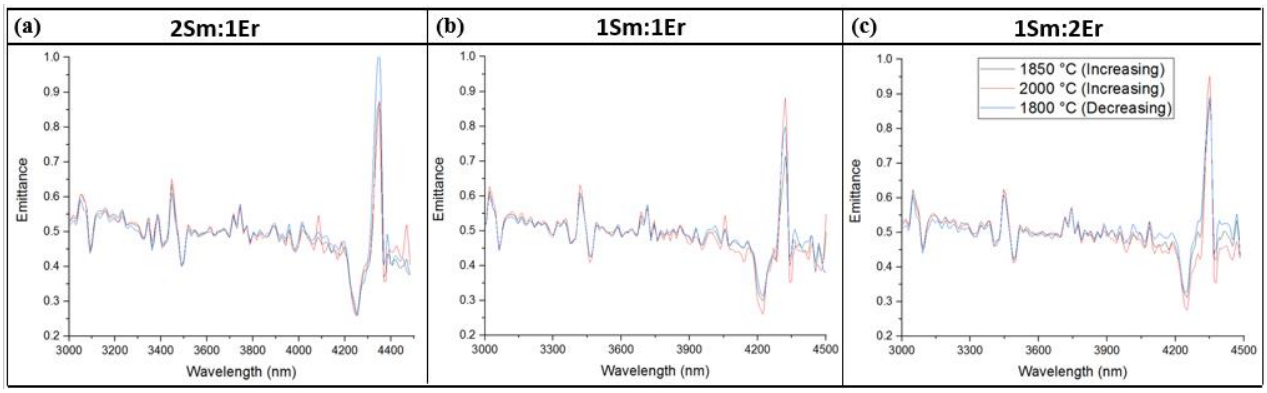

Figure 37: Emittance versus wavelength at 1850°C, 2000°C and 1800 °C from 3000-4500 nm for: (a) 2Sm:1Er, (b) 1Sm:1Er, and (c) 1Sm:2Er.

Figures 38a-b show the emittance versus wavelength profiles for all the five different Sm:Er molar ratios at a constant temperature of 1865°C. Figure 38a shows that the emittance values from 1500-1900 nm were the highest for the 1Sm:1Er and 2Sm:1Er samples. Also, Figure 38a shows that the emittance variation is more significant at shorter wavelengths (1500-1750 nm). Figure 38b shows that at larger wavelength ranges (2000-2700 nm) the emittance variation is higher at the maximum and minimum emittance peaks than in the other parts of the emittance profile. very small. Several maximum and minimum emittance peaks can be seen for all the five Sm:Er molar ratios.

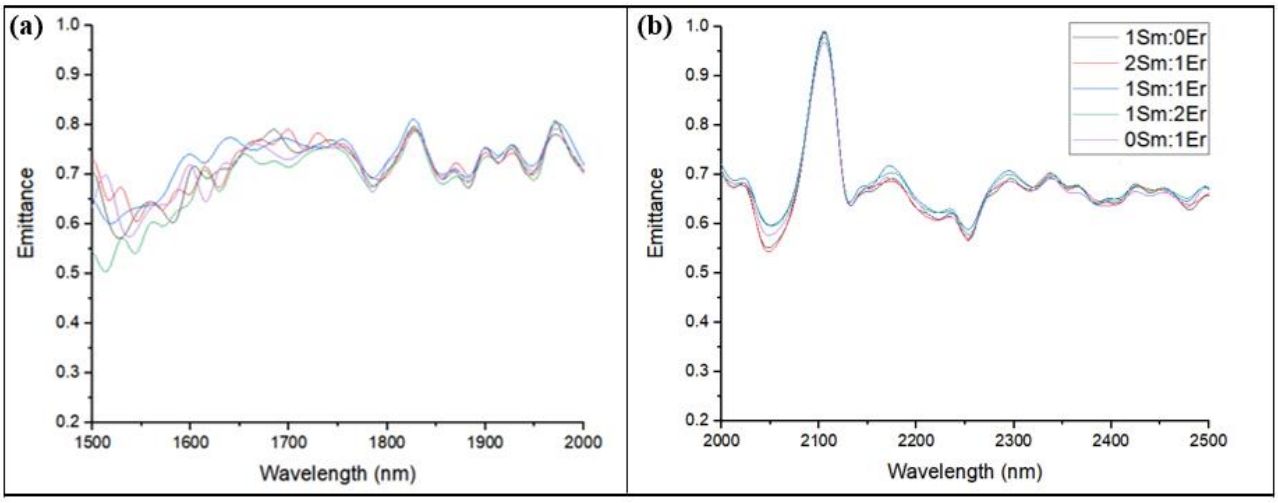

Figure 38: Emittance versus wavelength profile as function of the molar dopant concentration at 1865 °C for a wavelength range of: (a) 1500-2000 nm, and (b) 2000-2600 nm.

3. Discussion

3.1 Factors Influencing the Emittance

Thermally emitted spectral radiance from a surface depends on two main aspects: (1) the surface temperature, which results from the equilibrium thermodynamic state caused by the heat transfer energy balance between the surface of the sample and its environment; and (2) the emittance, which depends on the material composition, temperature, wavelength, surface roughness, and sample thickness. The present analysis will be focused on the emittance.

3.1.1 Sm and Er Dopant Concentration Effect on the Emittance of ZBS Systems

The first factor affecting the emittance is the material composition. Previous studies have demonstrated that the emittance of ZrO_2 can be increased via doping with rare-earths oxides which intentionally introduce defects into a pure material.[3–6] As the dopant concentration is increased, the absorption raises in the wavelength range studied in this paper (1500-5000 nm).[7] Although the total RE incorporated in the samples of the present study is constant at ~3 mol%, the actual Sm incorporated varies from 0-2.94 mol%, while the actual Er incorporated varies from 0-3.11 mol%. As both Sm^{3+} and Er^{3+} have a different electronic structure, the absorption spectra depend on the actual amount of each RE ions being incorporated. As an increase of the RE ions concentration of either Sm^{3+} or Er^{3+} raises the number of free electrons, more electrons within the present band of interest (1500-5000 nm) absorb more radiation by moving from a low to an empty high energy level.[7] Based on these findings, it is worth to analyze the dopant concentration effect of Sm^{3+} or Er^{3+} in the electronic structure of ZrO_2.

Avdoshenko *et al.*[3] studied the high-temperature emittance of ZrO_2 and Sm_2O_3 by using density functional theory simulations to compare the emittance behavior under three different conditions: defect-free, oxygen vacancies and *f*-shell states.[3] The results for systems with oxygen vacancies showed that for a thickness of 10 μm at 1727 ^oC, neutral oxygen vacancies contribute significantly to the high emittance of ZrO_2 by increasing its value from 0.3 for a defect-free system

to 0.6, while for the Sm_2O_3 the emittance value is increased from 0.15 to 0.23 under the same conditions[3]. It is worth to analyze the electronic changes induced by the oxygen vacancies to understand these differences. The defect introduced in ZrO_2 causes a mid-gap state with the donor essence, which enables a vertical excitation that influences significantly to the emittance spectra and enhances its value to 0.6 at 1727 ^oC.[3] For Sm_2O_3, the increase in the emittance is produced by localized additional electronic states within the material band gap which are caused by both point defects such as oxygen vacancies which create an acceptor state and localized *f*-electron states.[3,8] These localized electronic states, either acceptor or donor in nature, leads to added transitions that increase the overall dielectric response, and therefore, can modify the emittance.[3] As a result, by understanding the effect of these defects, there is an opportunity to tailor the emittance for hypersonic applications.

The electronic structure for the Sm^{+3} ions is given by [Xe] $4f^5$ in which the number of *f*-electrons in each Sm^{+3} determines its spectral properties.[3] As a result, the absorption spectra in the wavelength range of interest here is very high. The experimental value of emittance for Sm_2O_3 at 1727 ^oC is 0.8 and its melting temperature is ~1827 ^oC.[9] Furthermore, another effect caused by the Sm and Er dopants is the crystal distortion due to different ion radii, which also has an influence to radiation.[7]

Unfortunately, the beneficial c_1-$(Sm/Er)_{0.2}Zr_{0.8}O_{1.9}$ was not the major oxide phase formed in the front surface (spectrometer side) of the 1sm:0Er, 2Sm:1Er, 1Sm:1Er and 1Sm:2Er samples. The major oxide scale formed on these samples was *m*-ZrO_2. It is speculated that the test assembly affected the XRD results. As the samples were heated on the back side, the back side (laser side) reached higher temperatures than the spectrometer side, and therefore, the majority of the Sm and Er atoms diffused to the back side of the sample by a convection cell mechanism.[10–14] As a result of the minimal amount of Sm and Er atoms available in the spectrometer side, just a minimal amount of the beneficial c_1-$(Sm/Er)_{0.2}Zr_{0.8}O_{1.9}$ was able to form on the spectrometer side. It represent a huge difference as the emittance profile of *m*-ZrO_2 and c_1-$(Sm/Er)_{0.2}Zr_{0.8}O_{1.9}$ is totally different. A possible way to solve this issue could be to increase the total amount of rare-earth incorporated from 3 mol.% to 5 mol.%.

In the case of amorphous silica, it is known that it has a low emittance at high temperatures and the existence of point defects does not increase its value significantly.[3] Therefore, it is speculated that the minimum amount of the amorphous silica that observed in the XRD results of figure 32, slightly decrease the emittance values observed in Figures 34-38.

3.1.2 Temperature and Wavelength Effect on the Emittance of ZBS Systems

An increase in temperature increases the thermal movement of atoms in the lattice. The thermal movement of atoms influence the electronic and optical response of oxides.[3] Therefore, it is expected that an increase in temperature will affect the emittance of the *m*-ZrO_2 and the c_1-$(Sm/Er)_{0.2}Zr_{0.8}O_{1.9}$ formed during the laser heating test as shown by the XRD results on Figure 32. Figures 34-38 shows that the effect on emittance by increasing the temperature is directly related with the wavelength.

Figures 36a-c shows that at shorter wavelengths ranges (1500-2050 nm), the emittance decrease more with increasing temperature as the Er concentration is increased from 1.23 mol.% in the 2Sm:1Er sample to 2.33 mol.% in the 1Sm:2Er sample. The increase in emittance variation

at shorter wavelengths ranges from 1500-2050 nm can be explained by the Wien's displacement law which shows that the maximum spectral emissive power is displaced to shorter wavelengths with increasing temperature.[15,16] Therefore, it is expected that the emittance versus wavelength profile will be more sensitive at shorter wavelengths. Based on the results shown in Figures 36a-c, it is evident that the Er concentration is having a bigger effect on the ZBS sintered billets than the Sm concentration. This is also conformed by the XRD results shown in Figure 32, where as the Er concentration is increased the amount of the c_1-$(Sm/Er)_{0.2}Zr_{0.8}O_{1.9}$ phase also increases until it reaches a point in which this phase becomes the major oxide scale as in the 0Sm:1Er sample.

Figures 34-38 shows that several maximum and minimum emittance peaks are obtained because of doping the ZBS billets with rare-earth oxides. The three maximum emittance peaks were at ~2069 nm, ~2112 nm and ~4355 nm, whereas the minimum emittance peaks were at ~2055 nm, 3361 nm and 4313 nm. By looking at both the Sm_2O_3 and Er_2O_3 emittance profiles, it is speculated that the maximum and minimum emittance peaks were caused by the Er_2O_3 as its emittance profile its similar to the ones observed in Figures 34-38.

Based on the results, it is evident that the erbium oxide is modifying the emittance profile as can be seen by the maximum and minimum emittance peaks. Though, the effect of varying the Sm:Er molar ratios is not clear as the emittance profile of all samples is similar. It is speculated that if the total dopant concentration incorporated is augmented from 3 mol.% to 5 mol.%, the beneficial c1-$(Sm/Er)_{0.2}Zr_{0.9}O_{1.8}$ could be formed, producing a large difference.

3.1.3 Thickness and Surface Roughness Effect on the Emittance

It is well known from Kirchhoff law that, in equilibrium, the amount of electromagnetic energy absorbed by a body at a specific wavelength is emitted at the same wavelength. Therefore, the emittance is high for wavelengths around the absorption range. If the thickness of the sintered sample is increased, the emittance should increase due to higher absorption. Studies have shown the emittance initially increase by increasing the thickness, reaches a maximum value, and eventually remains constant. For example, studies on alumina shows that emittance increase by increasing thickness up to 40 μm, and then remains mainly constant.[7] Furthermore, in Avdoshenko study, it is shown that at 1727 ^oC the emittance of ZrO_2 is increased from 0.60 at a thickness of 10 μm to 0.78 at a thickness of 100 μm, while the emittance of Sm_2O_3 is increased from 0.72 at a thickness of 10 μm to 0.88 at a thickness of 100 μm.[3] Although the thickness of the samples in the present study were maintained constant at ~2 mm, it can be said that this thickness value is higher than the critical thickness where the emittance starts to be have mainly constant.

The surface roughness of surfaces can be characterized based on the ratio between surface roughness to wavelength (σ/λ) in three different regions: the specular zone ($\sigma/\lambda < 0.2$), intermediate zone ($0.2 < \sigma/\lambda < 1$) and the geometric region ($\sigma/\lambda > 0.2$). As the surface roughness value in the present study was held constant at ~100 nm, the wavelength range being analyzed in this study (1500-5000 nm) is in the specular region. However, as the surface roughness was maintained constant through all the experiment, its effect should be the same to all the tested samples.

4. Conclusions

The emittance of sintered billets with five different Sm:Er molar ratios were evaluated at the RHINO lab at the Air Force Research Laboratory. The maximum emittance peaks for all the Sm:Er molar ratios were 2069 nm, 2112 nm, and 2680 nm, whereas the minimum emittance peaks were 2055 nm, and 3091 nm. XRD results shows that *m*-ZrO_2 was the major phase with minor portions of c1-$(Sm/Er)_{0.2}Zr_{0.9}O_{1.8}$. Emittance profiles for both 1Sm:0Er and 0Sm:1Er samples were very similar from 1500-3000 nm. Emittance increase from 1500-2050 nm by increasing the Er mol.% in the samples containing both Sm and Er. The emittance peak for Er_2O_3 at ~1.5 μm could be causing the ε to be higher as the Er mol.% increases. Emittance profiles remains constant by increasing the temperature from 3000-4500 nm for all the Sm:Er ratios. Despite the emittance profile is similar as function of dopant concentration at T=1865 °C, emittance differences are seen at peaks and short wavelengths. Based on the results, it is evident that the erbium oxide is influencing the emittance profile as can be noted by the maximum and minimum emittance peaks. However, the effect of varying the Sm:Er molar ratios is not clear as the emittance profile of all samples is similar. It is speculated that if the total dopant concentration incorporated is increased from 3 mol.% to 5 mol.%, the beneficial c1-$(Sm/Er)_{0.2}Zr_{0.9}O_{1.8}$ could be formed, causing a big difference. Also, the test setup influences the emittance profile as the spectral radiance was obtained from the front side of the sample instead of the back side where the samples were heated. This study represents the first generation of UHTC for hypersonic vehicles by doping ZBS systems with both Sm and Er elements.

References

1. Saunders, P. Propagation of uncertainty for non-linear calibration equations with an application in radiation thermometry. (2003).
2. Saunders, P. & White, D. R. Physical basis of interpolation equations for radiation thermometry. (2003).
3. Avdoshenko, S. M. & Strachan, A. High-temperature emissivity of silica , zirconia and samaria from ab initio simulations : role of defects and disorder High-temperature emissivity of silica , zirconia and samaria from ab initio simulations : role of defects and disorder. doi:10.1088/0965-0393/22/7/075004
4. Tan, W., Adducci, M. & Trice, R. Evaluation of Rare-Earth Modified ZrB 2 – SiC Ablation Resistance Using an Oxyacetylene Torch. **2645,** 2639–2646 (2014).
5. Tan, W., Adducci, M., Petorak, C., Brenner, A. E. & Trice, R. W. Effect of rare-earth dopant (Sm) concentration on total hemispherical emissivity and ablation resistance of ZrB2/SiC coatings. *J. Eur. Ceram. Soc.* 1–9 (2016). doi:10.1016/j.jeurceramsoc.2016.04.013
6. Kenyon, A. J. *Recent developments in rare-earth doped materials for optoelectronics*. **26,** (2002).
7. He, X., Li, Y., Wang, L., Sun, Y. & Zhang, S. High emissivity coatings for high temperature

application : Progress and prospect. *Thin Solid Films* **517,** 5120–5129 (2009).

8. Gorter, C. J. & Hoogschagen, J. , 4ND THE MULTIPOLE CHARACTER. (1945).
9. Tan, W., Petorak, C. A. & Trice, R. W. Rare-earth modified zirconium diboride high emissivity coatings for hypersonic applications. *J. Eur. Ceram. Soc.* **34,** 1–11 (2014).
10. Karlsdottir, S. N. & Halloran, J. W. Formation of Oxide Films on ZrB2–15 vol% SiC Composites During Oxidation: Evolution with Time and Temperature. *J. Am. Ceram. Soc.* **92,** 1328–1332 (2009).
11. Karlsdottir, S. N., Halloran, J. W. & Henderson, C. E. Convection patterns in liquid oxide films on ZrB2-SiC composites oxidized at a high temperature. *J. Am. Ceram. Soc.* **90,** 2863–2867 (2007).
12. Karlsdottir, S. N. & Halloran, J. W. Oxidation : Evolution with Time and Temperature. **1332,** 1328–1332 (2009).
13. Gangireddy, S., Karlsdottir, S. N., Norton, S. J., Tucker, J. C. & Halloran, J. W. In situ microscopy observation of liquid flow , zirconia growth , and CO bubble formation during high temperature oxidation of zirconium diboride – silicon carbide. *J. Eur. Ceram. Soc.* **30,** 2365–2374 (2010).
14. Brenner, A. E. *et al.* Cyclic ablation of high-emissivity Sm-doped ZrB<inf>2</inf>/SiC coatings on alumina substrates. *J. Eur. Ceram. Soc.* **38,** (2018).
15. Radiation, T. Thermal radiation 13.0. 578–655 (2018).
16. Ilic, O. *et al.* Tailoring high-temperature radiation and the resurrection of the incandescent source. **11,** (2016).

Accomplishment 6: Air-Force Research Laboratory Collaboration on the Emittance of RE-Doped Billets

1.0 Introduction

Sharp leading-edge designs for hypersonic vehicles improve performance by reducing aerodynamic drag. However, sharp edges lead to convective heating resulting in temperatures exceeding 2000^{o}C. [1] Ultra-high temperature ceramics (UHTC) are among the materials being considered for leading edges, specifically ZrB_2-SiC (ZBS) which has a high melting point, thermal shock resistance, thermal conductivity and at 1500^{o}C and above. [2,3,4] While the material property thermal conductivity helps distribute the heat, emissivity is the only material property that will help cool the leading-edge system by re-radiating the heat out to the environment.

Studies performed by Tan et. al. [3,6] have shown that adding samarium (Sm) dopant to the ZBS system increases the emittance compared to ceramics comprised only of ZBS. Specifically, in a study where the total hemispherical emittance was tested on a 5 mol% Sm-doped ZBS plasma sprayed coating, it was found to have an emittance of 0.9 at 1600^{o}C. [3] In addition, the Sm dopant improved ablation performance by forming a stable oxide scale of c_1-$Sm_{0.2}Zr_{0.8}O_{1.9}$ (SZO) which has a melting point above 2500^{o}C, making it capable of withstanding extreme temperature conditions during hypersonic flight.

In the SmZBS system, it is unknown how microstructure effects both the emittance and ablation performance. Tan et. al. [6] found that there were differences in emittances with different Sm concentrations, however their beginning microstructure was also different. Microstructure was found to affect emittance here [7,8,9]. However, little research has been done on how emittance performance is affected by microstructure at ultra-high temperatures. [9, 10, 11]. Thus it was deemed important to investigate. In this study, the oxide scale of 3mol% Sm-doped ZBS billets with different surface finishes and densities were ablated for 60s using an oxyacetylene torch. The samples emittances were also tested at the RHINO lab at the Air Force Research Laboratories. The phase assemblages and microstructures were analyzed using XRD, SEM, and EDS.

2.0 Experimental Procedure

2.1 Materials and powder preparation

Spray-dried powders were prepared from a suspension that consisted of 80 vol.% ZrB_2 (3–5 μm, Grade A, HC Starck, Munich, Germany), 20 vol.% α-SiC (1.4 m, Grade UF-05, HC Starck, Munich, Germany), 0.4 wt.% dispersant (Darvan 821A, R.T. Vanderbilt Company, Inc., Norwalk, USA), 2 wt.% PVA binder (Celvol 203, Celanese Corporation, Dallas, USA) and DI water. Spray drying was performed by Arch Instant Spray Drying Services, Brunswick, GA. The average spray-dried particle size was ~50 μm. Samarium dopant was added to the spray dried ZrB_2/SiC powders via a chemical infiltration method. In this process, 10 mol.% samarium nitrate hexahydrate (99.9% pure $Sm(NO_3)_3 \cdot 6H2O$, Sigma-Aldrich, St. Louis, USA) was dissolved into isopropyl alcohol and

the resulting solution was then infiltrated into the porous spray-dried ZrB_2/SiC powder. Next, the solvent was removed via a rotary evaporator (BM 200, Yamato Scientific America Inc., Santa Clara, USA) at 100°C. This powder was heated at 400°C in air for an hour to remove residual moisture and nitrates. Tan et al.[3] showed that below 400 °C both the ZBS and the Sm-doped powders did not have any weight gain. As the normalize weight gain was approximate zero below 400°C, it suggests that the oxidation of the powders has little effect during the heat treatment at 400°C. The first weight gain inflections start near 600°C due to the oxidation of ZrB_2 to form m-ZrO_2 and B_2O_3 glass [3].

Subsequently, the dried mixture was crushed and sieved using a -325 mesh (40 μm aperture) to eliminate large agglomerates. The powder was then pressed into 38mm x 38mm x 5mm billets at 6 metric tons at room temperature and sandwiched between two SiC plates layered with graphite and sprayed with boron nitride. The purpose of the SiC plates was to avoid bloating of the samples due to outgassing during sintering. The pressed billets were then sintered in argon at 2000oC for 15 minutes (Series System VI, Centorr Vacuum Industries, Nashua, USA). A 1-hr hold at 1650^{o}C, prior to reaching 2000^{o}C, was programed into the heating cycle to evaporate off the boria glass formed from the boron nitride. The densities of the sintered billets was 87±2% and measured by Archimedes' method in the ASTM C37388[12] and compared to a theoretical density of 6.36 g/cm^3. The billets had a linear shrinkage of ~20% in x and y and ~40% shrinkage in the thickness. Samples with densities of 79% and 69% were also fabricated by changing the hold temperature to 1925^{o}C and 1850^{o}C respectively. They were then cut to 25.4mm x 25.4 mm and polished using an automatic polisher (GPX Series Advanced Autopolisher, LECO Corp., St. Joseph, USA) to an R_a of 0.4±0.1μm which was measured via atomic force microscopy (AFM). (Dimension 5000 AFM, Bruker, Santa Barbara, USA) Samples where surface finish was varied were then abraded for 10s on the automatic polisher using diamond sprays of 3μm and 6μm to achieve R_a values of 0.9±0.2μm and 1.4±0.3μm. The composition of the billets was measured by mass spectroscopy and comprised of 29.8 mol% Zr, 56.7% B, 7% C, 0.5% Si, 3% Sm, 2.8% O, and 0.2% impurities. (NSL Analytical Services Inc., Cleveland, USA)

2.4 Microstructural and phase analysis

Before performing the microstructural analysis the samples were coated with a thin layer of Au/Pd. A scanning electron microscope (SEM) (Quant 650 FEG, Thermo Fischer Scientific, Hillsboro, USA) was used to characterize coating topography in the as-sprayed conditions after each cycle. X-ray diffraction (XRD) (D8 Focus, Bruker Corporation, Billerica, USA) was used to investigate the phases present. Cu Kα radiation was used over 2θ values of 20°-80° on the coatings after ablation using a step size of 0.02° and a scan rate of 5°/minute. Samples were aligned in the XRD to analyze the regions where the ablation flame was most intense. AFM (Dimension 500 AFM, Bruker, Santa Barbara, USA) was used to measure the pre-ablated average surface roughness (R_a) of the specimens over a 300+ μm^2 area in contact mode using a speed of 350 points/second.

3.0 Results and Discussion

3.1 As-sintered microstructure and phase analysis of Sm-Doped ZBS

Table 4: Measured densities, porosities, surface roughnesses of pre-heated billets and max temperatures reached during laser heating

Sample	Density (%)	Open Porosity(%)	Ra (µm)	Max Temperature Reached (^{o}C)
D1R1	87	7.5	0.4±0.1	1656
D1R2	87	7.5	0.9±0.2	1768
D1R3	87	7.5	1.4±0.3	1818
D2R1	79	14	1.0±0.2	1763
D3R1	69	24	1.1±0.2	1855

The density, surface roughness, and porosity are listed in Table 4. It should be noted there is an increase in roughness as the density decreases, however porosity can also contribute to the Ra value obtained and is the cause for the increase. The density decreases as sintering temperature is decreased. The top microstructure of R1-R3 and D1-D3 and cross-sectional microstructure can be seen in Figure 39. The cross-sections in Figure 39 show both the ZrB_2 grains surrounded by a Sm containing matrix with random dispersions of SiC. As density decreases the porosity of the sample increases. The pores are elongated and ellipsoidal in nature.

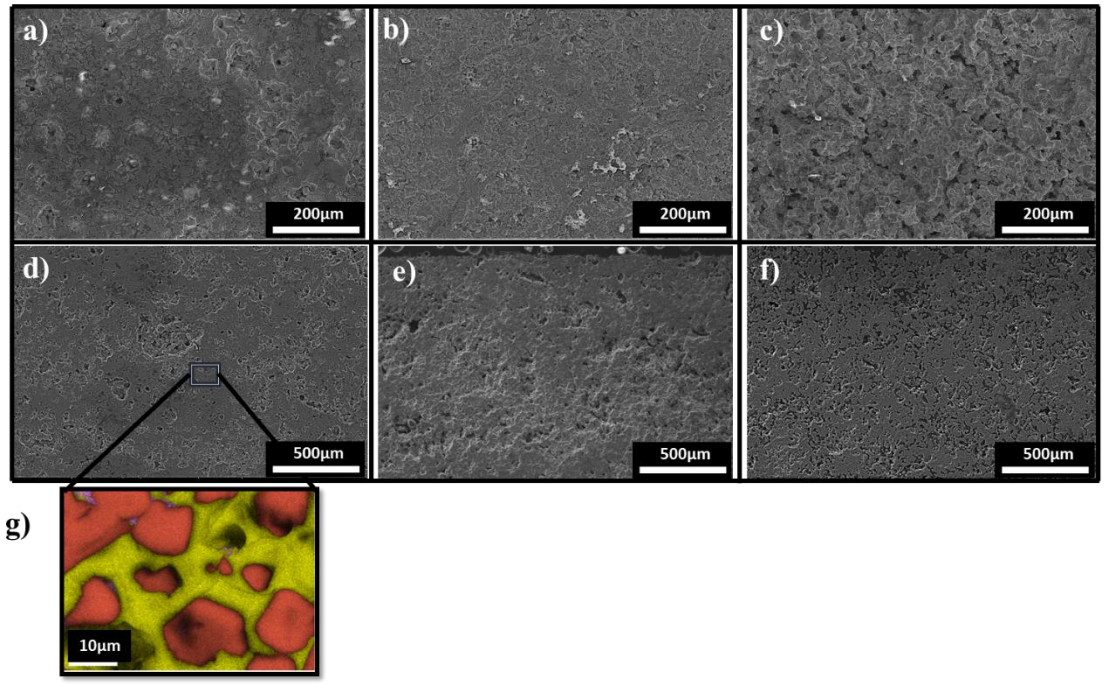

Figure 39: Surface SE SEM microstructural images of a)D1R1, b)D1R2, and c)D1R3. Also cross-sectional micrographs of d)D1R1, e)D2R1, and f)D3R1. Enlarged area of an EDS scan g) in D1R1 showing ZrB_2(red), SmB_2C_2(yellow), and SiC(purple).

The ZrB_2 grains can be seen surrounded by a Sm containing matrix with little pockets of SiC. XRD results, as seen in Figure 40, show the predominant phase is ZrB_2, with small peaks correlating to a SmB_2C_2 matrix. This correlates to what is seen in Figure 39 where the red phase is ZrB_2, yellow is SmB_2C_2, and purple is SiC, however SiC is not picked up by XRD. Small amounts of ZrC and $SmBO_3$ peaks are also visible in the pre-ablated XRD scan, however more so in the 69% dense sample. It is believed the sintering temperature used to obtain a 69% density was the optimal temperature to form the ZrC. The oxidation of the SiC to SiO and CO during sintering coupled with the degradation of Sm_2O_3 from the pre-sintered powders in the reducing atmosphere is believed to result in the formation of the ZrC, SmB_2C_2, $SmBO_3$, and loss of SiC in the billets. Similar reactions also occurred with pressureless sintered Y_2O_3/ SiC. [13] Previous studies on pressureless sintering on ZrB2-SiC ceramics has been with hold times of 1hr+ at similar temperatures that reached densities of 99%. [14] However for our studies it was found that increased hold time had little effect on resultant density.

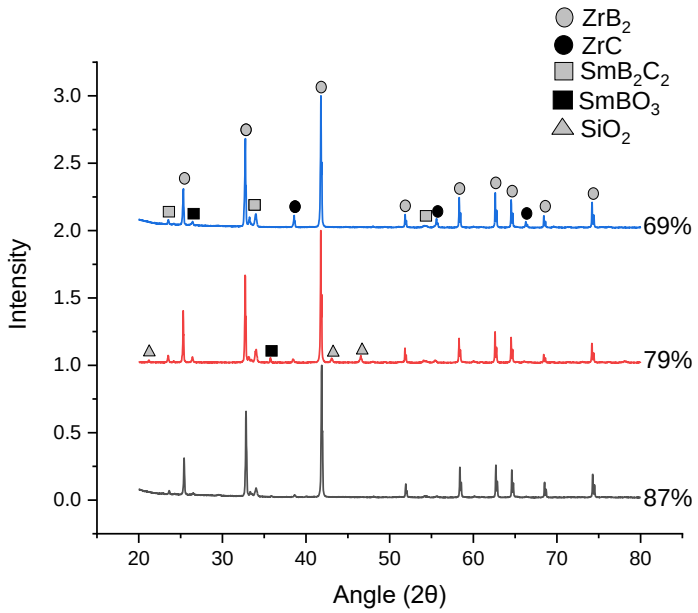

Figure 40: XRD pattern of the pre-heated surface of billets of D1R1, D2R1, and D3R1.

3.2 Post laser heated SmZBS with different roughness and densities resulted in same microstructure

The max temperature reached for each condition at powers of 700W, 800W, and 900W are seen in Table 5. Increase in temperature with increase in power was not constant for each sample condition. This most likely due to the differences in thicknesses.

Sample	Pre-ablation Phases	Post-Ablation Phases	Max Temperature Reached (^{0}C) Per Power		
			700W	800W	900W
D1R1	ZrB_2, SmB_2C_2, ZrC	m-ZrO_2, Sm_2O_3, c_1-$Sm_{0.2}Zr_{0.8}O_{1.9}$	2108	2094	2226
D1R2	ZrB_2, SmB_2C_2, ZrC	m-ZrO_2, Sm_2O_3, c_1-$Sm_{0.2}Zr_{0.8}O_{1.9}$	1878	2009	2133
D1R3	ZrB_2, SmB_2C_2, ZrC	m-ZrO_2, Sm_2O_3, c_1-$Sm_{0.2}Zr_{0.8}O_{1.9}$	1937	2041	2179
D2R1	ZrB_2, SmB_2C_2, ZrC	m-ZrO_2, Sm_2O_3, c_1-$Sm_{0.2}Zr_{0.8}O_{1.9}$	2197	2407	2327
D3R1	ZrB_2, SmB_2C_2, ZrC	m-ZrO_2, Sm_2O_3, c_1-$Sm_{0.2}Zr_{0.8}O_{1.9}$	1990	2142	2231

Table 5: Phases present in pre-ablated and post-laser-ablated billets as well as max temperature reached at each power condition.

The post ablated surfaces for all the samples show there is little differences in microstructure as seen in Figure 41, except for D3R1. D3R1 contains smaller oxide grains and large cracks. This is likely due to the starting porosity, however EDS results are consistent with all other samples. Similarity in microstructure is believed to be due to the formation and bursting

of convectional cells as described in a previous section. Crystalline structures of Zr, Sm, and O can be seen surrounded by a Sm, O, and Si glassy phase. Atomic% and wt% of the different elements in the two distict phase regions can be seen in Table 3.

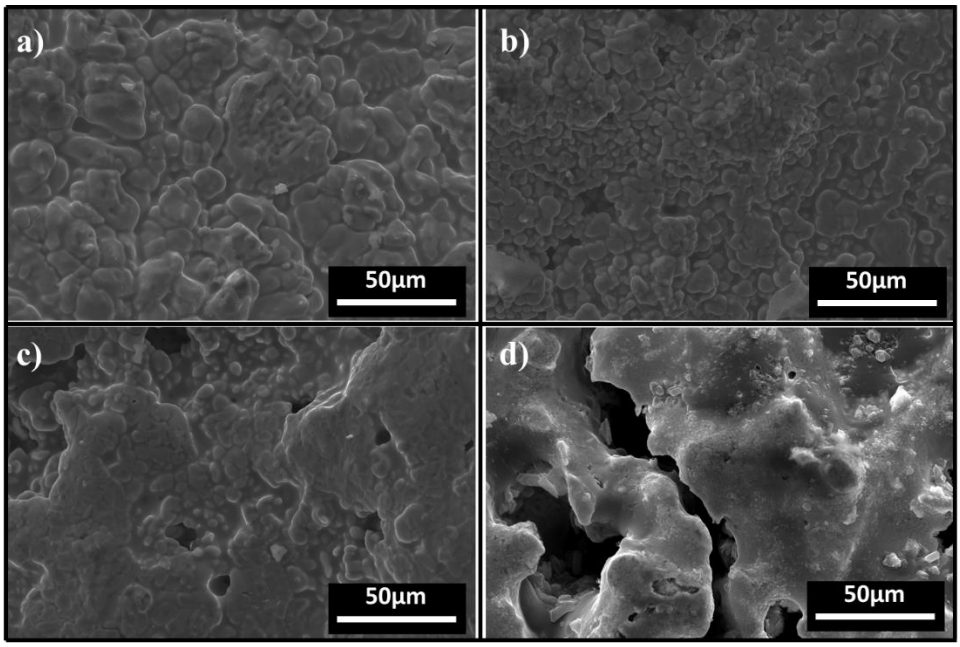

Figure 41: SEM SE micrographs of post-laser ablated a) D1R2, b)D1R3, c)D2R1, and d)D3R1.

XRD analysis of the different conditions at powers of 700W, 800W, and 900W all show a main phase of m-ZrO_2 (JCPDS-00-78-0047)with minuscule peaks of Sm_2O_3 (JCPDS-00-74-1807) and c_1-$Sm_{0.2}Zr_{0.8}O_{1.9}$ (JCPDS-01-78-1302) present in the XRD scan seen in Figure 42 and Table 5. In the Sm_2O_3-ZrO_2 phase diagram in Figure 43, it can be seen the reason we are not forming c_1-$Sm_{0.2}Zr_{0.8}O_{1.9}$ is because there is simply not enough Sm in the system on the radiance side of the sample. Although a small amount of c_1-$Sm_{0.2}Zr_{0.8}O_{1.9}$ is formed as seen in XRD, there is not enough to dope most of the m-ZrO_2. At temperatures of ~2000^{o}C, least 7 mol% is needed to form c_1-$Sm_{0.2}Zr_{0.8}O_{1.9}$. As mentioned in previous studies Sm incorporates into the Si and is pushed up through the expansion of oxidizing ZrB_2. As the Si is evaporated off, the Sm is left behind leaving a higher concentration on the surface. [15] With the laser side of the samples heating at a rapid pace and melting through the sample compared to the radiance side, it is likely the majority of the Sm flowed towards the laser side. This is due to the depletion of Si at a faster rate on the laser side compared to the radiance side.

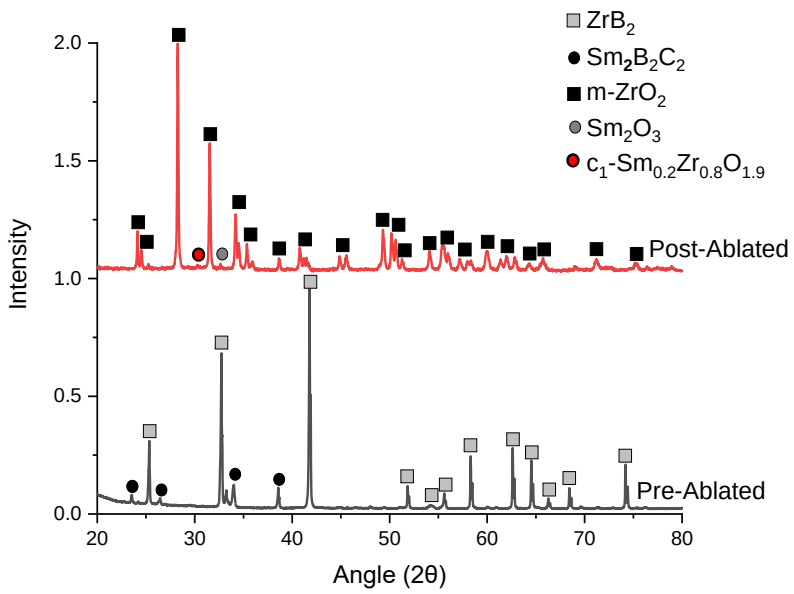

Figure 42: XRD of pre- and post-ablated billet surfaces of D1R2.

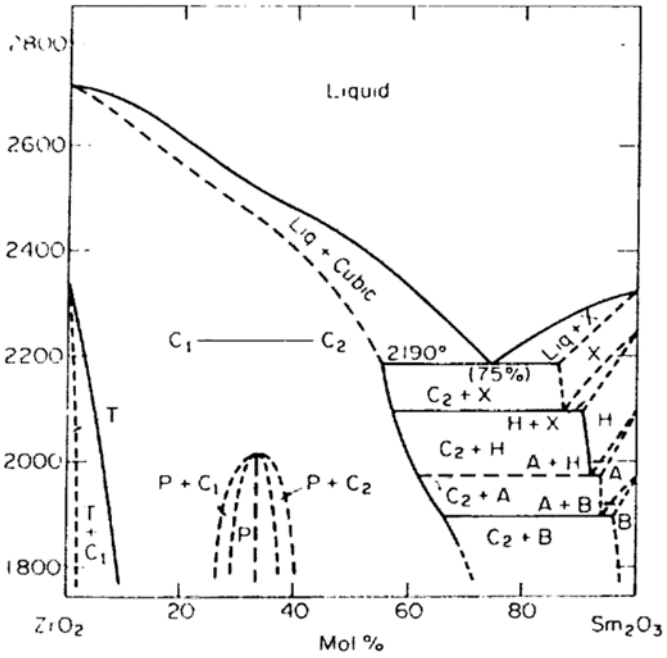

Figure 43: ZrO_2-Sm_2O_3 phase diagram.

It should be noted again that the side where radiance was measured was the non-laser heated side and conditions were not similar to the oxyacetylene ablation experiments performed on Sm-doped ZBS. [6,15,16] In these experiments, there was a higher oxygen partial pressure compared to what is normally in the air.

Laser heating of the back side of the billet without the addition of extra oxygen also likely caused the formation of m-ZrO_2 and not c_1-$Sm_{0.2}Zr_{0.8}O_{1.9}$. In studies done on ZrB_2/SiC at lower oxygen partial pressures, it was found that as PO_2 decreased, the active oxidation of SiC in the sample increased while the active oxidation of ZrB_2 decreased. [17,18] Although a large amount Si of was not seen on the surface this was likely due to two reasons: first that the amount of SiC in the sample to start was low. EDS indicated only 4 atomic% Si was present on the surface along with 61 atomic% O, 3 atomic% Sm, 18 atomic% Zr, and 15 atomic% C which was likely due to contamination from the graphite holder.

Secondly as mentioned previously the sample was heated on the opposite side of what was investigated. It is well known that during oxidation a SiO_2 scale and depletion layer forms due to the oxidation of ZrB_2. [19-24] The samples investigated were again hit with a laser on the opposite side and formed an oxide that was melted through most of the sample thickness as seen in Figure 44.

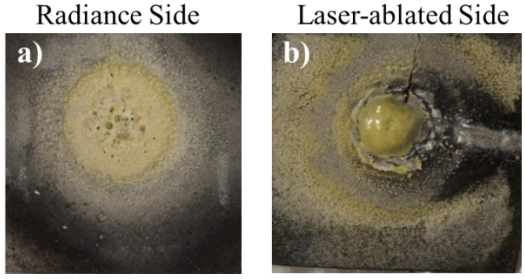

Figure 44: Spectrometer side where radiance data was collected and b) laser ablated side where sample was heated.

It is likely that most of the Si was depleted to the other side first due to the increase in temperature compared to what the investigated side experienced. Despite the likely consumption of Si in the sample on the opposite side, the investigated billets also reached temperatures exceeding 1800^{o}C, most of which exceeded 2000^{o}C. Residual white matter from condensation of the evaporated products was collected from the graphite holder post laser ablation and contained mainly B_2O_3 as well as SiO_2. It is likely most of the silica that was present on the surface evaporated off.

3.3 Spectral emittance of Sm-ZBS with differing surface roughness and densities

Spectral emittance testing resulted in almost identical results for all samples tested. This was expected due to the formation of slightly Sm doped m-ZrO_2 for all of the samples as well as similar microstructures. As temperature is increased the emittance remains relatively unchanged as seen in Figure 45. It can also be seen the density as well as surface roughness has little to no effect on the emittance as a function of temperature in Figure 45. In both graphs, the average emittance was ~0.35 across a temperature range of 1200^{o}C-2200^{o}C. The wavelength was held constant at 3000nm. These results were also consistent for wavelengths held at 1997nm and 4000nm, however the average emittance at a wavelength of 1997nm increased to ~0.4 from 1600-2200^{o}C. A study done by Liebert [25] on zirconia on the emittance as a function of temperature, it was found that in the temperature range of 700K-2700K (427^{o}C-2427^{o}C) the total hemispherical

emittance was found to decrease as temperature increased. This was also the same the spectral emittance in the range of 1.5µm-4µm for YSZ. [26] However, this was the opposite of what was found by Chekhovskoi et. al. [27] on fused ZrO_2 in the spectral range of 530-650nm. At these wavelengths the average emittance started at 0.3 at 1400°C and increased to 0.6 at 1800°C.

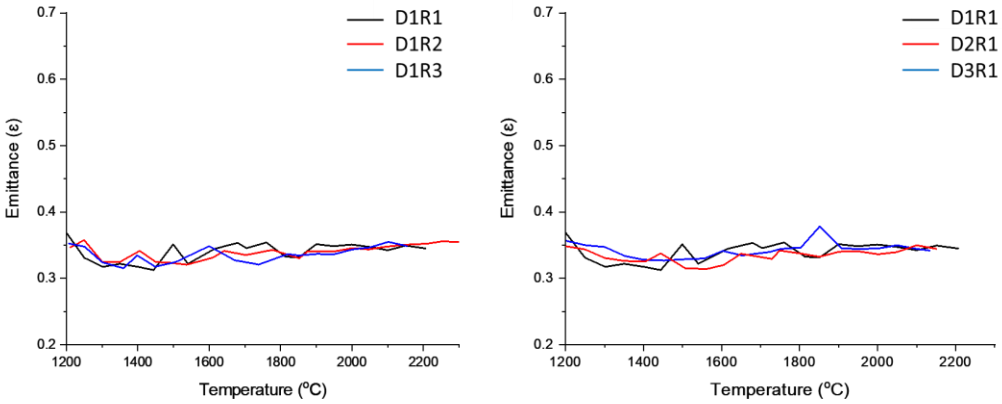

Figure 45: Emittance as a function of temperature for samples of different surface roughnesses and densities.

Emittance as a function of wavelength also showed no significant difference between D1R1-D1R2 and D1R1-D3R1 as seen in Figure 46 at temperatures of 2100°C. However, at 1600°C both D1R3 and D2R1 showed slightly lower emittance values. It is unclear why this is the case, but it may be due to the formation of the oxide structure. A study done by Eldridge et. al. [26] showed for thick yttrium stabilized zirconia in the 1.5-4µm (1500-4000nm) range at 1350°C the transmittance was essentially negligible, and the sample showed a reflectance of ~0.7. Assuming emittance is equal to the difference between 1 and reflectance, the emittance value would be ~0.3. Liebert [25] also found that the emittance of ZrO_2 between 1µm-4µm range emittance to be between 0.3-0.4. The emittance as a function of wavelength at hold times of 10s, 20s, 30s, 40s, 50s, and 60s was compared and showed time had little effect on resulting emittance graph as seen in Figure 46 for D1R2. Again, all samples had the same results.

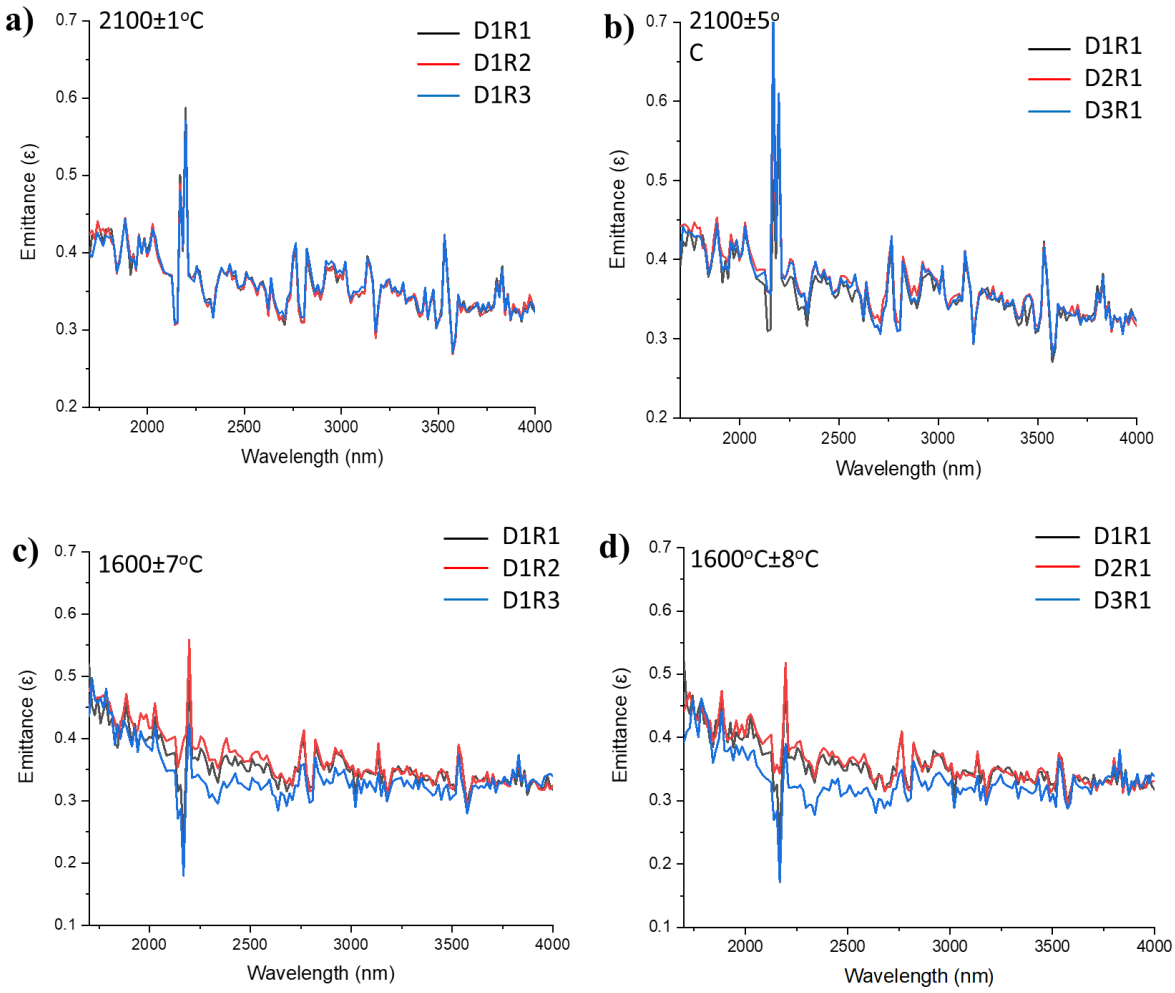

Figure 46: Emittance as a function of wavelength for a) different surface roughnesses at 2100°C, b) different densities at 2100°C, c) difference surface roughnesses at 1600°C, and d) different densities at 1600°C.

4.0 Conclusion

Billets with different densities and surface roughnesses were sintered and tested for spectral emittance at the RHINO lab at the Air Force Research Laboratory. Results showed surface roughness and density had little effect on the resulting microstructure. This is likely due to how the system oxidizes. The lack of c_1-$Sm_{0.2}Zr_{0.8}O_{1.9}$ on the side where radiance was collected is likely due to testing position as well as the lower PO_2 content compared to ablation in an oxyacetylene torch rig. In the temperature range investigate the surface roughness and density also had no effect on the spectral emittance. This was likely due to the similar microstructure as well as the main oxide formed for all of the samples tested was m-ZrO_2. However, it is believed if surface roughness and porosity were measured on an oxidized sample of c_1-$Sm_{0.2}Zr_{0.8}O_{1.9}$, the results may be different.

References

[1] T. H. Squire and J. Marschall, "Material property requirements for analysis and design of UHTC components in hypersonic applications," *J. Eur. Ceram. Soc.*, 30[11], 2239–2251, (2010).

[2] F. Monteverde, "The thermal stability in air of hot-pressed diboride matrix composites for uses at ultra-high temperatures," *Corros. Sci.*, 47[8], 2020–2033 (2005).

[3] W. Tan, C. A. Petorak, and R. W. Trice, "Rare-earth modified zirconium diboride high emissivity coatings for hypersonic applications," *J. Eur. Ceram. Soc.*, 34[1], 1–11 (2014).

[4] M. Tului, G. Marino, and T. Valente, "Plasma spray deposition of ultra high temperature ceramics," *Surf. Coat. Technol.*, 201[5], 2103–2108 (2006).

[5] W. Tan, M. Adducci, and R. Trice, "Evaluation of rare-earth modified ZrB_2- SiC ablation resistance using an oxyacetylene torch," *J. Am. Ceram. Soc.*, 97[8] 2639–2645 (2014).

[6] W. Tan, M. Adducci, C. Petorak, A. E. Brenner, and R. W. Trice, "Effect of rare-earth dopant (Sm) concentration on total hemispherical emissivity and ablation resistance of ZrB_2/SiC coatings," *J. Eur. Ceram. Soc.*, 1–9 (2016).

[7] O. Rozenbaum, D. D. S. Meneses, P. Echegut, O. Rozenbaum, D. D. S. Meneses, P. E. Texture, Texture and Porosity Effects on the Thermal Radiative Behaviour of Alumina Ceramics, *Int. J. Thermophys.*, 30, 580-590(2009).

[8] F. Wang. L. Cheng, Q. Zhang, L. Zhang, Applied Surface Science Effect of surface morphology and densification on the infrared emissivity of C/SiC composites, *Appl. Surf. Sci.*, 313, 670-676 (2014).

[9] G. Wilson, "Hemispherical spectral emittance of ablation chars, carbon, and zirconia to 3700°K," Langley Research Center, Langley Station, Hamption, VA, NASA TN D-2704, (1965).

[10] L. Scatteia, D. Alfano, F. Monteverde, J. Sans, M. Balat-Pichelin, Effect of the machining method on the catalycity and emissivity of ZrB2 and ZrB2-HfB2 based ceramics, *J. Am. Ceram. Soc.*, 911461-1468 (2008).

[11] E. Sani, L. Mercatelli, J. Sans, L. Silvestroni, D. Sciti, Porous and dense hafnium and zirconium ultra-high termperature ceramics for solar recievers, *Opt. Mater. (Amst).* 36 (2013) 163-168.

[12] ASTM C373-06. *Standard Test Method for Total Hemispherical Emittance of Surfaces up to 1400°C.* ASTM International; 2006.

[13] T. Negano, and K. Kaneko, "Effect of atmosphere on weight loss in sintered silicon carbide during heat treatment," *J. Am. Ceram. Soc.*, 83 [11], 2781-2787 (2000).

[14] S. Zhang, G. Hilmas, and W. Farhenholtz, "Pressureless Sintering of ZrB_2-SiC Ceramics," *J. Am.Ceram. Soc.*, 91[1], 26-32 (2008).

[15] W. Tan, M. Adducci, R. W. Trice, "Evaluation of rare-earth modified ZrB_2/SiC ablation resistance using an oxyacetylene torch," *J. Am. Ceram. Soc.*, 97 [8] 2639-2645 (2014).

[16] A. E. Brenner, A. A. Peña, X. L. Phuah, C. Petorak, B. Thompson, and R. W. Trice, "Cyclic Ablation of High-Emissivity Sm-doped ZrB2-SiC Coatings on Alumina Substrates," *J. Euro. Ceram. Soc.*, 38, 1136-1142 (2018).

[17] J. Han, P, Hu, X. Zhang, and S. Meng, " Oxidation behavior of zirconium diboride-silicon

carbide at 1800°C," *Scripta Materialia*, 57, 825-828 (2007).
[18] D. Gao, Y. Ahang, J. Fu, C. Xu, Y. Song, and X. Shi, "Oxidation of zirconium diboride-silicon carbide ceramics under an oxygen partial pressure of 200 Pa: Formation of zircon," *Corrosion Science*, 52, 3297-3303 (2010).
[19] D. D. Jayaseelanm E. Zapata-Solvas, C. M. Carney, A. Katz, P. Brown, and W. E. Lee, "Microstructural evolution of HfB2 based ceramics during oxidation at 1600-2000oC," *J. Advances in Applied Ceramics*, 114, 277-295 (2015).
[20] S. N. Karlsdottir, and J. W. Halloran, "Formation of Oxide Films on ZrB2-15vol% SiC Composites During Oxidation: Evolution with Time and Temperature," *J. Am. Ceram. Soc*., 92 [6], 1328-1332 (2009).
[21] S.N. Karlsdottir, J.W. Halloran, and A.N. Grundy, "Zirconia Transport by Liquid Convection During Oxidation of Zirconium Diboride-Silicon Carbide Composite," *J. Am. Ceram. Soc*., 91 [1], 272-277 (2008).
[22] F. Monteverde, D. Alfano, and R. Savino, "Effects of LaB6 addition on arc-jet convectively heated SiC-containing ZrB2-based ultra-high temperature ceramics in high enthalpy supersonic airflows," *Corros. Sci*., 75, 443-453 (2013).
[23] S. N. Karlsdottir, J. W. Halloran, and C. E. Henderson, "Convection Patterns in Liquid Oxide Films on ZrB2-SiC Composites Oxidized at High Temperature," *J. Am. Ceram. Soc*., 90 [9], 2863-2867 (2007).
[24] R. Telle, F. Greffrath, and R. Prieler, "Direct Observation of the Liquid Miscibility Gap in the Zirconia-Silica System," *J. Eur. Ceram. Soc*., 35, 3995-4004 (2015).
[25] C. H. Liebert, "Emittance and Adsorptance of NASA Ceramic Thermal Barrier Coating System," Lewis Research Center, Cleaveland, OH, NASA TP 1190c.1 (1978).
[26] J. I. Eldridge, and C. M. Spruckler, "Determination of scattering and absorption coefficients for plasma-sprayed yttria-stabilized zirconia thermal barrier coatings at elevated temperatures," *J. Am. Ceram. Soc*., 92[10], 2276-2285 (2009).
[27] V. Y. Chekhovskoi, V. D. Tarasov, and N. V. Grigor'eva, "The spectral emissivity of an oxide film of zirconium for wavelengths of 530 and 650 nm in the temperature range of 1450-1750 K," *High Temperature*, 42[2], 252-258 (2004).